

**THE EFFECT OF RAPID SOLIDIFICATION AND HEAT  
TREATMENT ON MICROSTRUCTURE AND  
ELECTROCHEMICAL PROPERTIES OF ADVANCED  
BIOMATERIAL CO-CR-MO-C ALLOY**

by

Hamid Reza Erfanian Nazif Toosi

A Dissertation Submitted in  
Partial Fulfillment of the  
Requirements for the Degree of

Doctor of Philosophy  
in Engineering  
at  
The University of Wisconsin-Milwaukee

December 2019

## ABSTRACT

### THE EFFECT OF RAPID SOLIDIFICATION AND HEAT TREATMENT ON MICROSTRUCTURE, ELECTROCHEMICAL, AND MECHANICAL PROPERTIES OF ADVANCED BIOMATERIAL CO-CR-MO-C ALLOY

by

Hamid Reza Erfanian Nazif Toosi

The University of Wisconsin-Milwaukee, 2019

Under the Supervision of Professor Hugo F. Lopez

Co-Cr-Mo-C alloys have been used for implant materials for decades because of their strength, corrosion resistance, wear resistance, and biocompatibility. To develop durable low-friction joint replacement implants, it is important to understand the solidification structure and properties of these materials. While  $\epsilon$ -HCP phase is the thermodynamically stable phase in these alloys, they maintain their high-temperature  $\gamma$ -FCC matrix and coarse dendritic structure on cooling to room temperature when cast by conventional methods. In this research, a wedge-shaped copper chill mold was used to examine the effect of cooling rates from 10 K/s to 450 K/s on the microstructure,  $\epsilon$ -HCP fraction, and corrosion properties of ASTM F75 alloy. The effect of laser surface modification, with an effective cooling rate of  $\sim 8900$  K/s, was also investigated. In addition, the effect of isothermal aging (750 – 900°C, 3 – 25 hours) on the  $\gamma$ -FCC to  $\epsilon$ -HCP transformation was studied. Cast specimens showed a columnar dendritic structure, with the dendrite arm spacing and carbide size decreasing and fraction of  $\epsilon$ -HCP increasing as cooling rate increased. On the other hand, laser surface modification resulted in a fully cellular structure with 100%  $\gamma$ -FCC. Rapid solidification was found to result in an improvement in corrosion resistance, which was attributed to a more uniform structure and distribution of alloying elements. In addition, a time temperature transformation (TTT) diagram was developed for

isothermal aging of this alloy; the  $\gamma$ -FCC to  $\epsilon$ -HCP transformation was found to be most rapid at 800°C.

© Copyright by Hamid Reza Erfanian-Nazif-Toosi, 2019  
All Rights Reserved

## TABLE OF CONTENTS

1. Introduction .....	1
1.1. Research Objectives and Scope.....	2
1.2. Hip and Knee implant design.....	4
1.3. Metallic Biomaterials .....	5
1.3.1. Stainless Steels.....	6
1.3.2. Titanium Alloys .....	7
1.3.3. Co-Cr Alloys.....	8
1.4. History of Knee and Hip Implant.....	9
1.4.1. Co-Cr-Mo-C as Hip and Knee Implant Material .....	10
1.5. Co-Cr-Mo Alloy Physical Properties .....	12
1.5.1. Isothermal Transformation (Heat Treatment).....	25
1.5.2. Athermal Transformation.....	38
1.5.3. Strain Induced Transformation (SIT).....	46
1.6. Importance of the HCP Crystal Structure for Development of Low-Friction Joint Replacement Implants .....	49
1.7. Corrosion of Co alloy.....	50
2. Materials and Methods .....	56
2.1. Samples Preparation and Characterization.....	57
2.2. Laser modification.....	58
2.3. Heat treatment .....	59
2.4. Corrosion test .....	60
3. Results and discussion.....	61
3.1. Microstructure characterization.....	62
3.1.1. Mathematical model of directional solidification under conditions of forced solidification (rapid solidification) .....	76
3.1.2. X-ray Diffraction (XRD) .....	84
3.2. Laser modified surface.....	89
3.2.1. Microstructure analysis.....	89
3.2.2. X-ray diffraction .....	97

3.3.	Heat Treatment of Co-Cr-Mo-C rapidly solidified alloy .....	98
3.3.1.	Effect of heat treatment on mechanical properties and X-ray diffraction patterns	102
3.4.	Corrosion test .....	104
4.	Conclusions .....	112
5.	References .....	115
6.	Appendix .....	122
7.	Curriculum Vitae .....	126

## LIST OF FIGURES

Figure 1.1 - Graphic representation of hip implant and its different component. ....	4
Figure 1.2 - Graphic representation of knee implant and its different component. ....	5
Figure 1.3- Phase diagram of Co-Cr alloy. ....	15
Figure 1.4 - Co-Cr-Mo-C alloy microstructure taken by Scanning Electron Microscopy (SEM) along with its correspond Energy Dispersive X-Ray Spectroscopy (EDS). ....	16
Figure 1.5 – Thermo-calc simulated phase diagram of Co-28Cr-6Mo-0.05C alloy (C = carbide). .....	17
Figure 1.6 - Edge dislocation in a cubic network centered on the faces. ....	19
Figure 1.7 - Partial dislocation in a cubic crystalline network centered on the faces. ....	20
Figure 1.8 - Orientation relationship between the Burgers vectors of a total dislocation and its partial dislocations. ....	20
Figure 1.9 - Extended dislocation shows the decrease in stress energy in the crystal lattice by the separation of a perfect dislocation into two partial dislocations. ....	22
Figure 1.10 - Location of sites A, B and C in a compact package. ....	23
Figure 1.11 - a) Compact hexagonal crystal structure and its stacking sequence; b) Cubic crystalline structure centered on the faces and their stacking sequence. ....	24
Figure 1.12 - a) Four repetitions along the direction of the FCC crystal structure with 15 (111)-layers and one atom per layer. b) Four repetitions along the direction of the tilted crystal structure with 15 (111)-layers. A SF is located between the ninth (counting from the bottom layer) and the fourteenth layer at the cell boundary represent HCP crystal structure. ....	25
Figure 1.13 - Effect of solution temperature and time on the mount of HCP phase formed during 5 hours of isothermal ageing at 800 °C of water quenched Co-27Cr-5Mo-0.05C [40]. ....	27

Figure 1.14 - Example of HCP $\epsilon$ -martensite formation on Co-Cr-Mo-C alloy, aged at 900 °C for 10 hours.....	30
Figure 1.15 - Transformation-Temperature-Time (TTT) diagram for the isothermal FCC to HCP transformation in Co-27Cr-5Mo-0.05C alloy [41]. .....	31
Figure 1.16 - TTT diagram for material annealed Co-Cr-Mo-C alloy at 1150°C, water quenched, and then isothermally aged at 700°C to 900°C [44].....	32
Figure 1.17 - TTT diagram for Co-based alloy in wrought and as cast conditions ageing directly from annealing temperature [41]. .....	34
Figure 1.18 - TEM micrograph of discontinuous strings of carbides in a Co-27Cr-5Mo-0.05C alloy after ageing at 1123 K for 1 hour [26]. .....	38
Figure 1.19 - (a) Martensite embryo with thin ellipsoidal geometry, $c$ and $a$ corresponds to semi-thickness and radius, respectively, (b) Top view for martensite embryo that resembles a flat plate, (c) In front view for martensite embryo that resembles a needle shaped morphology [52]. .....	41
Figure 1.20 - Energy surface generated by arbitrary variation of $c$ and $a$ plate dimensions in Eq. (2). Minimal energy conditions for the Co-20Cr alloy, a Co-29Cr-6Mo alloy and a Fe-Cr-Ni steel are marked by a circle, a square and a triangle, respectively [50]. .....	44
Figure 1.21 - (a) SEM micrograph of the as-chill cast Co-20Cr alloy showing a part of columnar dendrites directionally solidified, (b) X-ray mapping of Cr (chromium) [50]. .....	46
Figure 2.1 - (a) Wedge-shaped copper mold isolated in both sides by an alumina sheet; (b) “V” shaped ingot showing three different cooling rate zones: 90 mm high: 120 K/s, 60 mm high: 230 K/s, and 20 mm high: 450 K/s. ....	58

Figure 3.1– Images of Co-Cr-Mo-C alloy regarding its distance from the tip of the “V” shape mold- Sand cast-90 mm (cooling rate: 10 K/s), a) optical image 200x and SEM images b) 100x, c) 500x, and d)2000x. ....	63
Figure 3.2 – Images of Co-Cr-Mo-C alloy regarding its distance from the tip of the “V” shape mold- Copper mold cast-90 mm (cooling rate: 120 K/s), a) optical image 200x and SEM images b) 100x, c) 500x, and d)2000x.....	64
Figure 3.3 – Images of Co-Cr-Mo-C alloy regarding its distance from the tip of the “V” shape mold- Copper mold cast-60 mm (cooling rate: 230 K/s), a) optical image 200x and SEM images b) 100x, c) 500x, and d)2000x.....	65
Figure 3.4 – Images of Co-Cr-Mo-C alloy regarding its distance from the tip of the “V” shape mold- Copper mold cast-20 mm (cooling rate: 450 K/s), a) optical image 200x and SEM images b) 100x, c) 500x, and d)2000x.....	66
Figure 3.5 - Microstructure analyzing of Co-Cr-Mo-C alloy regarding their cooling rates. ....	67
Figure 3.6 – Showing carbide morphology in Co-Cr-Mo-C alloy regarding its cooling rate, a) 10 K/s cast in sand mold 90 mm from the tip of “V” shaped mold, and b) 450 K/s cast in copper mold 20 mm from the tip of “V” shaped mold. ....	69
Figure 3.7 - Shows the EDS analysis results on the a) matrix and b) carbide of the sand cast alloy 90mm from the tip of the “V” shaped mold. ....	70
Figure 3.8 - Shows the EDS analysis results on the a) matrix and b) carbide of the copper mold cast alloy 90mm from the tip of the “V” shaped mold. ....	71
Figure 3.9 - Shows the EDS analysis results on the a) matrix and b) carbide of the copper mold cast alloy 60mm from the tip of the “V” shaped mold. ....	72

Figure 3.10 - Shows the EDS analysis results on the a) matrix and b) carbide of the copper mold cast alloy 20mm from the tip of the “V” shaped mold. ....	73
Figure 3.11 - Shows the EDS results of Co-Cr-Mo-C alloy in presence of carbide. ....	74
Figure 3.12 - Shows the EDS results of Co-Cr-Mo-C alloy in presence of carbide. ....	75
Figure 3.13 - Results of the mathematical model of directional solidification. ....	84
Figure 3.14 – XRD results of Co-Cr-Mo-C alloys regarding their cooling rate. ....	86
Figure 3.15 - Schematic illustration of coherent growth between the $\gamma$ -Co, FCC and $\epsilon$ -Co, HCP phases in the austenite-martensite transformation. Note the relationship between the lattice parameter HCP and the major diagonal of the unit cell FCC. ....	87
Figure 3.16 – Showing the HCP phase formed in rapidly solidified Co-Cr-Mo-C alloy, 2cm from the tip of the Cu mold cast in two different magnifications. ....	88
Figure 3.17 – Optical images of the as-cast Co-Cr-Mo-C alloy showing (a) the dendritic matrix structure and (b) carbide precipitates in the interdendritic regions and at dendritic grain boundaries. ....	90
Figure 3.18 – SEM and EDS results of as-cast Co-Cr-Mo-C alloy showing (a) athermal $\epsilon$ -martensite, (b) dendritic structure of as-cast alloy including carbides, (c) EDS peaks of alloying elements in the matrix and (d) EDS elements in precipitated carbides. ....	91
Figure 3.19 - Optical images of the Co-Cr-Mo-C alloy after pulsed laser (a) Side view of the solidified metal pool and surrounding as-cast alloy b) front view of solidified metal string beads. ....	94
Figure 3.20 – SEM images of solidified LSM Co-Cr-Mo-C alloy. (a) Solidified cellular structure, (b) cellular solidified front showing the carbide distribution in the cell boundaries, (c)	

EDS peaks of alloying elements in cellular matrix and (d) EDS peaks of elements in intercellular carbides. ....	95
Figure 3.21- XRD results of Co-Cr-Mo-C alloy a) As-cast b) Laser surface modified (LSM). ..	98
Figure 3.22 – Phase diagram of Co-C, shows zero solubility of carbon in HCP cobalt alloy [40]. .....	100
Figure 3.23 – Co-Cr-Mo-C alloy after ageing heat treatment solutionized at 1150 °C for 1 hour and then aged at 850 °C for a) 5 hours, b) 10 hours, c) 20 hours d) 20 hours in 2000x magnification .....	101
Figure 3.24 - XRD results of Co-Cr-Mo-C alloy aged at 800 °C for 7 h, 10 h, and 15 h.....	103
Figure 3.25 - Transformation-Time-Temperature diagram for the Co-Cr-Mo-C alloy.....	104
Figure 3.26 – Potentiodynamic curves for Co-Cr-Mo-C alloy in different conditions (Cu: Cu mold cast, Sand: Sand mold cast). ....	106
Figure 3.27 – Optical microstructure of Co-Cr-Mo-C in different casting conditions, a) Sand cast- 9cm from tip and b) Cu mold cast- 2cm from tip.....	107
Figure 3.28 – EDS line scan and mapping of CoCrMoC alloy, a) as-cast, b) laser surface modified. ....	111
Figure 6.1A - Phase diagram of Co-Cr-6Mo based on Thermo-Calc simulation software. ....	123
Figure 6.2A - Phase diagram of Co-Cr-6Mo-0.25C based on Thermo-Calc simulation software (C = Carbides).....	124

## LIST OF TABLES

Table 1.1 – Mechanical properties of Co-Cr alloys .....	11
Table 1.2 - The lattice parameters of HCP cobalt and FCC cobalt.....	13
Table 1.3 – Properties of Co-20Cr [50] .....	43
Table 1.4 – Computed $\Delta G_V$ , energy barrier values and critical parameters for athermal martensite nucleation in selected alloys [50].....	43
Table 1.5 - General chemical composition of the human biological fluids .....	51
Table 1.6 - Chemical composition (g/L) of different solutions used for corrosion test .....	54
Table 1.7 - Corrosion characteristics of Co-Cr-Mo alloys after different types of processing....	55
Table 2.1 - Chemical composition (wt%) of as-cast Co-Cr-Mo-C sample.....	60
Table 3.1 - Microstructure analyzing of Co-Cr-Mo-C alloy in different positions.....	67
Table 3.2 - Properties for Co-28Cr-6Mo-0.....	77
Table 3.3 - Laser melting parameters and cobalt thermal properties.....	93
Table 3.4 Corrosion parameters for Co–Cr–Mo–C alloys in Ringer’s solution.....	108

## **ACKNOWLEDGMENTS**

I wish to thank my advisor Professor Dr. Hugo F. Lopez for his patience and support over the course of this project. I would also like to thank Dr. A. L. Ramirez-Ledesma for all her assist in sample preparation. I would like to thank Materials Science and Engineering department at UWM for the support during my Ph. D. education.

I would like to thank my parents: my dad, Mohammad Reza Erfanian Nazif Toosi and my mom, Nasrin Boroumand for their extraordinary support and sacrifice.

## *1. Introduction*

## 1.1. Research Objectives and Scope

Despite the tremendous volume of research that has been done on the properties and modifications of Co-Cr and Co-Cr-Mo-C alloy over the past several decades, there is no published article on the effect of solidification rate and rapid solidification on the mechanical, physical, and electrochemical properties of Co-Cr-Mo-C alloy.

In this investigation, samples were prepared by rapid solidification. In addition, laser welding was applied on Co-Cr-Mo-C as-cast alloy to modify its surface. Microstructure characteristics of as-cast, rapidly solidified and surface modified implant alloy were studied. Potentiodynamic method is used to investigate the corrosion behavior of samples in biological Ringer's solution. Experimental results from both microstructure and electrochemical analysis were compared and discussed.

The objectives of this work are as follows:

- a) Prepare rapidly solidified Co-Cr-Mo-C alloy with rates of up to 450 K/s, using sand and copper mold casting.
- b) Evaluate the effect of cooling rate (rapid solidification and laser modified sample) on the microstructure (morphology, dendrite arm spacing, secondary dendrite arm spacing, and alloying elements distribution) of Co-Cr-Mo-C alloy.
- c) Investigate the effect of cooling rate (rapid solidification and laser modified sample) on corrosion behavior (corrosion rate and potential) of Co-Cr-Mo-C alloy.

- d) Determine the amount of formed  $\epsilon$ -HCP phase in Co-Cr-Mo-C alloy in as-cast condition, prepared by rapid solidification, and modified by laser surface treatment.
- e) Determine the amount of formed  $\epsilon$ -HCP phase in Co-Cr-Mo-C alloy after applying isothermal heat treatment on samples which are prepared by rapid solidification method and establishing a corresponding TTT diagram.
- f) Evaluate the carbide modification (carbides morphology, composition, size, and elements distribution) formed at different cooling rates.

## 1.2. Hip and Knee implant design

Physiologically, the hip joint is called a ball and socket structure because the spherical head of the thighbone (femur) moves inside the cup-shaped hollow socket (acetabulum) of the pelvis, Figure 1.1. Therefore, to replicate this structure, a total hip replacement has three parts: a) the stem that fits into the femur, b) the ball that replaces the spherical head of the femur, and c) the cup that fits into the worn cut acetabulum [1].

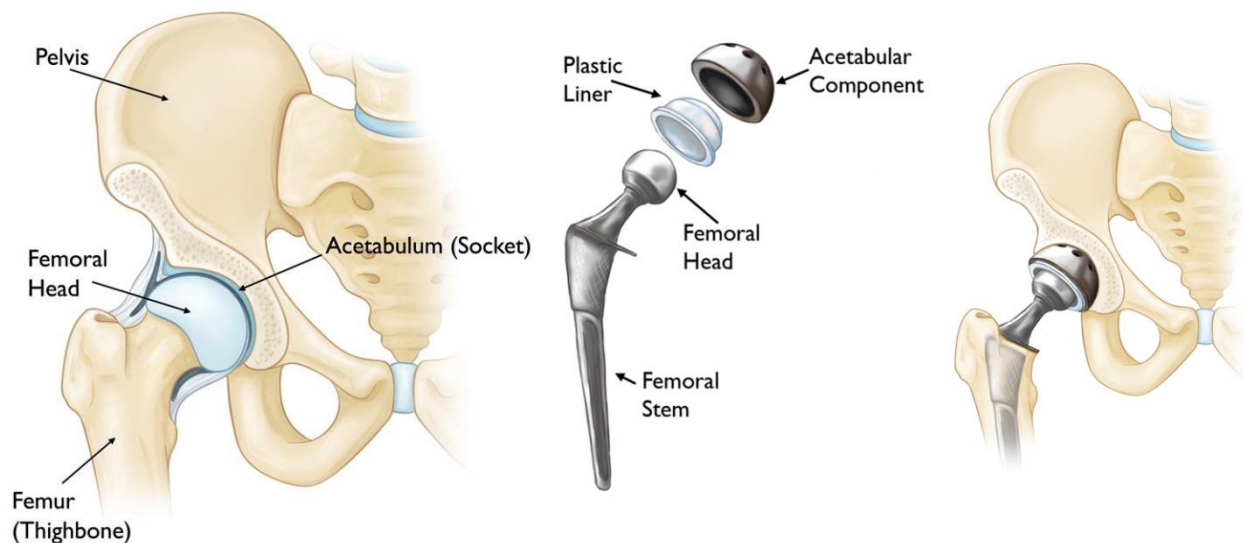


*Figure 1.1 - Graphic representation of hip implant and its different component.*

The knee can be simply considered as a hinge joint. In reality, it includes rolling and gliding as well. All knee implants are composed of three main parts: a) a curved femoral component to replace the lower end of the thighbone, b) a flat tibial component to replace the top surface of the shinbone, and c) a dome shaped patella to replace the kneecap, these parts are shown in Figure 1.2 [1].

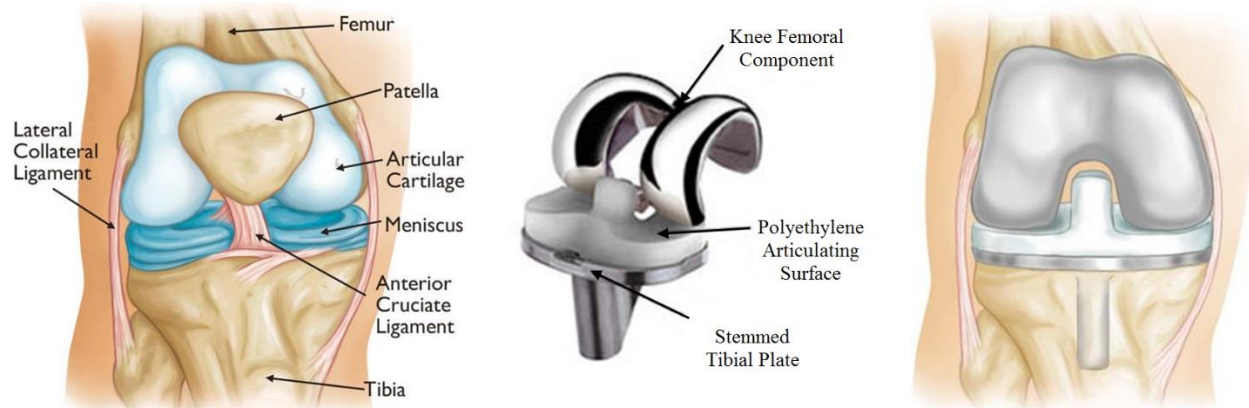


*Figure 1.2 - Graphic representation of knee implant and its different component.*

### **1.3. Metallic Biomaterials**

Metal materials have been used in medical industry equipment and surgical tools for decades. That is mainly because metallic materials have benefits compared to polymer and ceramic materials, such as: an ideal combination of strength-toughness, ductility and fatigue properties, associated with them. Also, manufacturing metallic materials is easier than ceramics and polymers regarding advanced mass production methods such as casting and forging [2]. The metallic biomaterial series is including Co-Cr based alloys, titanium-based alloys and austenitic stainless steels. For implants biomaterials, several requirements can be considered:

1. Biocompatibility [3];
2. Mechanical properties: strength [4], ductility, Young' modulus [5], and fatigue strength [6];
3. Surface properties: wear [7] and corrosion [8] resistance.

Considering the above requirements, Ti and Ti-based alloys demonstrate excellent biocompatibility and corrosion resistance; however, their poor wear resistance has limited their application for such a high-load surface engagement of hip and knees joint prostheses [5]. In addition, austenitic stainless steels will satisfy most of the conditions. In contrast with Ti alloys, austenitic stainless steels implants are susceptible to pitting and crevice corrosion especially for long-term application [9]. On the other hand, Co-Cr alloys are highly resistant to corrosion and fatigue and have better wear resistance than austenitic stainless steels and Ti alloys [10]. Therefore, Co-Cr alloys have been used as one of the best metallic biomaterials for metal-on-metal hip joint prostheses.

### **1.3.1. Stainless Steels**

Stainless steel 18-8, which contains ~ 18% by weight of chromium and ~ 8% by weight of nickel was introduced for application in the human body. Ni and Cr provide this alloy a considerable resistance to corrosion. The addition of Mo greatly improved the corrosion resistance of these materials, which are known as stainless steels 316. Subsequently, the decrease in C from 0.08 to 0.03% by weight increased the resistance to corrosion in chlorinated environments, these materials are known as 316L stainless steels. Austenitic stainless steels have a face-centered cubic crystal structure (FCC), by ASTM specification and are currently the most widely used in the field of medicine (ASTM F138, ASTM F139). The various adverse reactions that nickel causes when released into the human body are one of the major disadvantages of 316L austenitic stainless steels [11]. This problem has been faced with the development of austenitic stainless

steels free of nickel with a high percentage of nitrogen, which stabilizes the austenitic phase FCC [12]. The manufacture of cardiovascular stents represents a major challenge in these materials because they suffer from a significant dimensional change in the cross section, as a result of expansion during performance.

### **1.3.2. Titanium Alloys**

The most studied and relevant titanium-based alloy is Ti-6Al-4V (ASTM F136). One of the most relevant characteristics of pure Ti (ASTM F67) is its low density, with a value of  $4.5 \text{ g/cm}^3$  in comparison with stainless steels and Co-Cr base alloys, with values of  $7.9 \text{ g/cm}^3$  and  $8.3 \text{ g/cm}^3$ , respectively. This is characterized by having a high tensile strength and excellent resistance to corrosion [5]. Regarding to pure titanium (98.9 - 99.6%), the main disadvantage lies in the percentage of oxygen depending on the degree of purity of the material. For example, for grade 1 titanium with 0.18% oxygen the yield stress is around 170 MPa while with 0.40% oxygen (grade 4), the yield stress presents an increase of approximately 485 MPa. There are several investigations that report vanadium as an element that generates strong cytotoxicity [13]. When this element is in contact with the fluids of the human body for a long time it produces severe adverse reactions. For example, stimulation of the mucosa in the organs of the respiratory system and a significantly detrimental effect on blood production [13]. Aluminum is also an element that causes unrest due to the unfavorable reactions it generates in contact with biological fluids. Recently, other types of titanium-based alloys have been developed to replace both vanadium and aluminum in their chemical composition. For this reason, it has been proposed the

implementation of titanium-based alloys with non-toxic elements such as: Nb, Ta and Zr. Since niobium and vanadium belong to group V in the periodic table, they show much similarity. In particular, both elements have the ability to stabilize the  $\beta$  phase in the Ti-V and Ti-Nb systems. The above is necessary to obtain the microstructure formed by the combination of  $\alpha + \beta$  phases in these materials [13].

### **1.3.3. Co-Cr Alloys**

The next following sections are focused on describing in detail the importance to study and understand the properties of Co-Cr alloys particularly as hip and knee implant materials.

The mechanical properties of any alloy can vary drastically depending on its chemical composition and processing. For this reason, Co-Cr alloys are classified depending mainly on these two factors. The main benefit of using this alloy is its resistance to corrosion in chlorinated environments which is the result of its bulk composition and the passive layer of oxide formed on the surface ( $\text{Cr}_2\text{O}_3$ ). This alloy has a long history in the aerospace industry and biomedical implants [14]. With respect to the conventional casting of Co-Cr-Mo alloys, it is known that they are susceptible to mechanical failure. For this reason, currently the main method of manufacture of these alloys is investment casting process. The maximum carbon content for the F75 alloys (Co-28Cr-6Mo) is 0.35% by weight. A low carbon content for the F75 alloy is possibly the cause of formation the  $\sigma$  phase (brittle intermetallic compound  $\rightarrow$  Co (CrMo)). It is known that the presence of  $\sigma$  phase considerably reduces the mechanical properties in this of material [15].

#### **1.4. History of Knee and Hip Implant**

Around 1930, a Co-Cr-Mo alloy ("Vitallium") was obtained by the investment casting method, which was marketed for use as a dental prosthesis [16]. Due to its excellent mechanical properties, high resistance to corrosion and wear, the application of this alloy was increased in areas of orthopedics and cardiovascular devices compared with others [16]. Total hip replacement (THR) operation has been started since the early 1960s by Sir John Charnley when he developed the first THR with low friction arthroplasty. Charnley developed a hip replacement consisting of a metal femoral stem and a polyethylene component for seating the joint in the acetabulum of the pelvis. Elwood Haynes was the person who patented the development of cobalt-chromium (Co-Cr) alloys known as Stellite. He also found that adding alloying elements such as: tungsten (W) and molybdenum (Mo) could enhance the mechanical properties of Co-Cr alloys [17].

Surgeons' choice of materials varied considerably among different materials such as: stainless steel, cobalt–chrome alloy, Teflon®, and high-density polyethylene, as did the prosthesis design. Total hip replacements usually have three parts as it was previously mentioned in section 1.1. Hip implants stem is usually made of titanium or cobalt-chromium alloys due to their good mechanical properties and corrosion resistance. The ball's material is commonly cobalt-chromium alloys because of its good wear resistance properties. Despite all efforts to utilize new materials for hip implant, cobalt-chromium is still dominant [18].

Knee implant can be considered as a hinge joint composed of three parts (Figure 1.2). The femoral part is usually made of cobalt-chromium alloys to provide low wear and smooth motion. The tibial component has a metal platform and an ultrahigh density polyethylene (UHDPE) as well as patella part.

Any type of materials developed for knee and hip implant shall meet three main requirements:

- Mechanical stability for the system; avoid stress shielding and bone resorption resulting from a mechanical mismatch with bone.
- High wear and corrosion resistance; reducing wear debris to avoid excessive metal ion release in the body fluids.
- Achieve quick and strong bonding with bones; prevent excessive tissue growth and inflammatory response.

#### **1.4.1. Co-Cr-Mo-C as Hip and Knee Implant Material**

Co-Cr-Mo-C alloys have been increasingly used in biomedical applications for their biocompatibility, excellent corrosion resistance, and mechanical and wear properties [19]. However, early cobalt-chromium alloys were not considered as optimal as titanium alloys regarding new bone-tissue integration [20]. Second generation of Co-Cr alloys performed successful after short to midterm follow up clinical studies [21].

There are four Co-Cr alloys available for using as hip and knee implant replacements which are listed in Table 1.1. Co-Cr F75 (as-cast/annealed conditions) are being widely used in the manufacturing of stems because of its high corrosion resistance in body fluid environments. Regular casting process characteristics such as: large grain size and casting defects result in low yield strength and fatigue fracture of a femoral stem. Therefore, to overcome these problems, investment casting and powder metallurgical methods are good alternatives. Higher solidification processes like investment casting are usually used for decreasing grain sizes as well as improving the alloying element distribution and carbides. F799 has a similar chemical composition to F75 except for being hot forged after casting. As a result, its mechanical properties such as: yield, fatigue, and ultimate tensile strength increase by the factor of two compared with as-cast F75. Adding Ni and processing F90 by cold work will make this alloy with mechanical properties twice as high as those for F75. F562 alloy, which is manufactured by cold working and an aging heat treatment, is one of the strongest materials for implant applications.

*Table 1.1 – Mechanical properties of Co-Cr alloys [22]*

<b>ASTM Designation</b>	<b>Condition</b>	<b>Young's Modulus (GPa)</b>	<b>Yield Strength (MPa)</b>	<b>Tensile Strength (MPa)</b>	<b>Fatigue Limit (At 10<sup>7</sup> Cycle, R = -1) (MPa)</b>
<b>F75</b>	As-cast/Annealed	210	448-517	655-889	207-310
	Powder Metallurgy Hot Pressed	253	841	1277	725-950
<b>F799</b>	Hot Forged	210	896-1200	1399-1586	600-896
<b>F90</b>	Annealed	210	448-648	951-1220	N/A
	44% Cold Worked	210	1606	1896	586
<b>F562</b>	Hot Forged	232	965-1000	1206	500
	Cold Worked, Aged	232	1500	1795	689-793 (At R = 0.05)

## 1.5. Co-Cr-Mo Alloy Physical Properties

Since the introduction of Co-based alloys as a prosthesis material, a considerable amount of research has been done on investigating the possibility of enhancing mechanical properties and biocompatibility of this alloy regarding its physical properties modification [23-27]. In as-cast cobalt alloys the solidified microstructures consist of a predominantly FCC dendritic structure which is accompanied by segregation, and second phase precipitates within the matrix and along the interdendritic regions. In addition, inherent investment casting defects are of concern as they can lead to early implant failure and inadequate mechanical properties [27]

In general, investment casting Co-Cr-Mo-C alloys used as biomedical devices exhibit poor ductility, shrinkage porosity, interdendritic segregation, and the presence of intermetallic compounds [28, 29]. Hence, in order to improve the alloy's performance for potential biomedical applications, modifications in alloy design and casting technology have been considered to enhance the strength and ductility of Co-based alloys [30]. In particular, changes in alloy design have been aimed at suppressing brittle-phase formation along the interdendritic regions during solidification [31].

There are two crystal structures allotrope of pure cobalt: a close-packed hexagonal (HCP) form ( $\epsilon$ -martensite) at temperatures below 417 °C and a face-centered-cubic (FCC) form ( $\gamma$ ) at temperatures above 417 °C and below the melting point (1495 °C). The density of pure cobalt is 8.85 and 8.80 g/cm<sup>3</sup> for HCP and FCC crystal structure, respectively. The hardness of cobalt

ranges from 135 HV to 260 HV depending on manufacturing methods and phase stability. The lattice parameters of two allotropes, FCC and HCP, at the ambient temperature are given in Table 1.2 [32]. The temperature of the phase transformation depends on the purity and on the solidification rate.

*Table 1.2 - The lattice parameters of HCP cobalt and FCC cobalt [32]*

HCP Cobalt Lattice parameters (nm)			FCC Cobalt Lattice Parameter (nm)
<i>a</i>	<i>c</i>	<i>a/c</i>	<i>a</i>
0.25071	0.40695	1.6233	0.35446

During regular cooling rates, after processing, the phase transformation has been suggested to occur by a martensite reaction, involving dislocation movements on the octahedral planes of the cubic lattice [32]. For implant materials application, it is sufficient to understand binary phase diagrams of Co-Cr close to 26-30 wt% of Cr content (Figure 1.3). Chromium improves the alloy corrosion resistance by forming the chromium oxide passive film on the surface locally and because of that it is one of the main alloying elements. In addition, increasing Cr concentration will raise the transition temperature of HCP to FCC. In Co-Cr-Mo-C alloy, molybdenum plays an important role when it is added to Co-Cr because of its crystal grain refinement capabilities in solid solution which leads to improvement in tensile strength and ductility [32] as well as corrosion resistance. Carbon content is a distinguishing element in Co-Cr-Mo-C systems. Low carbon versions of this alloy have a soluble carbon content of less than 0.15 wt% carbon; however, high carbon alloys are allowed to have up to 0.35 wt% carbon. ASTM F75 has a maximum carbon content of 0.35 wt%. Carbon in solid solution forms metal-carbides (MC). Where M stands for either chromium or molybdenum or the combination of both. Extra carbon

content results in a significantly higher volume fraction of carbides. Carbides in Co-Cr-Mo-C alloy have the formula of either  $M_{23}C_7$  or  $M_6C$  depending on the solidification rate and metal alloying element content (this will be fully discussed in section 3.1). Carbide precipitation has been one of the main strengthening mechanisms for the ASTM F75 [33] alloy and high carbon alloys have excellent wear resistant as attributed to their higher hardness, Figure 1.4 shows a Co-Cr-Mo-C alloy microstructure taken by Scanning Electron Microscopy (SEM) along with its correspond Energy Dispersive X-Ray Spectroscopy (EDS) map. In general, carbides increase strength, hardness, while reducing ductility in Co-Cr-Mo-C alloys. Furthermore, it has also been reported that increasing the nitrogen (0.04 to 0.14 wt%) content in solution for Co-Cr-Mo alloys increases the tensile and fatigue strength, slightly increases the hardness, while decreasing ductility [33].

According to the phase diagram of Co-Cr (Figure 1.3) in a Cr range of 26-30 wt%; at room temperature and high temperatures (higher than 800°C for Co-Cr binary)  $\epsilon$ -HCP and  $\gamma$ -FCC phases are expected to be thermodynamically stable, respectively. However, the  $\gamma \leftrightarrow \epsilon$  is strongly restricted by nucleation phenomena which result in having retained  $\gamma$ -FCC phase in most conventionally solidified Co-Cr-Mo-C alloys at room temperature [34, 35]. Apparently, the  $\gamma \leftrightarrow \epsilon$ , FCC to HCP, transformation is rather slow under normal cooling conditions. Hence, in most Co-based alloys, the FCC structure is retained at room temperature [28, 36]. In pure Co, the  $\gamma \leftrightarrow \epsilon$  FCC to HCP allotropic transformation takes place at a  $T_c = 417^\circ\text{C}$  (690 K) by a displacive martensitic transformation [37]. The transformation mechanism will be discussed in details later

this section. The transformation temperature,  $T_c$ , is shifted toward increasing temperatures (near 870°C [38]) in Co-28Cr-6Mo-0.05C wrought alloys as Cr and Mo expand the HCP field of stability, Figure 1.5. The resultant HCP phase from the martensitic transformation is known as  $\epsilon$ -martensite [37]. Appendix 1 shows all the calculated phase diagrams including: Co-28-6Mo and Co-28Cr-6Mo-0.25C alloys. In Co alloys, the martensitic transformation can be achieved by (1) isothermal, (2) athermal, and (3) a strain induced mechanism.

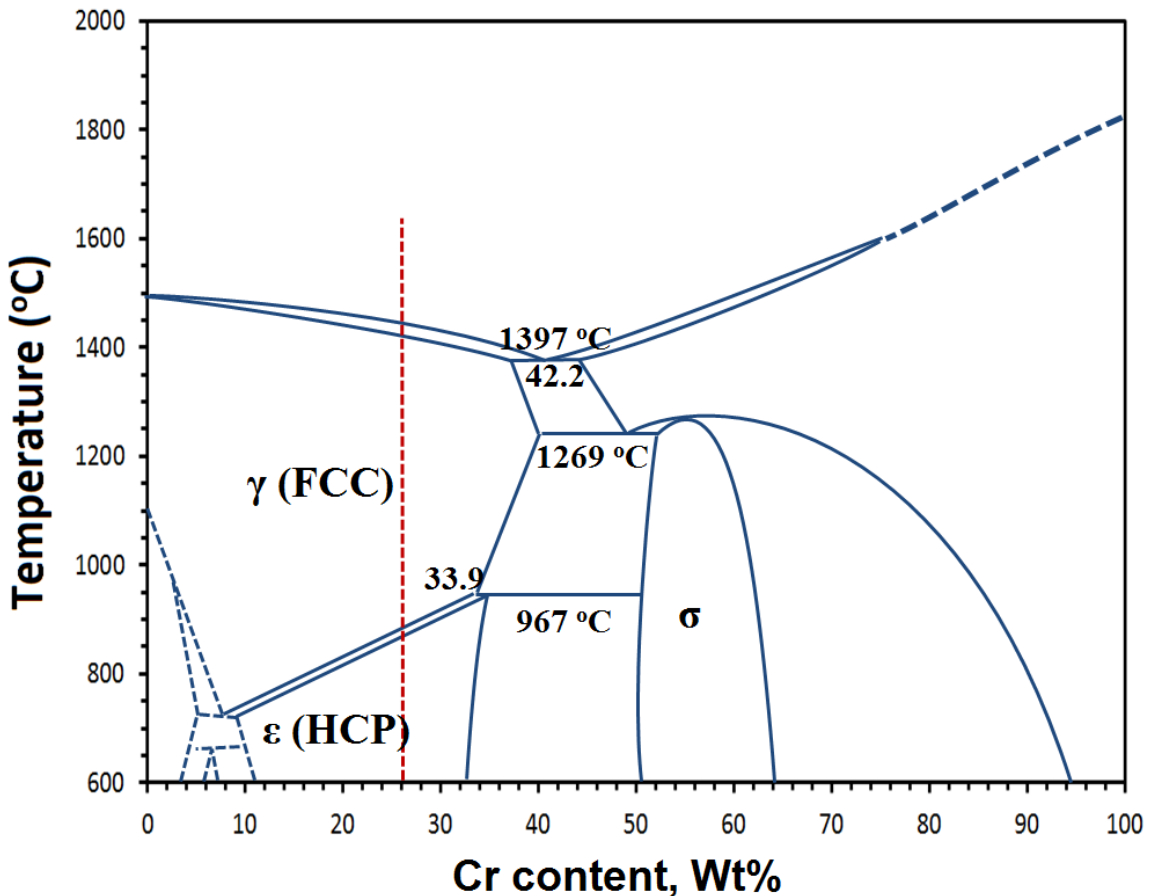
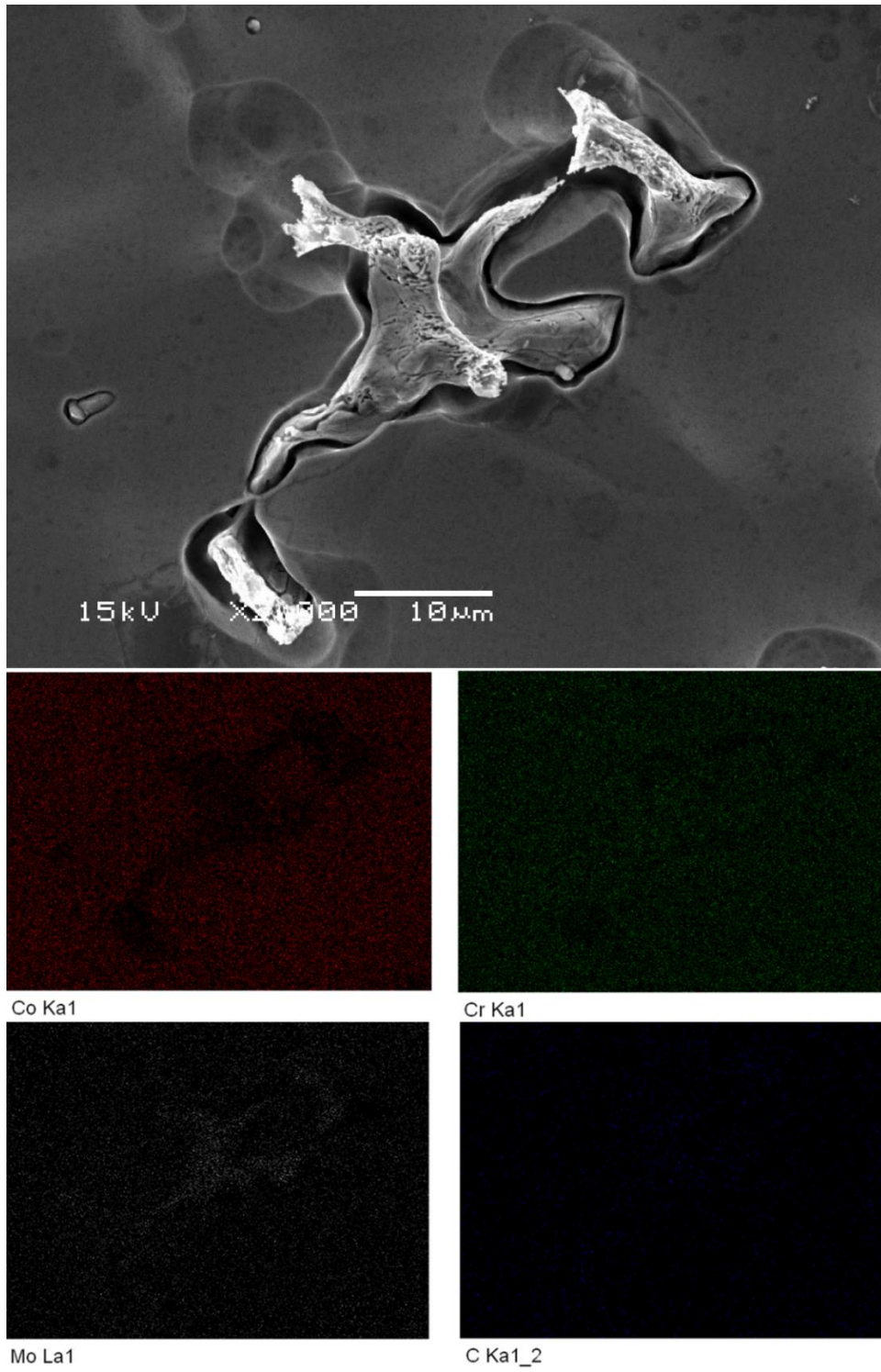
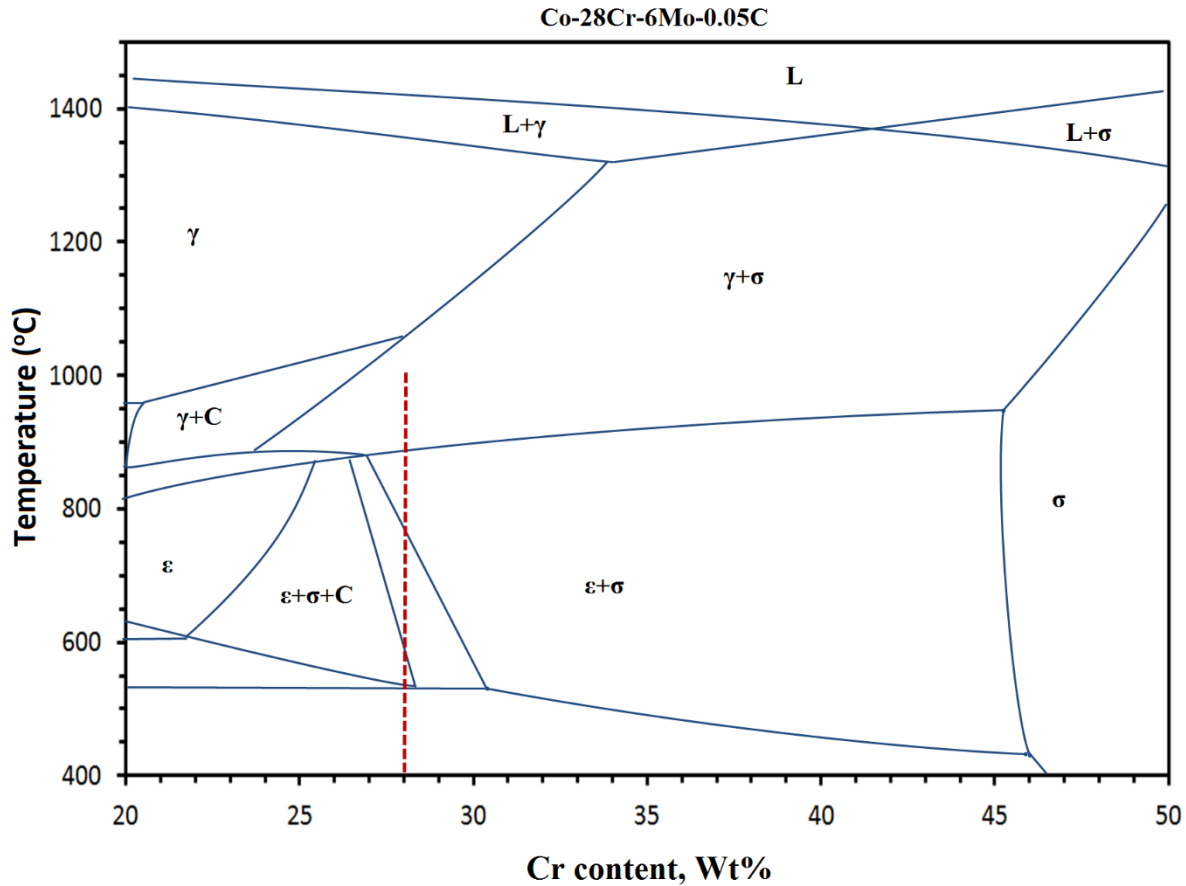


Figure 1.3- Phase diagram of Co-Cr alloy.



*Figure 1.4 - Co-Cr-Mo-C alloy microstructure taken by Scanning Electron Microscopy (SEM) along with its correspond Energy Dispersive X-Ray Spectroscopy (EDS).*



*Figure 1.5 – Thermo-calc simulated phase diagram of Co-28Cr-6Mo-0.05C alloy (C = carbide).*

The main characteristics of the martensitic transformation are:

- a) In the case of Co-Cr alloys, the  $\gamma$ -Co phase, FCC transforms diffusionless into  $\epsilon$ -Co, HCP. The necessary condition for the phase transformation to occur is that the free energy of the  $\epsilon$ -Co phase is less than that of  $\gamma$ -Co. If this is true, there are additional energy components, as a result of the surface energy and the stress energy of the deformation. Because of this, for the martensitic transformation to take place, the difference between the free energies of  $\gamma$ -Co and  $\epsilon$ -Co must exceed the additional

energy required. That is why a driving force or excess free energy is necessary for the transformation to take place.

- b) The martensite crystals form habit patterns defined with respect to the crystalline structure of the matrix phase. For the particular case of Co-Cr alloys the habit plane (undistorted) corresponds to  $\{111\}_{\gamma-Co, FCC} // \{0001\}_{\epsilon-Co, HCP}$
- c) The crystallographic axes of the  $\epsilon$ -Co crystals produced in a  $\gamma$ -Co crystal have a defined relationship to those untransformed  $\gamma$ -Co crystals.
- d) Surface relief occurs when martensite crystals are formed. Due to the volume change associated with the structure change.
- e) The crystals of  $\epsilon$ -Co, HCP, are formed with a defined habit pattern, with defined orientation relationships with respect to the  $\gamma$ -Co phase, FCC, and a defined surface relief. This leads to the conclusion that the transformation takes place as a result of a coordinated and ordered "re-arrangement" of the atomic configuration during the transformation.
- f) The change of shape is compensated by mechanisms of deformation by invariant network cutting, that is, mechanisms of plastic deformation such as sliding dislocations and twinning.

It is known that the main slip plane in a face centered cubic crystal structure is the octahedral  $\{111\}$ . In Figure 1.6 the following event is shown: the blue circles represent the compact plane (111) in which the extra plane of an edge dislocation ends. The green circles are the atoms in the compact (111) immediate plane. It can be clearly seen that in the last plane a whole row of

zigzag atoms is absent. This row corresponds to the omitted plane of the edge dislocation. It can be imagined that the natural movement of this dislocation is indicated by the black arrow in the graphical representation of Figure 1.6. This movement of atoms through the plane corresponds to a horizontal distance “b” that displaces the dislocation one unit to the left. Vector “b” represents the Burger’s vector for the mentioned dislocation, which is assigned as  $\frac{1}{2}[\bar{1}10]$ . This movement of dislocations represents a deformation in the crystal lattice because each green atom in the sliding plane will be forced to climb or climb over the blue atom underneath it and to the right.

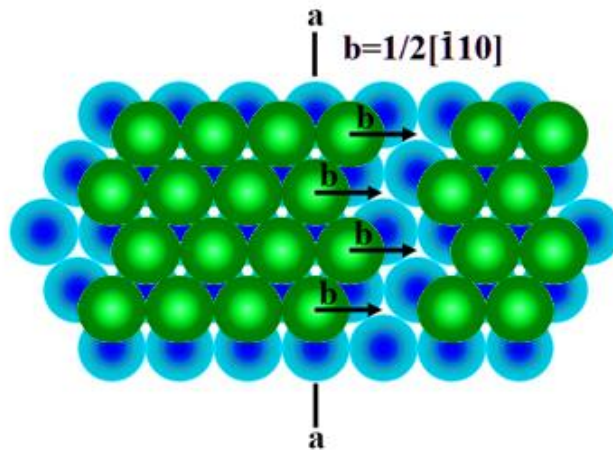


*Figure 1.6 - Edge dislocation in a cubic network centered on the faces.*

This does not happen in reality, since the actual movement of these dislocations is the one indicated by the vectors labeled “c” in Figure 1.7. This movement occurs with much less deformation in the crystal lattice. The second movement of the same type demonstrated by the vector “d”, leads the green atoms to the same final position as the simple movement indicated in Figure 1.6. It should be noted that the atomic arrangement shown in Figure 1.7 is particularly

important because it shows how a dislocation can be broken down into a pair of partial dislocations. The Burger's vectors of these partial dislocations are the vectors "c" and "d" in Figure 1.7. The notation of these vectors can be presumed with the help of Figure 1.8.

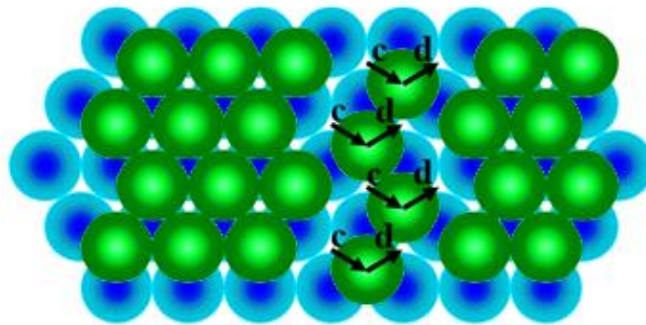


*Figure 1.7 - Partial dislocation in a cubic crystalline network centered on the faces.*

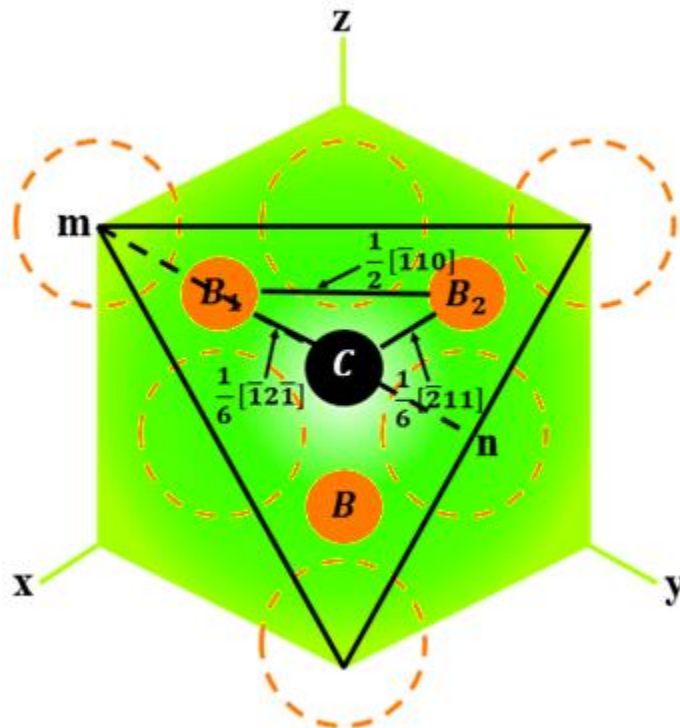


*Figure 1.8 - Orientation relationship between the Burgers vectors of a total dislocation and its partial dislocations.*

The surface of the plane (111) in cubic crystal structure with an atom located in center of the faces is shown in Figure 1.8. The Burger's vector for a dislocation is equal to the distance  $B_1B_2$ , while The Burger's vectors of the two partial dislocations "c" and "d" in Figure 1.7 correspond to the distances  $B_1C$  and  $CB_2$ , respectively. Thus, line  $B_1C$  leads to direction  $[\bar{1}2\bar{1}]$ . The index  $[\bar{1}2\bar{1}]$  represents a vector with a negative component in the  $x$  and  $z$  directions and a component with a magnitude of 2 in the  $y$  direction. This vector has the length of twice the distance  $mn$  in Figure 1.8. Knowing that  $B_1C$  is only one third of the  $mn$  line, the Burger's vector for this dislocation is  $\frac{1}{6}[\bar{1}2\bar{1}]$ . In this way, vector  $B_2C$  can be represented as  $\frac{1}{6}[\bar{2}11]$ . In summary, a perfect dislocation in a cubic crystalline structure centered on the faces  $\frac{1}{2}[\bar{1}10]$ , is capable of dissociating into two dislocations according to the following relationship:

$$\frac{1}{2}[\bar{1}10] = \frac{1}{6}[\bar{1}2\bar{1}] + \frac{1}{6}[\bar{2}11] \quad \text{Equation 1.1}$$

The decomposition of a perfect dislocation into two partial dislocations decreases the deformation energy of the crystal lattice, this is shown in Figure 1.9.

On the other hand, since the partial dislocations of Figure 1.7 constitute similar network force, a repulsive force exists between them which make dislocations to be always separated. Separation can add planes of atoms to the simple zigzag of Figure 1.6, this event is represented graphically in Figure 1.9. In this way, a dislocation that has been dissociated into a pair of separate partial



sequence are shown in Figure 1.11 (a). The compact plane can be indexed as (0001) and the compact directions are of type  $\langle 11\bar{2}0 \rangle$ .

Now, if the atoms of the third layer are placed in type C sites, the sequence  $ABCABC \dots$  is generated, which repeatedly produces a compact arrangement with face-centered cubic symmetry (FCC), as shown in Figure 1.11 (b).

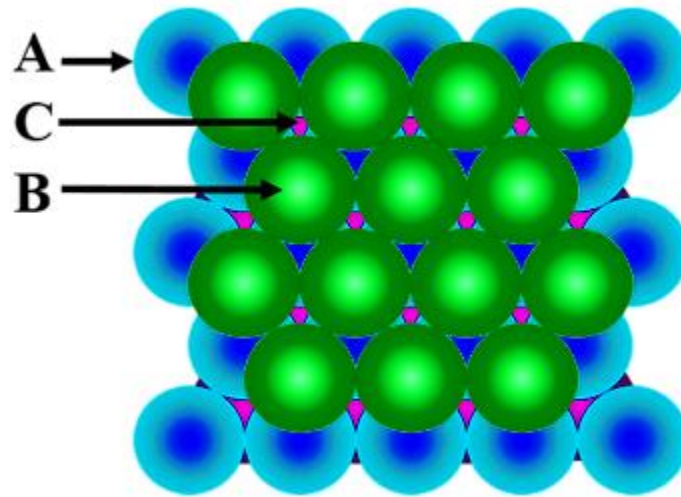


*Figure 1.10 - Location of sites A, B and C in a compact package.*

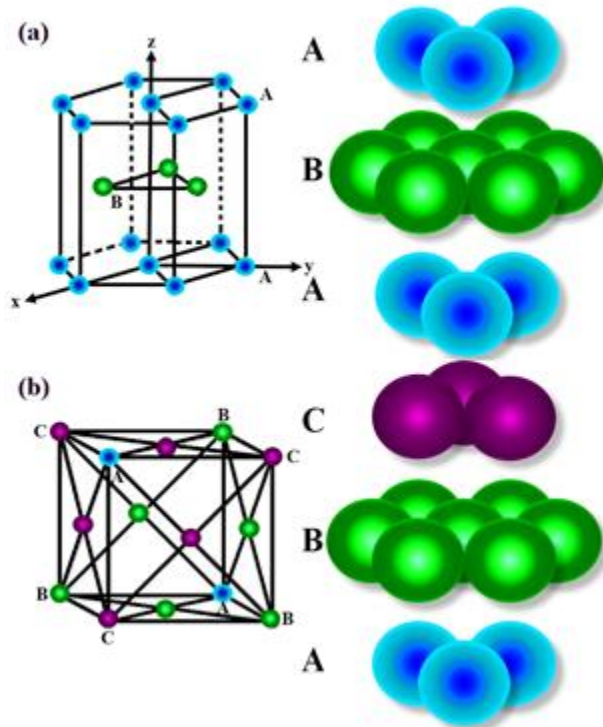


*Figure 1.11 - a) Compact hexagonal crystal structure and its stacking sequence; b) Cubic crystalline structure centered on the faces and their stacking sequence.*

Figure 1.12 shows that the stacking fault alters four layers of material. So, that zone locally becomes an HCP network with *ABAB* sequence. In thermodynamically stable FCC crystal structures, the stacking fault is a region with a high Gibbs free energy. Consequently, if the FCC network is metastable with respect to the HCP structure, the stacking fault energy will be negative, and the sliding of the Shockley partial dislocations will decrease the free Gibbs energy of the system.

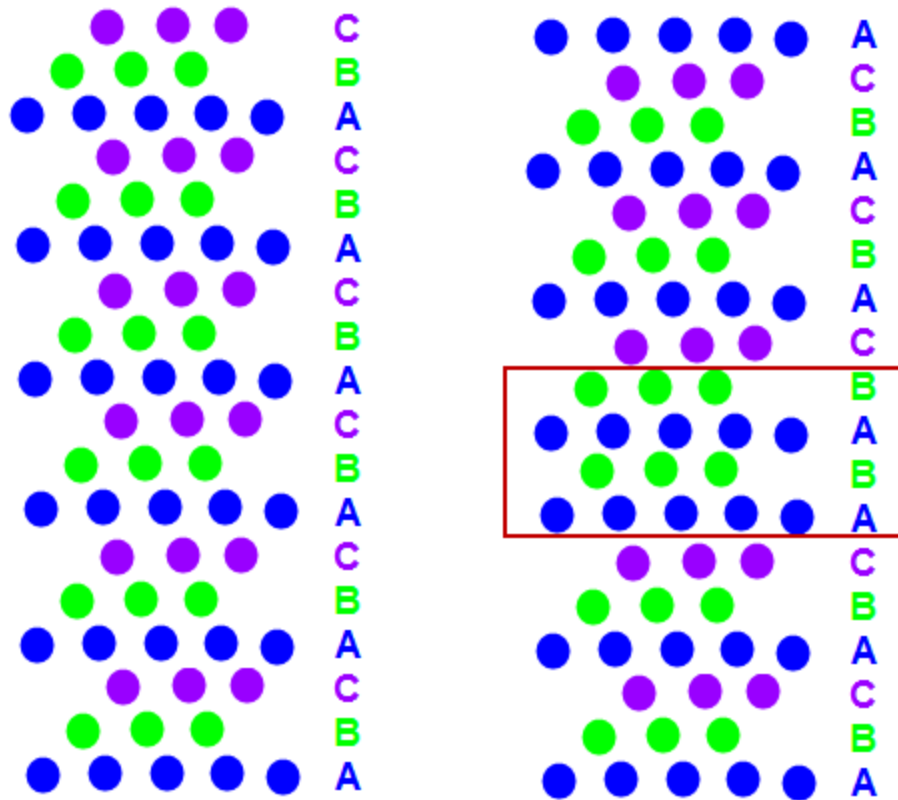


*Figure 1.12 - a) Four repetitions along the direction of the FCC crystal structure with 15 (111)-layers and one atom per layer. b) Four repetitions along the direction of the tilted crystal structure with 15 (111)-layers. A SF is located between the ninth (counting from the bottom layer) and the fourteenth layer at the cell boundary represent HCP crystal structure.*

### 1.5.1. Isothermal Transformation (Heat Treatment)

The  $\gamma \leftrightarrow \epsilon$  (FCC to HCP) transformation can be promoted by isothermal aging below  $T_c$ . In Co-base alloys, the isothermal transformation has been investigated in some detail by various authors [23, 39]. However, here is very limited information on the evolution of  $\epsilon$ -martensite during isothermal annealing in as-cast Co alloys and on their overall transformation kinetics.

Since cast Co alloys are widely used as hip and knee implants, it is essential to establish the active transformation mechanisms, as this plays a key role in improving the alloy tribological properties. In general, it is important to be able to disclose the effects of alloy segregation, carbide precipitation, heat treatment temperature, and the dendritic structure on the exhibited volume fractions and morphologies of  $\epsilon$ -martensite. In particular, the most common heat treatments for biomedical grade Co-based alloys are including a high temperature annealing above the HCP to FCC transition followed by isothermal aging. Annealing temperature plays an important role on the density of HCP embryos that can participate of the martensitic transformation during ageing. Investigations on the effects of solution treatments on the FCC to HCP isothermal martensitic transformation in Co-Cr-Mo-C alloy aged at 800 °C shows that total amount of HCP phase obtained after 5 hours ageing decreases rapidly as the solution temperature increases above 1150 °C, shown in Figure 1.13 [40]. The observed effect is further enhanced by increasing the soaking time at the solution temperature. This behavior can be explained in terms of the effects of the solution temperature and time on the nucleation kinetics of the FCC to HCP isothermal transformation. As it was discussed, the central event for the formation of any embryo is a faulting process derived from a group of appropriately spaced partial dislocations in the FCC matrix. The embryo may grow from the structural defect when the faulty energy associated with it vanishes and the dislocation energy does not increase with the movement of the mentioned dislocations. The localized high energy structural defects required for martensitic embryo formation can persist and even be created during high temperature annealing. Thus, increasing the solution temperature and time would increase the number of possible nucleation sites for the

transformation of the FCC equilibrium phase before the material is quenched to room temperature.

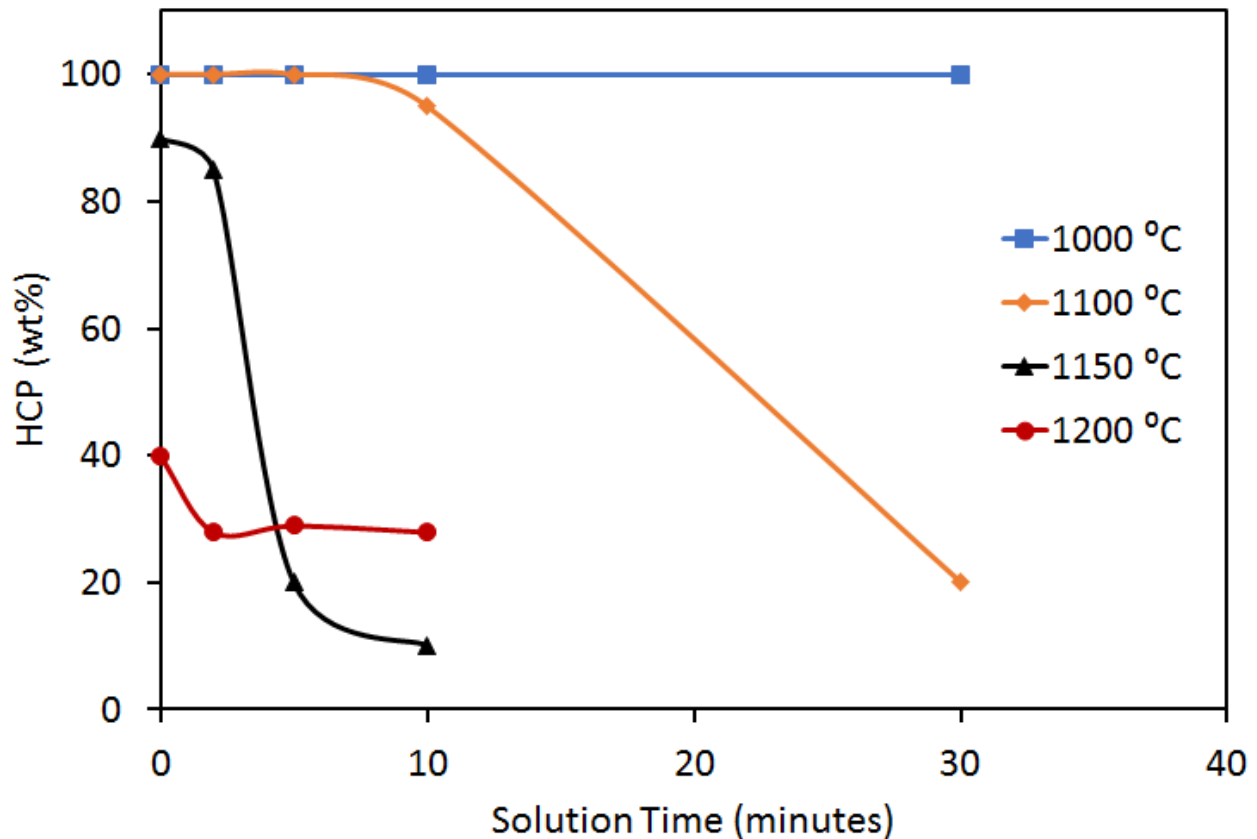


*Figure 1.13 - Effect of solution temperature and time on the amount of HCP phase formed during 5 hours of isothermal ageing at 800 °C of water quenched Co-27Cr-5Mo-0.05C [40].*

In contrast, the amount of athermal HCP martensite formed increases with increasing solution temperature. Thus, the structural changes produced by the athermal transformation appear to have a profound inhibiting consequence on the nucleation of the isothermal martensite through ageing. For instance, total carbide dissolution can be achieved in cast and wrought versions of this alloy as a function of annealing duration and temperature. Alloy aging is employed to

promote the FCC to HCP martensitic transformation and can be either applied directly from the annealing temperature or after alloy quenching. Typical isothermal aging temperatures are of the order of 650 °C to 950 °C. Isothermal aging, between 650 °C and 950 °C, of a Co-27Cr-5Mo-0.05C alloy annealed at 1150 °C causes a temperature- and time-dependent crystal structure change where the FCC metastable phase is transformed to HCP via a diffusionless martensitic transformation. At a given temperature, the progress of the transformation exhibits trend dependence with time, which can be explained in terms of the thermally activated nucleation of HCP martensite. Age hardening of this material was found to vary linearly with the amount of hcp phase present in the microstructure and does not depend on the aging temperature [41].

It is found that during alloy quenching, the numbers of HCP embryos become active nuclei for the martensitic transformation are increasing and consequently the  $\epsilon$ -martensite formation will rise. In contrast, when the alloy is directly aged from annealing, most of the HCP embryos participate in the FCC to HCP transformation; thus reducing the nucleation times as well as the times needed for a full FCC to HCP transformation significantly [32, 42].

Vander Sande and co-workers [43] have shown that upon alloy aging, the FCC phase transforms into numerous HCP plates creating markings in the cast and wrought Co-27Cr-5Mo-(0.15–0.30)C alloys after water quenched from 1230 °C. These markings (also known as bands) become increasingly thick and highly discontinuous with increasing aging times [43]. The bands were characterized by TEM as heavily faulted, martensitically transformed HCP regions with widths ranging from 5 to 15  $\mu\text{m}$ . The origin of the intergranular striations was attributed to a

diffusionless, martensitic phase transformation taking place as a result of quenching from temperatures within the FCC phase stability field. The active mechanisms involved in the development of  $\epsilon$ -martensite in Co-27Cr-5Mo-0.05C wrought alloys is related to a net reduction in the intrinsic stacking fault energy,  $\gamma_{sf}$ , to almost zero, which in turn promotes the splitting of lattice dislocations into Shockley partials to indefinite separation distances [44], section 1.4 explains this mechanism in details.

Moreover, the annealing times for carbide dissolution are strongly influenced by the carbon and nitrogen contents in the alloy, considering interactions between Shockley partial dislocations and these obstacles; it is known that precipitates suppress the  $\gamma \rightarrow \epsilon$  martensitic transformation in the parent  $\gamma$  phase [40]. In addition, the  $\epsilon$ -martensite nucleates preferentially at FCC grain boundaries, developing a morphology, which resembles “pearlite,” a constituent typical of the classical Cahn and Hagel model for austenite decomposition in carbon steels, Figure 1.14 shows the example of HCP formed in Co alloy. This appearance is due to the formation of carbides simultaneously with the development of  $\epsilon$ -martensite. However, the microstructural evidence does not support this interpretation. Rajan [14] showed by TEM that the structural defects which are involved in the formation of stacking-fault martensitic embryos during isothermal aging of low stacking fault energy Co-Cr-Mo-C alloys are incoherent twin boundaries and twin-twin intersections. Nucleation of martensite on these structural defects is consistent with the experimental observation that increasing the FCC grain size from 35 to 100  $\mu\text{m}$  does not have a significant effect on the kinetics of the transformation. In the Co-27Cr-5Mo-0.05C alloy investigated in the [41] work, carbide precipitation was not detected by SEM. This is probably

due to the lower carbon content in the alloy and to the fact that the temperature of the heat treatment in the FCC phase stability field (1150 °C) was not high enough to cause carbide dissolution. Thus, carbide re-precipitation during quenching or aging is less likely to have occurred in the present material. This conclusion is supported by the observations of Taylor and Waterhouse [45], in most Co-Cr-Mo-C alloys, carbide dissolution takes place at temperatures are 1210 °C.

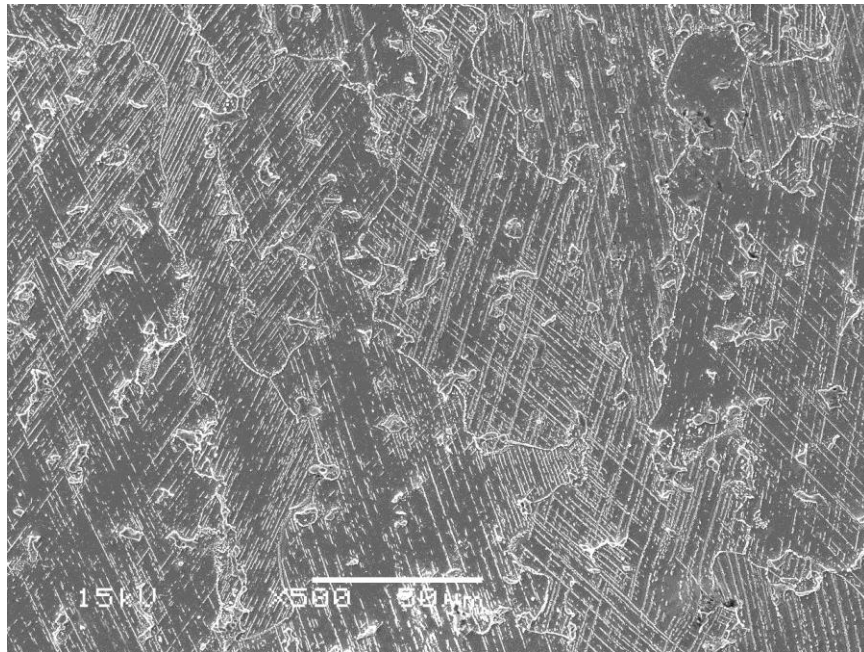


*Figure 1.14 - Example of HCP  $\epsilon$ -martensite formation on Co-Cr-Mo-C alloy, aged at 900 °C for 10 hours.*

Figure 1.15 shows the Transformation-Temperature-Time (TTT) diagram for the isothermal FCC (metastable) to  $\epsilon$ -HCP phase transformation in Co-27Cr-5Mo-0.05C alloy [41] for materials water quenched from 1150 °C to 25 °C prior to aging. By comparing the TTT diagrams in 1.13, water quenching from 1150 °C and reheating to the aging temperature retards the FCC

(metastable) to  $\epsilon$ -HCP isothermal transformation by nearly one order of magnitude in time. In addition, when the material is cooled directly from the solution to the aging temperature, the start of the transformation requires only about 5 minutes at temperatures within the range from 800 °C to 850 °C. Aging treatments performed outside this temperature range cause a significant decrease in the rates of transformation.

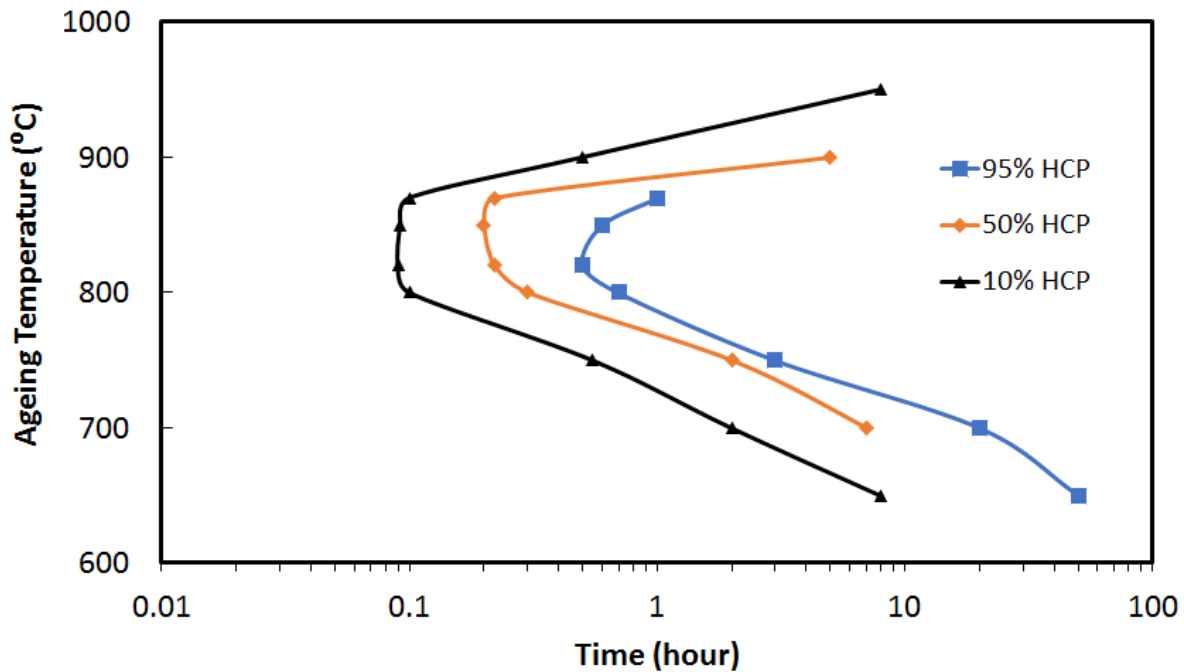


*Figure 1.15 - Transformation-Temperature-Time (TTT) diagram for the isothermal FCC to HCP transformation in Co-27Cr-5Mo-0.05C alloy [41].*

These observations suggest that thermal activation, to overcome the structural barriers for isothermal martensite nucleation during aging of Co-27Cr-5Mo-0.05C, is most effective at temperatures between 800 °C and 850 °C. However, water quenching from 1150 °C to room temperature prior to aging causes a significant decrease in the transformation rates observed.

This indicates that the additional quenching has a strong negative effect on the nucleation kinetics of isothermal martensite during aging. H. F. Lopez et al. [44] proposed an isothermal annealing heat treatment on Co-Cr-Mo-C alloy which was based on annealing at 1150°C, water quenched, and then isothermally aged at 700°C to 900°C, resultant TTT curves plotted by using quantitative measurements of HCP phase as a function of ageing temperature and time, Figure 1.16. Notice the enhancement of transformation rate between 800°C to 850°C. Also, these results show that by increasing the ageing time the amount of formed HCP phase will increase.

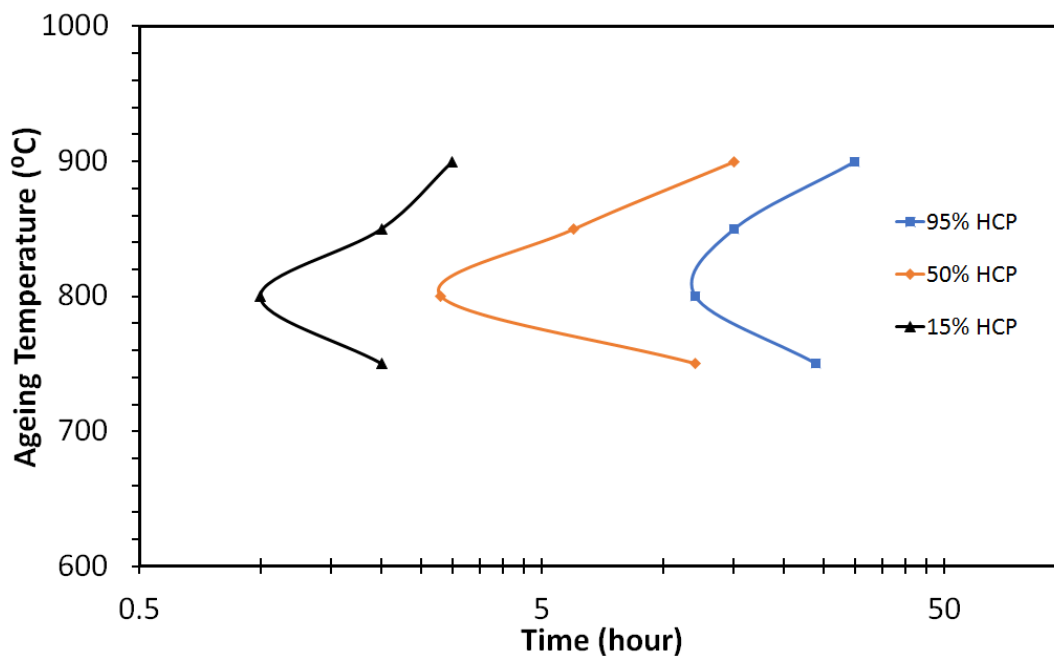


*Figure 1.16 - TTT diagram for material annealed Co-Cr-Mo-C alloy at 1150°C, water quenched, and then isothermally aged at 700°C to 900°C [44].*

This behavior can be explained by considering the possible effects of quenching and reheating to the aging temperatures on the structure of the metastable FCC phase retained at room

temperature. Water quenching generates internal thermal stresses and it may also cause partial transformation of the FCC equilibrium phase to HCP martensite, introducing further internal phase transformation stresses. These internal stresses must be relieved during reheating to the aging temperature. Rajan and Vander Sande [46] have shown that the main room-temperature plastic strain-producing mechanisms in cast Co-Cr-Mo alloys are FCC twinning and stacking-fault formation. Additionally, transformation induced plasticity also plays an important role as a strain accommodation mechanism in low-carbon Co-Cr-Mo alloys. Therefore, if at least some of these deformation mechanisms are active during reheating to the aging temperature, plastic relaxation of the internal stresses may lead to a significant modification of the number and distribution of lattice defects in the structure of the metastable FCC phase. This evolving defect structure may hinder the formation of the specific dislocation configurations [41] needed for the creation of HCP martensite embryos and impose additional obstacles to the motion of partial dislocations required for isothermal martensite nucleation during aging. These arguments, therefore, could explain the slower transformation kinetics observed in material water quenched prior to aging (Figure 1.13).

Figure 1.17 shows the TTT diagram for Co-based alloy in wrought and as cast conditions ageing directly from annealing temperature. The results of this study done A. J. Saldivar [41] shows that most of the  $\epsilon$ -embryos generated by annealing become active in the  $\epsilon$ -martensite growth process. Consequently, conditions for maximum transformation rates are developed when quenching is not implemented in the heat treatment, this can be understood by observing the

effect of heat treatment as direct aging after annealing reduces significantly the transformation times.

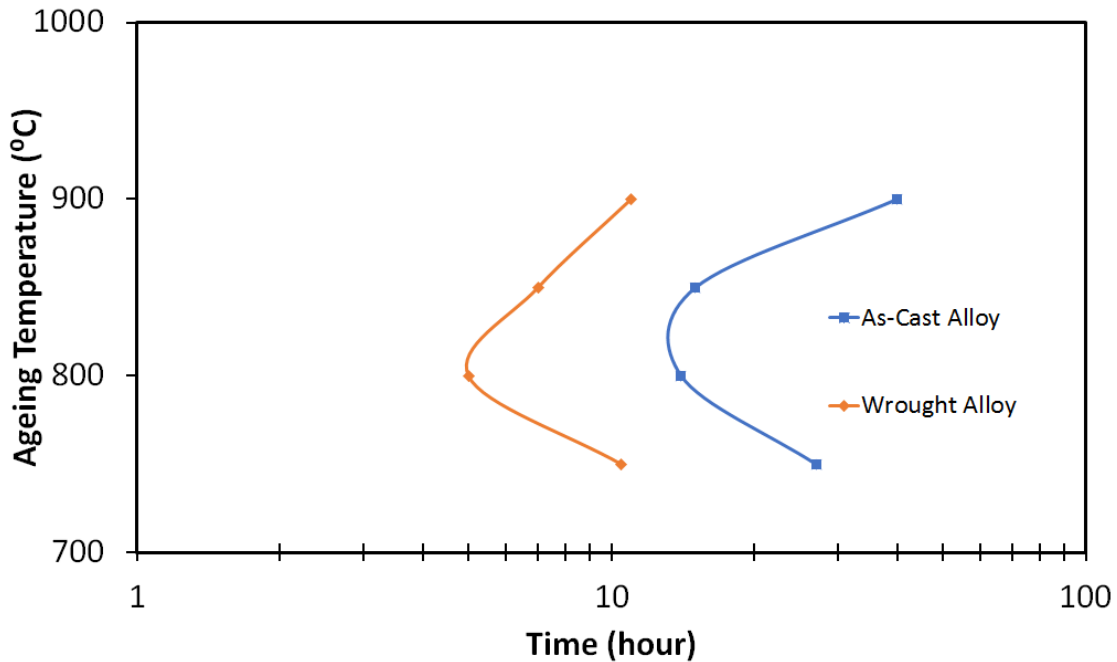


*Figure 1.17 - TTT diagram for Co-based alloy in wrought and as cast conditions ageing directly from annealing temperature [41].*

In addition, sample dimensions have a large effect on the transformation times in a cast Co-alloy. At relatively large Co-alloy bar diameters, a reduction in the formation of potential nucleation sites is expected as a result of higher segregation of alloying elements during solidification. The isothermal transformation kinetics for  $\epsilon$ -martensite can be followed by using a modified version of the Avrami equation, described in the work of Pati and Cohen [47] as following:

$$\frac{df}{dt} = nVv \exp\left(\frac{-Q}{RT}\right)$$

*Equation 1.2*

where  $f$  is the volume fraction of martensite,  $n$  is the density of nucleation sites ( $10^6 \text{cm}^{-3}$ ),  $\nu$  is the nucleation attempt frequency ( $10^{11} \text{s}^{-1}$ ),  $R$  is the universal gas constant,  $T$  is the absolute temperature, and  $V$  is the instantaneous mean martensite plate volume.

The kinetic aspects of the FCC to HCP transformation suggest that the nucleation stage of the transformation is a thermally activated phenomenon. Olson and co-workers [42] have considered these types of transformations and proposed an analytical model for the FCC to HCP transformation. From their work, it is evident that the FCC to HCP martensitic transformation is strongly influenced by the alloy stacking fault energy of the HCP phase,  $\gamma'_{HCP}$ . As the  $\gamma'_{HCP} \rightarrow 0$  in these alloys, a given stacking fault becomes unstable and it is expected to extend indefinitely, increasing the probability of  $\epsilon$ -martensite formation. Accordingly, a negative  $\gamma'_{HCP}$  will favor a spontaneous development of groups of partial dislocation arrays (HCP nuclei). Olson and Cohen [42] estimated that the probable density of these types of defects is of the order of  $10^5$ - $10^7/\text{cm}^3$ . Therefore, solute elements such as C, N and Ni that increase the  $\gamma'_{HCP}$ , severely limit the martensitic transformation and consequently promoting the stability of the FCC phase at room temperature. Considering substitutional solutes, it is well known that BCC elements, such as Mo, W, and Cr, tend to stabilize the HCP crystal structure by reducing the  $\gamma'_{HCP}$  while Ni has the opposite effect. The solubility of carbon and nitrogen in Co-base alloys is negligible at room temperature [48]. Considering interstitial elements such as C and N, it is found that they strongly hinder the FCC to HCP transformation due to their effect on increasing the  $\gamma'_{HCP}$ . Therefore, for the FCC to HCP transformation to happen at the isothermal aging temperatures these solutes

must segregate at the FCC to HCP interphase boundaries. In turn, during the martensitic transformation carbide and carbonitride phases are concomitantly formed as the transformation front advances giving rise to the lamellar or fibrous microstructural features. Nitrogen enlarges the field of stability of the  $\epsilon$ -phase. It is mentioned before that the ability of a stacking fault to extend indefinitely will result into martensitic transformation. On the other hand, this process strongly depends on the solute content in these faults. This very well can be explained by the lack of HCP martensite nucleation at carbide interfaces and at most of the dendrite boundaries of an as-cast cobalt alloy [44].

Considering the development of  $\epsilon$ -embryos from high-temperature anneals after quenching will reveal additional evidence for the role of interstitials on the FCC $\rightarrow$ HCP transformation. In this condition, about 20% of martensite are shown after quenching which is suggesting that when the content of interstitials is relatively low, the nucleation barrier for athermal martensite is reduced. By aging process, isothermal  $\epsilon$ -martensite will be developed, indicating that the kinetic barriers for lattice dislocation splitting are no longer effective in stopping the transformation. Apparently, at the aging temperatures, there is enough thermal energy for interstitial diffusion away from the HCP lattice and into dislocation cores or interfaces. Therefore, it is expected that the magnitude of  $\gamma'_{HCP}$  will drop to values that enable active growth events with indefinite splitting of Shockley partials. Since there is almost no carbon or nitrogen solubility in the HCP cobalt structure interstitials must diffuse away from the HCP matrix to achieve a total isothermal transformation. Nevertheless, as  $\epsilon$ -martensite growth continues, a concentration of interstitial elements at the

HCP/FCC transformation front is predictable. As a result, interstitials will be moved sideways to precipitate interphase carbide/carbonitride supersaturation at locations such as stacking fault intersections and dislocation cores. Thus, the type and growth of carbides will determine martensite growth. Accordingly, the development of zigzag pattern of interphase precipitates confirms the effectiveness of interstitial removal from the growing  $\epsilon$ -martensite, Figure 1.14.

The growth of carbides/carbonitrides at the HCP/FCC interphase is a highly coordinated process. In this process, coherency strains can develop at the HCP/precipitate and FCC/precipitate interphases. Hence, the favored precipitate phases that are developed would minimize the energy barriers associated with any lattice mismatches. In this case, the main barrier for precipitate growth is related to the actual coherency strains at the HCP/precipitate interphase. Taylor and Waterhouse [45] have found that  $M_{23}C_6$  carbides, which are FCC type with a lattice parameter similar to FCC-Co, are the typical carbides developed in high carbon cast cobalt alloys. Alternatively, other carbide/carbonitride phases can develop as long as there is a habit plane where the transforming HCP phase is under minimal coherency stresses. Figure 1.18 shows the development of discontinuous strings of what seems to be carbides in a low carbon wrought Co alloy. These carbides were not identified as  $M_{23}C_6$  carbides but as the zeta carbide ( $\zeta$ ), this carbide belongs to the spatial group and possesses a trigonal structure.

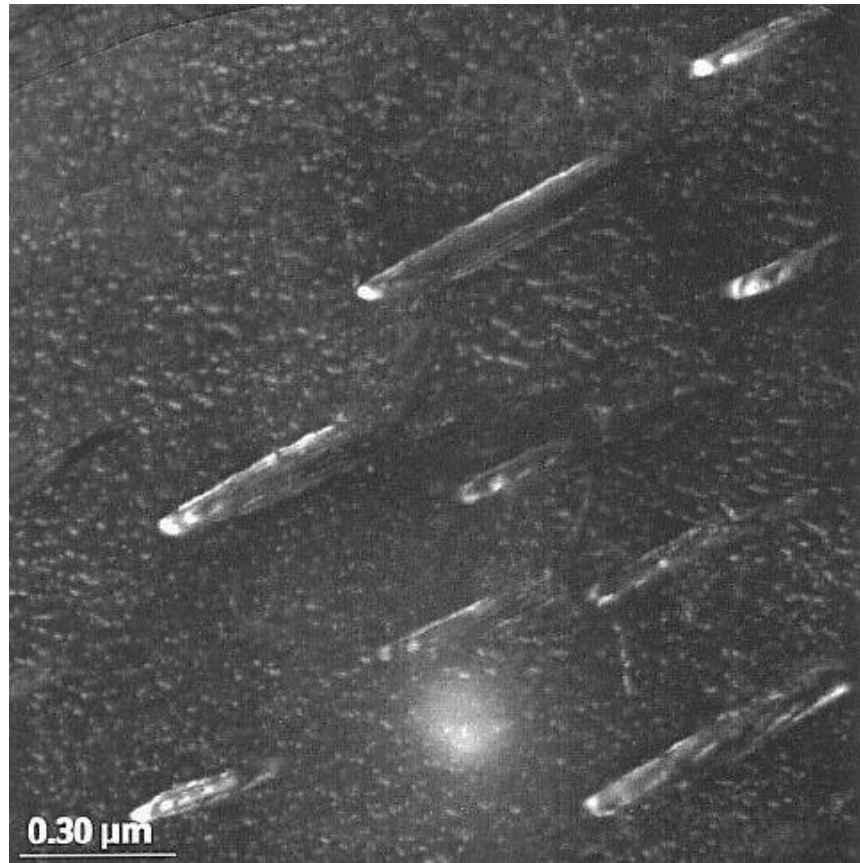


*Figure 1.18 - TEM micrograph of discontinuous strings of carbides in a C0-27Cr-5Mo-0.05C alloy after ageing at 1123 K for 1 hour [26].*

### **1.5.2. Athermal Transformation**

In addition, the transformation of  $\gamma$  (FCC)  $\rightarrow$   $\epsilon$  (HCP) takes place by a martensitic athermal reaction. In particular, in athermal transformations the amount of transformed martensite depends primarily on the quenching temperature and not on the residence time at this temperature. Experimentally, it has been found that in conventionally solidified Co-Cr-Mo-C alloys the reported amounts of athermal  $\epsilon$ -martensite are relatively small, not exceeding 20 vol. % in most cases [49]. The limited extent of athermal martensite induced in Co-Cr-Mo alloys has

been attributed to the lack of enough defects necessary for the spontaneous formation of  $\epsilon$ -embryos during alloy cooling from the  $\gamma$ -phase [50].

Athermal reaction is controlled by the distribution of faulting defects which act as effective nucleation sites for  $\epsilon$ -martensite embryos. These faulting defects including tilt boundaries, twin intersections, incoherent twin boundaries or incoherent inclusion interfaces expedite the formation of  $\epsilon$ -martensite embryos by having a long-range stress field. Olson et al. [42] have shown that the spontaneous formation of  $\epsilon$ -martensite embryos can be achieved when the alloy stacking fault energy becomes zero or negative. The nucleation defect being a faulting mechanism consisting of a group of lattice dislocations where the motion of a Shockley partial on every second FCC closed packed plane gives rise to an  $\epsilon$ -phase nucleus. Yet, the estimated density of the proper faulting defects is of the order of  $10^5$ - $10^7/\text{cm}^3$ , which explains the sparse amounts of precipitated athermal martensite in cobalt based alloys [42]. To better understand the martensitic transformation mechanism in Co-Cr alloys, the nature of Shockley's partial dislocations must be considered and understood. In the work of Olson and Cohen [42], the classical nucleation theory was used in identifying energetic conditions for the spontaneous nucleation process of martensite embryos. In their work, the critical condition for spontaneous embryo nucleation was taken to be zero ( $\gamma'_{SF} = 0$ ). In addition, the critical embryo size was given in terms of the number of dissociated lattice dislocations in the inclusion. In the proposed analysis, minimal energy conditions for embryo nucleation were found as a function of the embryo geometry (size and thickness) by using the method proposed by Easterling and Thölén [51].

Consider a martensite embryo plate (such as the ones found in the directionally solidified Co-20Cr alloy) which is expected to nucleate upon cooling. Energetically, various workers [42, 51] have suggested that martensite nucleation from a defect occurs as a result of the propagation of existing strain fields rather than energy consumption by the phase change. In this context, the structural defects capable of acting as nucleation sites must possess long range stress fields [42, 51]. In addition, consider a Bain distortion which gives rise to martensite from the austenitic matrix with a minimum of atomic displacements and an invariant plane condition. In the case of a small inclusion, lattice invariant deformation might not be required as the inclusion is under the strain field of a defect. Accordingly, the total energy associated with the nucleation process is given by [51].

$$\mathbf{E}_{tot} = \mathbf{E}_{surf} + \mathbf{E}_{strain} + \mathbf{E}_{chem} + \mathbf{E}_{int} \quad \text{Equation 1.3}$$

Notice that the total energy incorporates (a) the coherent interfacial energy between the austenite matrix and the martensite embryo ( $\mathbf{E}_{surf}$ ), (b) coherency strains due to a change in lattice parameters ( $\mathbf{E}_{strain}$ ), (c) the difference in chemical free energy for the austenite-martensite transformation ( $\mathbf{E}_{chem}$ ) and (d) interaction between the strain field of a Shockley partial and the strain field of the martensite embryo ( $\mathbf{E}_{int}$ ). Since  $\epsilon$ -martensite embryos result from the dissociation of a number of properly spaced lattice dislocations, the development of stable nuclei

is then plausible whenever a net energy reduction occurs through the incorporation of a dissociated dislocation onto the critically sized martensite embryo.

Considering the geometry for martensite nuclei assumed by Easterling and Thölen [51], a single martensite embryo possessing a thin ellipsoidal geometry can be defined by a semi-thickness  $c$ , a radius  $a$  and volume  $V$ . The thin ellipsoidal geometry for the martensite embryo is shown in Figure 1-19. This figure also contains a top view of the ellipsoidal embryo which resembles a flat plate, as well as a front view resembling a needle-shaped inclusion.

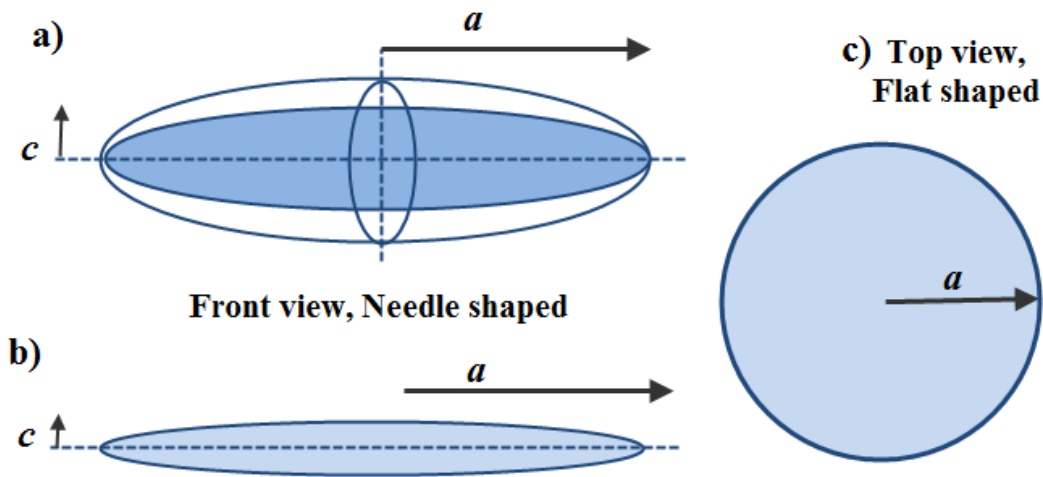


*Figure 1.19 - (a) Martensite embryo with thin ellipsoidal geometry,  $c$  and  $a$  corresponds to semi-thickness and radius, respectively, (b) Top view for martensite embryo that resembles a flat plate, (c) In front view for martensite embryo that resembles a needle shaped morphology [52].*

In addition, it is assumed that the transformation can be expressed by a simple shear of magnitude  $S$  and that the interaction of the strain field of the Shockley partial is compatible with

the strain field of the martensite embryo. Under these assumptions, Eq. (1.3) can be rewritten as [51].

$$E_{tot} = 2\pi\sigma a^2 + \frac{\pi\mu}{2} \left(\frac{S}{2}\right)^2 \frac{(2-\nu)}{(1-\nu)} \frac{c}{a} V - \Delta G_V V - \frac{\pi^2 \mu S b}{4} \frac{2-\nu}{1-\nu} a c \quad \text{Equation 1.4}$$

In the above expression, the total energy is a function of the surface energy ( $\sigma$ ), the shear modulus of the austenite matrix ( $\mu$ ), Poisson's ratio ( $\nu$ ), the volumetric chemical free energy difference ( $\Delta G_V$ ) and the magnitude of the Burgers vector intrinsic to the Shockley partial ( $b$ ). The value of  $\sigma$  used is minimum as it corresponds to a fully coherent interface but increases as the interface becomes semi-coherent. According to various workers, in transition metals and alloys the value of  $\sigma$  varies from 0.005 to 0.015 J/m<sup>2</sup> [53]. In addition, the magnitude of  $\mu$  is of the order of 10<sup>10</sup> Pa [54] Whereas  $\nu$  is around 1/3 [51].

The shear transformation can be determined by the strain over the inclusion; in this instance, the various parameters used in Eq. (1.4) are given in Table 1.3. The total energy associated with the athermal martensite embryo was estimated using the data reported by Yamanaka and co-workers for a Co-29Cr-Mo alloy [55] (see Table 1.4). Moreover,  $\Delta G_V$  is highly sensitive to the molar weight of the elements involved, as well as, to the austenite-martensite transformation temperature. Figure 1.20 shows the total energy surface contour predicted by Eq. (1.4) by arbitrary varying the  $c$  and geometrical martensite plate parameters. From this graph, minimal energy conditions required for embryo nucleation can be found including critical parameters that satisfy minimal energy conditions (as described in the minimal energy subsection). In addition,

Figure 1.20 shows the critical dimensions needed for martensite nucleation from an austenitic matrix in other alloy systems.

*Table 1.3 – Properties of Co-20Cr [50]*

Property	Value in SI unit	Reference
$S$	0.2	[51]
$\sigma$	$0.0075 \text{ J/m}^2$	[56]
$\mu$	$8.8 \times 10^{10} \text{ Pa}$	[56]
$\nu$	0.28	[56]
$b$	$0.145 \times 10^{-9} \text{ m}$	[56]
$\Delta G_V$	$2.098 \times 10^6 \text{ J/m}^3$	

*Table 1.4 – Computed  $\Delta G_V$ , energy barrier values and critical parameters for athermal martensite nucleation in selected alloys [50]*

Alloy	$\Delta G_V \text{ (J/m}^3\text{)}$	Energy barrier (J)	$c \text{ (nm)}$	$a \text{ (nm)}$
Co-20Cr	$2.098 \times 10^6$	$5.692 \times 10^{-12}$	6.953	20.176
Co-29Cr-6Mo	$7.801 \times 10^6$	$6.065 \times 10^{-12}$	1.652	938.84
Steel	$1.740 \times 10^8$	$6.650 \times 10^{-12}$	2.044	53.331

Minimal energy conditions which are needed to overcome the energy barrier for nucleation can be estimated by a partial derivation of Eq. (1.4) [51] with respect to the  $a$  and  $c$  parameters. As a result of this derivation, a system of two coupled equations is obtained, which can be described by the array in Eq. (1.5). In this expression, each partial derivation evaluated for the critical parameters  $c_{\text{crit}}$  and  $a_{\text{crit}}$  must be equated to zero. The equations for the critical parameters obtained by this method thus provide the semi-thickness and radius that satisfy the minimal

energy state. A minimal energy expression can then be obtained by substitution of the critical parameters  $c_{crit}$  and  $a_{crit}$  into the energy equation, Eq. (1.4).

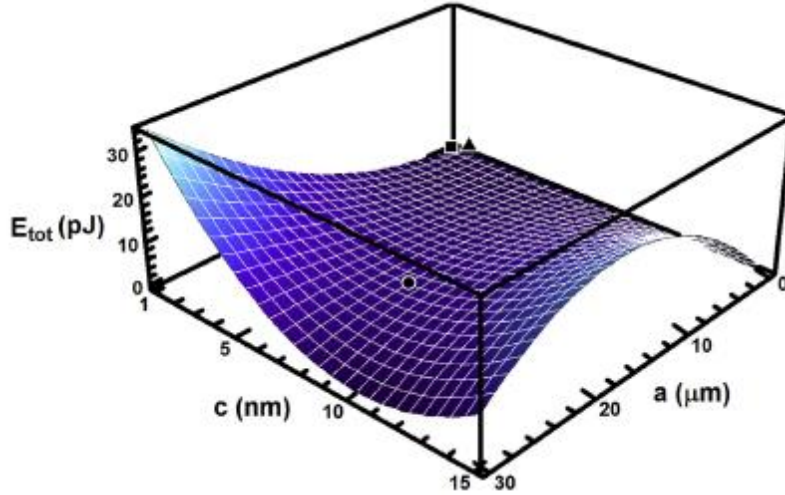


*Figure 1.20 - Energy surface generated by arbitrary variation of  $c$  and a plate dimensions in Eq. (2). Minimal energy conditions for the Co-20Cr alloy, a Co-29Cr-6Mo alloy and a Fe-Cr-Ni steel are marked by a circle, a square and a triangle, respectively [50].*

$$\begin{cases} \left. \frac{\partial}{\partial c} E_{tot}(a, c) \right|_{\substack{c=c_{crit} \\ a=a_{crit}}} = 0 \\ \left. \frac{\partial}{\partial a} E_{tot}(a, c) \right|_{\substack{a=a_{crit} \\ c=c_{crit}}} = 0 \end{cases} \quad \text{Equation 1.5}$$

In the case when there is no interaction between the strain field of the Shockley partial dislocation and the strain field of the martensite embryo ( $E_{int} = 0$ ), critical parameters that satisfy Eq. (1.5) are given by Eqs. (1.6) and (1.7).

$$c_{crit} = \frac{2\sigma}{\Delta G_V} \quad \text{Equation 1.6}$$

$$a_{crit} = \frac{5\pi\sigma\mu}{(\Delta G_V)^2} \left(\frac{S}{2}\right)^2 \quad \text{Equation 1.7}$$

Under these assumptions, the minimal energy condition can be described by the expression proposed by Easterling and Thörlén [51]:

$$E_{min} = \frac{50\pi^3}{3} \frac{\sigma^3\mu^2}{(\Delta G_V)^4} \left(\frac{S}{2}\right)^4 \quad \text{Equation 1.8}$$

Rapid solidification is an effective method to increase the density of faulting defects and consequently a prompt transformation of  $\gamma \rightarrow \epsilon$ . A.L. Ramirez-Ledesma et al. [50] used rapid solidification method to cast Co-20%Cr alloy and they found fully  $\epsilon$ -martensite matrix at the cooling rate of 278 K/s. According to their results, development of an extremely large amount of stacking faults and stacking fault intersections, including  $\epsilon$ -martensite have been observed. In this regard, a clear advantage of employing rapid solidification is the elimination of any detrimental effects associated with interdendritic segregation. Figure 1.21 shows an SEM micrograph and corresponding X-ray mapping of chromium in a region of a directionally solidified columnar dendrite. Notice that Cr is uniformly distributed with no evidence for solute (Cr) segregation in the interdendritic regions of the investigated alloy.

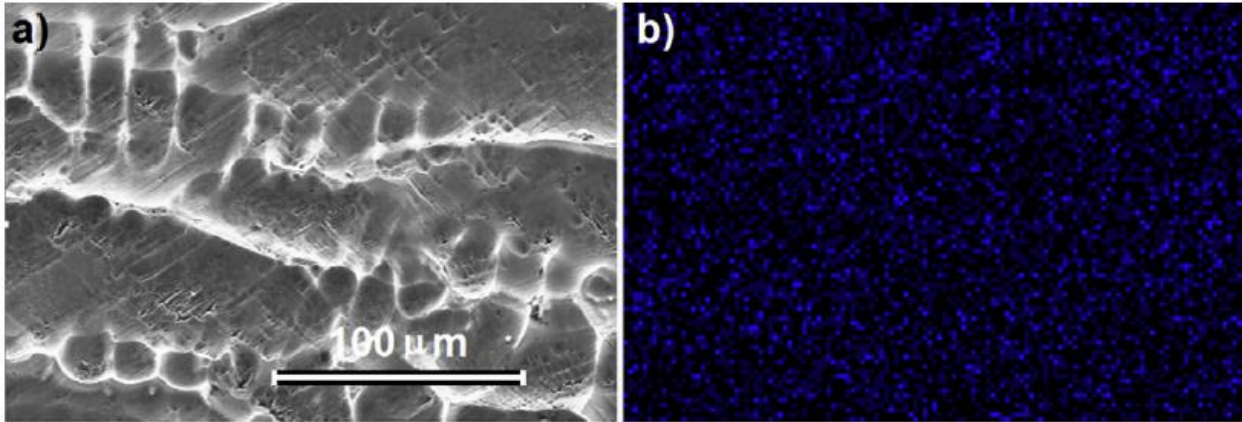


*Figure 1.21 - (a) SEM micrograph of the as-chill cast Co-20Cr alloy showing a part of columnar dendrites directionally solidified, (b) X-ray mapping of Cr (chromium) [50].*

J. L. Acevedo-Dávila et al. [57] applied laser welding on Co-Cr-Mo-C alloy and studied the effect of surface modifying on microstructure and wear properties of alloy. Results exhibit changing the microstructure of alloy from HCP-FCC to fully FCC with a finer cellular structure, also improvement in wear properties has been observed.

### **1.5.3. Strain Induced Transformation (SIT)**

It is found that the density of striations, representing  $\epsilon$ -martensite phase, increases with the amount of plastic straining [58]. The increase in the density of striations is related to the formation of strain induced  $\epsilon$ -martensite. In addition, the kinetics of the strain induced transformation (SIT) of  $\epsilon$ -martensite can be followed by using a modified version of the model proposed by Olson and Cohen [42]. From this model, a sigmoidal shape expression has been proposed that satisfactorily predicts the volume fractions of SIT  $\epsilon$ -martensites as a function of

plastic strain. Moreover, it is found that the amount of SIT  $\epsilon$ -martensite is strongly influenced by the alloy grain size, with increasing hardening rates at smaller grain sizes. In high carbon Co-Cr-Mo-C alloys, the effect of alloy pre-straining on the isothermal  $\epsilon$ -martensite transformation does not slow down the transformation [58]. In this case, 8 hours are sufficient to promote 100 %  $\epsilon$ -martensite in specimens pre-strained 10 and 20 % and aged at 850°C for various times. The acceleration of the  $\epsilon$ -martensite transformation is attributed to the formation of heavy faulted regions and intersection of striations during the SIT. In particular, a build-up of carbon at stacking fault intersections (solute drag) is expected to lead to rows or strings of fine carbides thus removing carbon supersaturation in the HCP-phase. In turn, this will favor  $\epsilon$ -martensite growth under isothermal aging leading to reduced aging times. Enhancing the strain hardening is crucial for improving the strength, ductility, and fatigue properties of these alloys. Recently, manufacturing of high-strength Co-Cr-Mo alloys with a particular focus on their peculiar phase stability have been studied. Studies revealed that Co-28Cr-6Mo alloys with chemical composition complies with the ASTM F1537 standard for surgical implants, have an unusually high equilibrium temperature between the  $\gamma$ -and  $\epsilon$ -phases (i.e.,  $T_0 \sim 1173\text{K}$ ) [49, 56], and thus display an extremely low stacking fault energy even at hot deformation temperatures. In such circumstances, a significant increase in dislocation density can be obtained via multi-pass hot deformation, which involves repeated introduction of relatively small amounts of strain to the alloys at elevated temperatures [49]. Furthermore, a substantial increase in the number of stacking faults (SFs) in the  $\gamma$ -matrix occurs during multiple hot deformation, resulting in a significant strengthening of the alloys [55]. An important point to note is the influence of these latticed effects on the performance of the alloys. It is well known that a strain-induced

martensitic transformation (SIMT) from FCC  $\gamma$ -matrix to HCP  $\epsilon$ -phase occurs in biomedical Co–Cr–Mo alloys if plastic deformation is introduced, and this transformation influences the mechanical properties [15, 48, 49], cold workability [55], and wear resistance [59] of the alloys. The  $\gamma \rightarrow \epsilon$  SIMT has been intensively investigated in austenitic steels, especially in high manganese steels. Notably, Tomota et al. [60] determined that  $\epsilon$ -martensite will effectively enhance strain hardening, and is thus promising for obtaining prominent transformation-induced plasticity (TRIP) effects. Controlling the  $\gamma \rightarrow \epsilon$  martensitic transformation of Co–Cr–Mo alloy by varying the chemical composition requires further verification from a biocompatibility perspective and is therefore an obstacle to its practical application. Significantly, the  $\gamma \rightarrow \epsilon$  SIMT occurs via the regular overlap of SFs, bounded by Shockley partial dislocations, in every other  $\{111\}_{\gamma}$  plane [61]. Therefore, it can be said that the lattice defects present in the metastable  $\gamma$ -phase matrix can alter the subsequent SIMT behavior and, ultimately, the performance of the alloys. However, the effect of pre-existing defects in the parent phase on the martensitic transformation is generally considered in neither theories [62, 63] nor experiments.

High entropy alloys (HEAs), such as Co-based or multi-principal-component alloys [64] show remarkable properties, mainly for their twinning induced plasticity (TWIP) effect, or transformation induced plasticity (TRIP) effect, due to overcoming the strength-ductility trade-off in the composition design of alloys. Generally, low stacking fault energy (SFE) HEAs with face-centered cubic (FCC) single phases are more likely to deform by twinning, with increased strain hardening rates [65]. With the decreasing temperature, the very low SFE values at

cryogenic conditions suggest that the possible presence of the TRIP effect via calculation. Nano-twins and hexagonal close packed (HCP) lamellae are observed to coexist in Co-Cr-Ni at 77 K, suggesting a possible evolution of the deformation mechanism from nano-twinning to phase transformation in equal molar Co-Cr-Ni. Usually, the SFE of HEAs were experimentally measured by weak-beam dark-field transmission electron microscopy or theoretically calculated by first principles calculations, such as the exact muffin-tin orbitals (EMTO) method.

### 1.6. Importance of the HCP Crystal Structure for Development of Low-Friction Joint Replacement Implants

The friction coefficient ( $\mu$ ) between two materials with different strengths subjected to adhesive wear is given by:

$$\mu = \frac{\tau}{\sigma_y - \frac{2E_{ab}\cot\theta}{r}} \quad \text{Equation 1.9}$$

Where  $\tau$  is the interfacial shear stress,  $\sigma_y$  is the yield strength of the softer material, and  $\theta$  and  $r$  are parameters defining the geometry of the region plastically deformed in the softer material.

The term  $E_{ab}$  is the work of adhesion between the materials a and b and is given by  $(G_a + G_b - G_{ab})$ , where  $G_a$  and  $G_b$  are the surface free energies of the materials a and b, respectively.  $G_{ab}$  is the interfacial free energy. Let Eq. 1.9 be valid for the conditions of friction between ultrahigh-molecular-weight polyethylene (UHMWPE) and a Co-Cr-Mo-C alloy. Since the friction coefficient depends on the strength and hardness of the softer material, the increased hardness

caused by the  $\gamma \rightarrow \epsilon$  transformation does not really play a significant role in improving the tribological behavior of the material. In contrast, an increase of the metal/polyethylene interfacial free energy would result in a reduction of the friction coefficient due to the reduction of the work of adhesion at the interface. Moreover, increasing the interfacial free energy would also improve the hydrophilic characteristics of the interface and would also increase its ability to retain a film of liquid lubricant. Improved lubrication conditions at the interface decrease the interfacial shear stress and would cause a further reduction of the friction coefficient. These arguments could be applied for the case of HCP Co-27Cr-5Mo-0.05C/UHMWPE implant prostheses. In this case [26] the increase in interfacial free energy would result from:

- The increased number of lattice defects created to accommodate the shape change associated with the formation of isothermal HCP martensite
- The orientation differences between martensite lamellae at the surface of the material
- The surface residual stresses generated by expansion and contraction during heating and cooling.

Thus, low-friction articular implants could be manufactured using isothermally aged, low-carbon HCP Co-Cr-Mo-C wrought alloys.

### **1.7. Corrosion of Co alloy**

The surrounding media of the metallic implants (body fluids) plays an important role on its durability. This fluid is one of the most aggressive environments due to the high concentration of chloride ions and organic compounds. Main components of body fluids are salts (NaCl, KCl, and

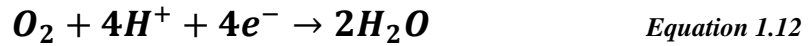
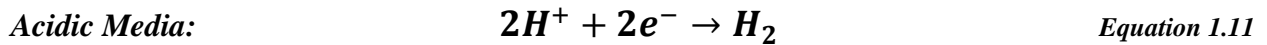
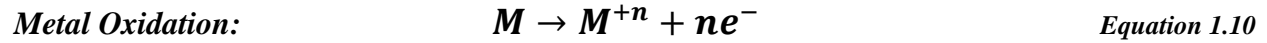
CaCl<sub>2</sub>), organic molecules (proteins) and inorganic species (phosphates). The general composition of human biological fluids (plasma or serum and synovial fluid) is shown in Table 1.5. Fluid properties and composition can readily change as a result of disease, aging, and drug ingestion [66].

*Table 1.5 - General chemical composition of the human biological fluids [66]*

Compound	Plasma (Serum)	Synovial (Fluid)
Bicarbonate	25-30 mM	-
Calcium	2.12-2.72 mM	1.2-2.4 mM
Chloride	100-108 mM	87-138 mM
Phosphorous (total)	2.87-4.81 mM	-
Potassium	3.5-4.7 mM	3.5-4.5 mM
Sodium	134-143 mM	133-139 mM
Amino acids	20-51 mg mL <sup>-1</sup>	-
Glucose	650-966 mg mL <sup>-1</sup>	-
Uric acid	30.5-70.7 mg mL <sup>-1</sup>	39 mg mL <sup>-1</sup>
Water	930-955 mg mL <sup>-1</sup>	960-988 mg mL <sup>-1</sup>
Albumin	37.6-54.9 mg mL <sup>-1</sup>	6-10 mg mL <sup>-1</sup>
IgG	6.4-13.5 mg mL <sup>-1</sup>	1.47-4.62 mg mL <sup>-1</sup>
Fibrinogen	2-4 mg mL <sup>-1</sup>	-

Due to the aggressive biological environment in which biomaterials are in contact and to the nature of metals, it is necessary to understand the corrosion phenomena that these materials experience. The corrosion process is an electrochemical reaction occurring at the interface of the metal (M) with the environment resulting in the loss of the material or in the dissolving of one of the constituents of the environment into the material. The oxidation of the metal is coupled to the

reduction of the oxidizing agent (environment) which takes the electrons from the oxidation reaction. Following equations show the reduction reactions in different media:



The high biocompatibility of the Co-Cr-Mo-C alloy is related to the spontaneous formation of an oxide film (passive layer) that protects the metal from the surrounding environment (body fluid). It is well known that the properties of this oxide film control the chemical resistance of the implant and therefore its durability into the human body. The properties of the passive film also control the corrosion behavior of the metal, the interaction with tissues and the electrolyte, and thus the degree of the material biocompatibility. The composition of the passive film of Co-Cr-Mo-C alloys is mainly Cr with a small amount of Co and Mo oxides [39, 67]. Some studies demonstrate the importance of alloying elements in the passive layer and their role in corrosion protection. The corrosion behavior of the passive alloy is determined by the presence of Cr although corrosion resistance of the passive layer is higher when Mo is present [9]. Mo does not react with the electrolyte since the passive film (composed by Cr and Co) protects the underlying Mo from further oxidation.

The main corrosion mechanism of Co-Cr-Mo-C alloys in the body fluids is a passive dissolution. Many studies have shown that metal ions dissolve from prostheses in the body because of the corrosion and wear debris cause allergies and implant failure [68, 69]. Investigations on the corrosion characteristics of Co-Cr-Mo alloy in different body solutions using potentiodynamic method have high corrosion resistivity and small passivity region for this alloy in joint fluid and body fluid simulated environments [25, 30, 70-72]. Table 1.6 shows the chemical composition of different solutions which were used for corrosion investigations.

S. Hiromoto et al. [25] considered the effect of forging ratio on corrosion behavior of Co-Cr-Mo-C alloy in different environment, they found that the alloy with a low forging ratio shows a reduced passive current density and also an increasing the grain boundaries by forging will decrease the corrosion resistant of alloy. F. Ren et al. [73] investigated the effect of physiological simulated solution on corrosion behavior of ultra-fine grain Co-28Cr-6Mo made by mechanical alloying process. Results demonstrate positive shift in corrosion potential and lower corrosion density as compared to conventional Co-Cr-Mo cast alloys. Petrov et al. [74] were studied the effect of surface treating such as solution heat treatment then water quenched (ST + WQ) and ultrasonic impact treatment (UIT), as a high plastic deformation process, on the corrosion behavior of Co-Cr-Mo-C alloy in Saline solution. The result shows worse corrosion behavior for ST+WQ sample in compare with the UIT-processed ones. The specimen exposed by UIT for 10s has the highest corrosion potential which is more positive than that for original specimen and ASTM requirements [38]. The study on influence of precipitate carbides on corrosion behavior of biomedical Co-Cr-Mo-C alloy shows that at high anodic potential ( $0.5-0.7 V_{\text{sat}} \text{ Ag/AgCl}$ )

metal dissolution occurs at the carbide boundaries and, in the form of etching-like dissolution, on the carbides. The effects of sintering temperature in powder metallurgical processing of Co-Cr-Mo alloy on its corrosion behavior have been investigated by Rodriguez et al. [75]. They selected 1150 °C, 1250 °C, and 1300°C for sintering process and the results of electrochemical test show less corrosion resistivity for samples sintered at 1150 °C. Corrosion behavior improves by increasing sintering temperature because of samples low density. Table 1.7 shows the result for corrosion of Co alloy samples processed by different methods.

*Table 1.6 - Chemical composition (g/L) of different solutions used for corrosion test*

<b>Solution</b>	<b>Chemical composition (g/L) in 1 liter distilled water</b>
Ringers [75]	NaCl (9.0), KCl (0.43), CaCl <sub>2</sub> (0.24), NaHCO <sub>3</sub> (0.2)
Hank [73]	NaCl (8.0), KCl (0.4), NaHCO <sub>3</sub> (0.35), NaH <sub>2</sub> PO <sub>4</sub> .2H <sub>2</sub> O (0.25), CaCl <sub>2</sub> .2H <sub>2</sub> O (0.19), MgCl <sub>2</sub> (0.19), MgSO <sub>4</sub> .7H <sub>2</sub> O (0.06), glucose (1.0)
Saline [25]	NaCl (8.0)

**Table 1.7 - Corrosion characteristics of Co-Cr-Mo alloys after different types of processing**

Sample	Process	Solution	$i_{\text{corr}}$ ( $\mu\text{A}/\text{cm}^2$ )	$E_{\text{corr}}^{(A)}$ (mV)	Reference
Co-29Cr-6Mo	Ultra Fine Grain	Hank	0.898	-265	[73]
Co-29Cr-6Mo-0.16C	ST + WQ <sup>(B)</sup>	Saline	0.316	-447	[74]
	UIT-30Sec		0.239	-351	
Co-29Cr-6Mo-0.35C	Sintered at 1150 °C	Ringer	NA	167	[75]
	Sintered at 1280 °C			287	
	Sintered at 1300 °C			302	
Co-28Cr-6Mo-0.25C	SA	Saline	5.27	-805	[24]
	SA+HIP+SA		1.3	-864	
	SA+PC+HIP+SA <sup>(C)</sup>		0.8	-762	
Co-29Cr-6Mo	HF <sup>(D)</sup> (50%)	Saline	0.008	-462	[25]
	HF (88%)		0.009	-331	

<sup>(A)</sup> All the numbers are converted from SCE to Ag/AgCl reference electrode

<sup>(B)</sup> ST: Solution treatment; WQ: Water quenched and UIT: ultrasonic impact treatment.

<sup>(C)</sup> SA: Solution Annealing; HIP: Hot Isostatic Pressing and PC: Porous Coating

<sup>(D)</sup> HF: Hot forging

## ***2. Materials and Methods***

## 2.1. Samples Preparation and Characterization

Cobalt alloy parts containing 28 wt. % Cr, 6 wt. % Mo, and 0.3 wt. % C (ASTM F-75 [38]) were purchased. Then, alloy was molten in an alumina crucible using a vacuum induction furnace. The system was evacuated three times with high purity argon prior to vacuum melting. When the parts turned into liquid at 2273 K (approx. 2000 °C); the chamber was immediately evacuated, and the melt was degassed. On the other hand, the temperature was dropped to 1873 K (approx. 1600 °C) and a slag was collected from top of the melt. Finally, the molten alloy was cast into a wedge-shaped sand and copper mold. The wedge mold sides were covered by an alumina sheet to keep the heat flow predominantly in one direction, (Figure 2.1). The same method of casting was used to prepare samples for tensile test in rectangular shape mold. Plates of 10 cm × 5 cm × 7 cm were cast in the copper mold and the developed phases were identified. A cooling rate of the order of 278 K/s was achieved at the time of casting. These plates were used for finding the effect of cooling rate on mechanical properties of Co-Cr-Mo-C alloy as well as isothermal heat treatment. Before casting, Pt/Pt-18% Rh thermocouples were centrally inserted into the wedge copper mold at 20, 60, and 90 mm locations from the tip to the top of the mold cavity, at half thickness locations of 1.0, 3.0, and 4.5 mm, respectively (Figure 2.1).

The as-cast ingots were then sectioned along the lateral direction in the plane normal to the tip of the wedge and polished followed by electrolyte etching using a 60 vol. % HNO<sub>3</sub> + 40 vol. % H<sub>2</sub>O solution at 6 V and 5 mA for 20 s. Prepared samples were studied by means of optical microscopy and scanning electron microscopy (SEM). SEM and EDX analysis of specimens were performed using a Topcon SM300 Scanning Electron Microscope at 20KV of intensity.

The phases presented in these samples were determined by x-ray diffraction using Bruker D8 Discover. The source of X-Ray was Cu  $K_{\alpha}$  with 40 kV primary beam. The angle of analysis ( $2\theta$ ) set to be between  $20^{\circ}$  to  $100^{\circ}$  and all tests were performed at room temperature on smooth finished specimens.

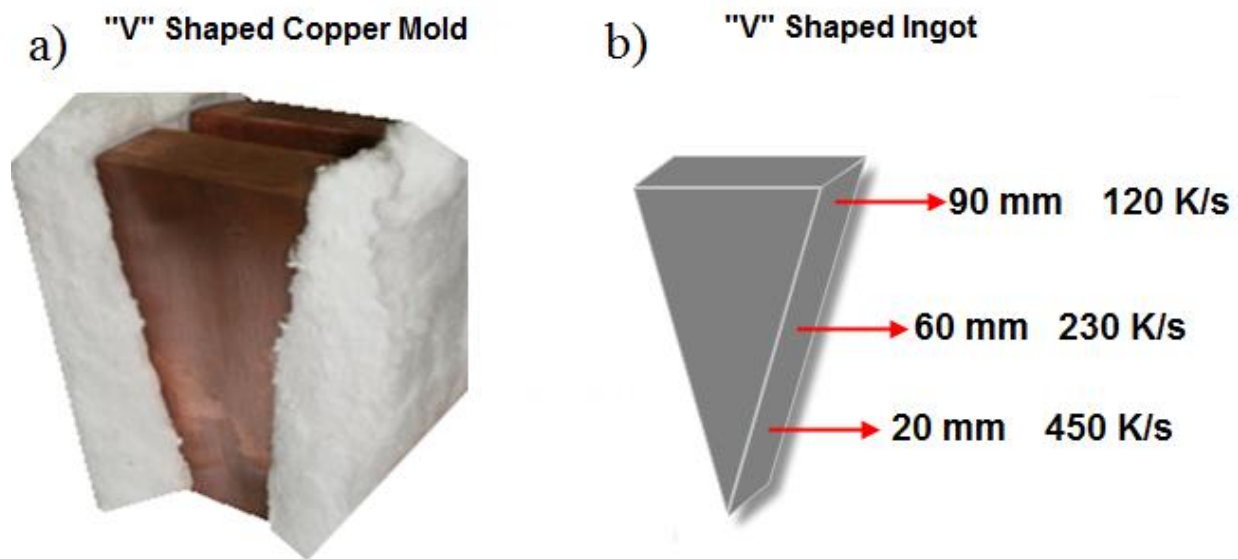


*Figure 2.1 - (a) Wedge-shaped copper mold isolated in both sides by an alumina sheet; (b) "V" shaped ingot showing three different cooling rate zones: 90 mm high: 120 K/s, 60 mm high: 230 K/s, and 20 mm high: 450 K/s.*

## 2.2. Laser modification

Investment casting used to cast the molten metal at 1773 K in to preheated molds. The chemical composition of alloy measured, and it is reported in Table 2.1. Cylindrical plates were cut using waterjet equipment with dimensions of 39.2 mm and 7.0 mm in diameter and thickness, respectively. The Laser Surface Modifying (LSM) process was applied on samples using a

Nd:YAG pulsed laser model HTS LS P-160 with a 1067 nm wavelength. In order to avoid metal oxidation due to high temperature of process, the laser melt pool was protected by argon gas with a flow of 1.5 L/min. Also, 50% overlapping melt track were formed on discs used for corrosion test. The laser beam mode was Gaussian shape and the optical set-up made a laser beam spot diameter of  $0.8\pm 0.05$  mm on the work piece. The pulse frequency for all the tests was fixed at  $8\text{ s}^{-1}$ .

### **2.3. Heat treatment**

The thermal cycle identified as an ageing heat treatment was carried out inside a high temperature induction furnace provided with room atmosphere. Sets of , 5 mm thick samples were heated to 1150 °C at 50 °C/min and soaked for 1 hour at 1150 °C and then rapidly quenched in water at room temperature. Following this high-temperature heat treatment and quenching, the samples were placed again inside the furnace on a ceramic rack. The rack was designed to facilitate the individual extraction and quenching of the samples after predetermined periods (3 to 25 hours) of isothermal aging at temperatures of 750 °C, 800 °C, 850 °C, and 900 °C. The changes in structure caused by this type of thermal treatment were followed as a function of aging time by measuring X-ray diffraction patterns on the aged samples at room temperature.

## 2.4. Corrosion test

The surface of as-cast (rapidly solidified) alloy and laser welded alloy were finished by 1200 SiC abrasive paper and polished by Al<sub>2</sub>O<sub>3</sub> 1 μm solution for corrosion tests. The disks were coated by epoxy resin and leaving the desired area for measurement uncoated. Biological Ringer's solution consists of 9 g NaCl, 0.43 g KCl, 0.24 g CaCl<sub>2</sub>, and 0.2 g NaHCO<sub>3</sub> in 1 liter of distilled water was used as an electrolyte. Super saturated Ag/AgCl and Pt plate were used as reference electrode and counter, respectively. The sample was fixed in an electrode holder with O-ring. To stabilize the potential, samples immersed in the solution for about 15 min. The stabilized potential was used as the open-circuit potential ( $E_{ocp}$ ) of samples. Samples were polarized in a range of -0.3 V to +1.3 V versus  $E_{corr}$  with the scanning rate of 10 mV min<sup>-1</sup>. In order to measure the corrosion rate, a Biologic SP-200 and EC-Lab v10.33 corrosion software were used for electrochemical control and data analysis, respectively. The test was repeated three times for each sample to have reliable results. The corrosion current density ( $i_{corr}$ ) and other corrosion parameters including anodic and cathodic Tafel slopes ( $b_a$  and  $-b_c$ ), were measured by considering the polarization curves by Tafel extrapolation.

*Table 2.1 - Chemical composition (wt%) of as-cast Co-Cr-Mo-C sample*

Element	C	S	Mn	Si	P	Cr	Ni	Mo	W	Fe	Co
Cast sample	0.25	0.003	0.21	0.61	0.0014	28.0	0.43	5.82	0.02	0.38	Bal

### ***3. Results and discussion***

### 3.1. Microstructure characterization

The microstructure of the as-cast Co–Cr–Mo–C alloy consists of a cobalt-rich matrix with a dendritic structure and a relatively large volume fraction of interdendritic precipitates. During the solidifying stage, some amount of the metastable phase was retained at the room temperature when the Co–Cr–Mo–C alloy solidified through the FCC phase field. A cobalt-rich matrix was found with residual phase and phase coupled with intergranular striations. The interdendritic precipitates are identified as carbides that also exist continuously at the grain boundaries. This brittle phase corresponded to the higher solute content (Cr, Mo) at the grain boundaries causing a stress concentration and leading to early fracture. The intergranular striations are related to  $\epsilon$ -martensite phase formed because of stacking faults. Cr and Mo solutes can diffuse preferentially at the stacking faults with increasing temperature.

The maximum cooling rate experimentally measured was: 450 K/s at distance 20 mm from the tip of the “V” shape ingot; 300 K/s at 60 mm at the center of the ingot; 120 K/s at 90 mm at the top of the ingot; and conventional cooling rate from sand cast samples of approximately 10 K/s. In the Co–Cr–Mo–C alloy, there are three dominant microstructures: 1) dendrites (columnar or equiaxed), 2) dendrites (columnar or equiaxed) and eutectic in the interdendritic regions and, 3) dendrites (columnar or equiaxed) and eutectic plus the intermetallic phase  $\sigma$  in interdendritic regions.

Figures 3.1-3.4 show the various microstructures regarding the cooling rate found in the studied locations (at 20 mm, 60 mm and 90 mm from bottom to top in the rapid solidified wedge ingot

and top of the sand mold). It can be clearly observed that the dominant microstructure is the columnar dendrites. In addition, the  $\sigma$  phase which is characterized as extremely fragile appears in this investigation which conforms to the alloy F75 casting condition. In contrast, in alloys with no carbon content,  $\sigma$  phase was only found in alloys with more than 35% Cr content. While in the F75 alloy,  $\sigma$  phase always precipitates despite having a chromium percentage of 28% by weight [27].

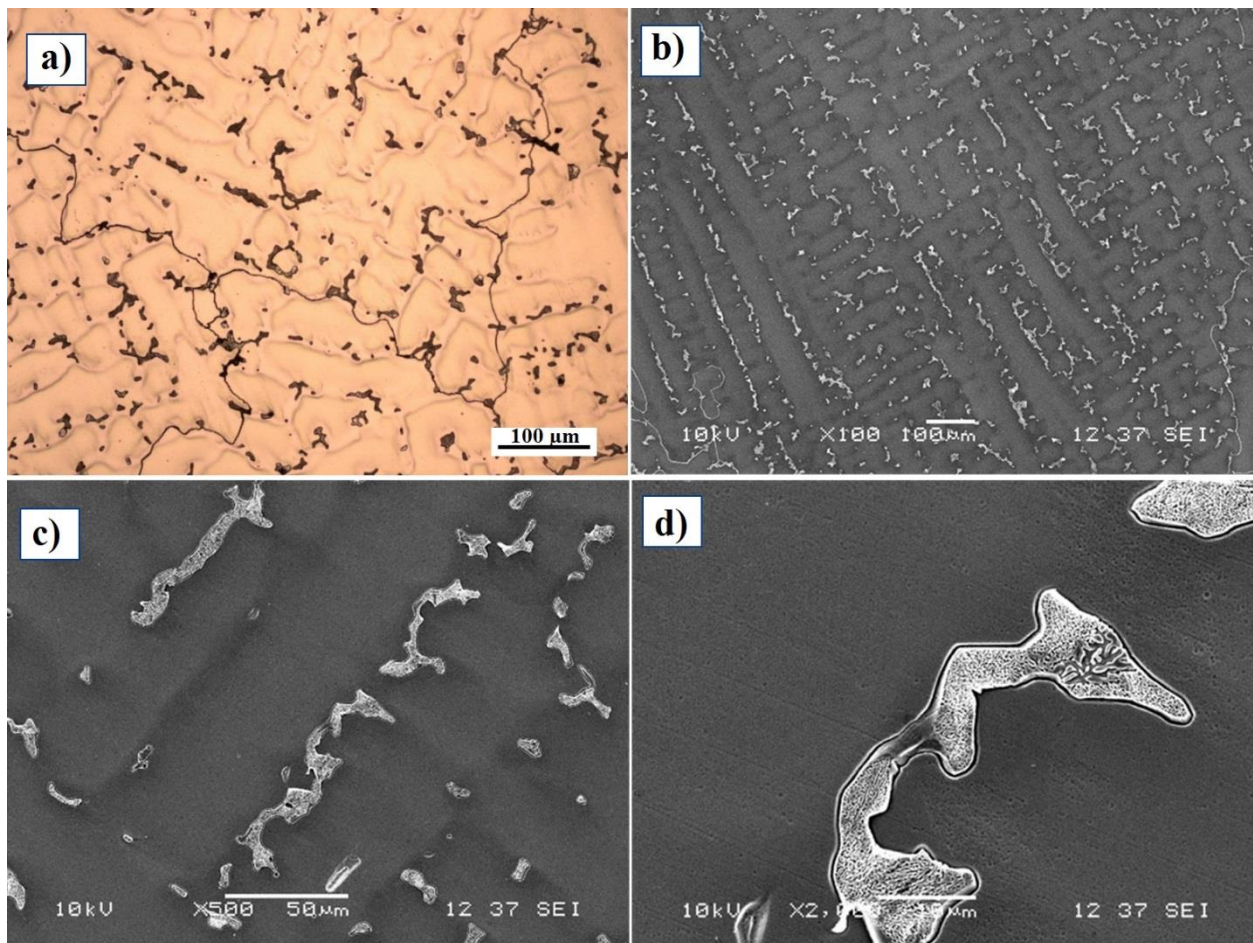


**Figure 3.1**– Images of Co-Cr-Mo-C alloy regarding its distance from the tip of the “V” shape mold- Sand cast-90 mm (cooling rate: 10 K/s), a) optical image 200x and SEM images b) 100x, c) 500x, and d)2000x.

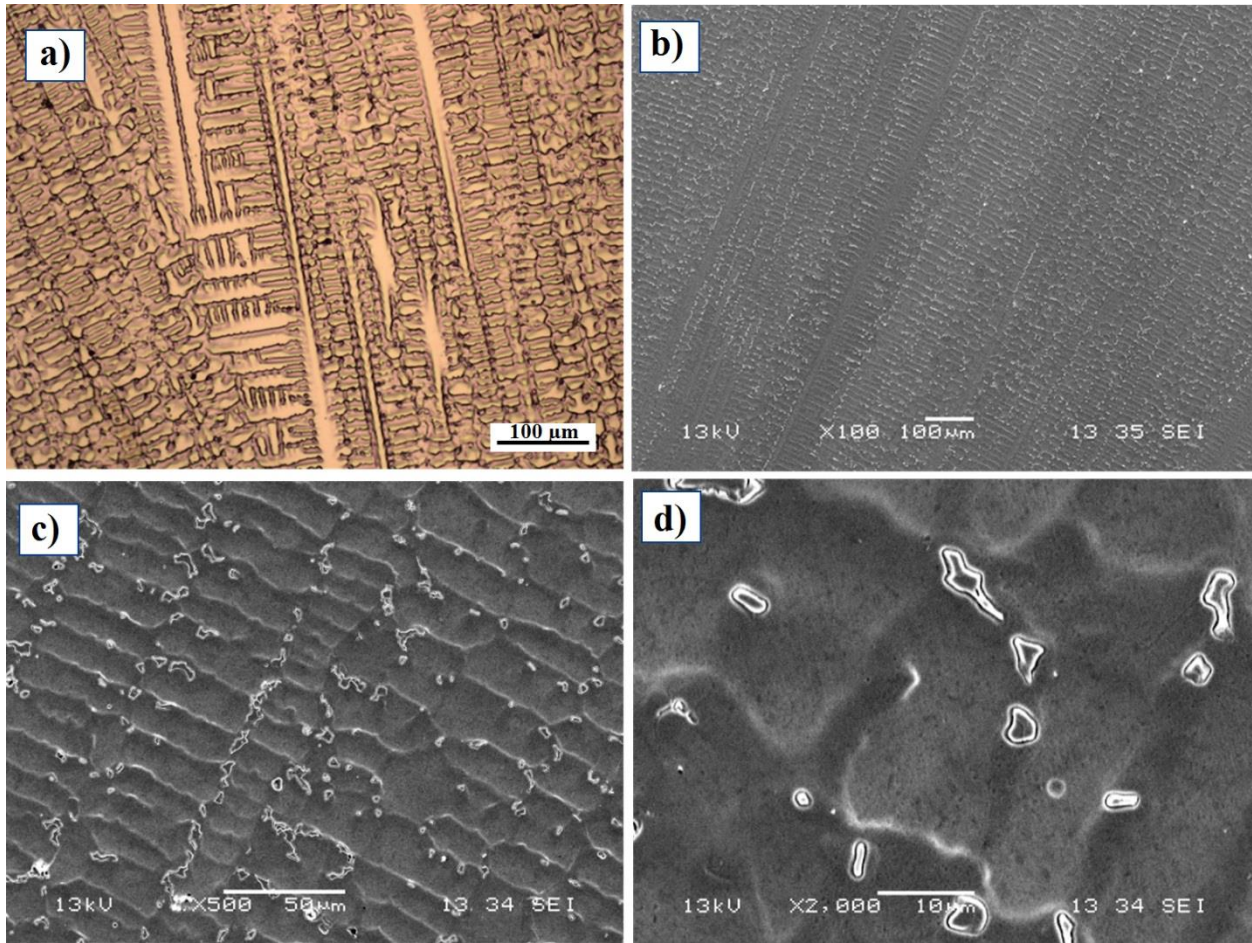


*Figure 3.2 – Images of Co-Cr-Mo-C alloy regarding its distance from the tip of the “V” shape mold- Copper mold cast-90 mm (cooling rate: 120 K/s), a) optical image 200x and SEM images b) 100x, c) 500x, and d)2000x.*

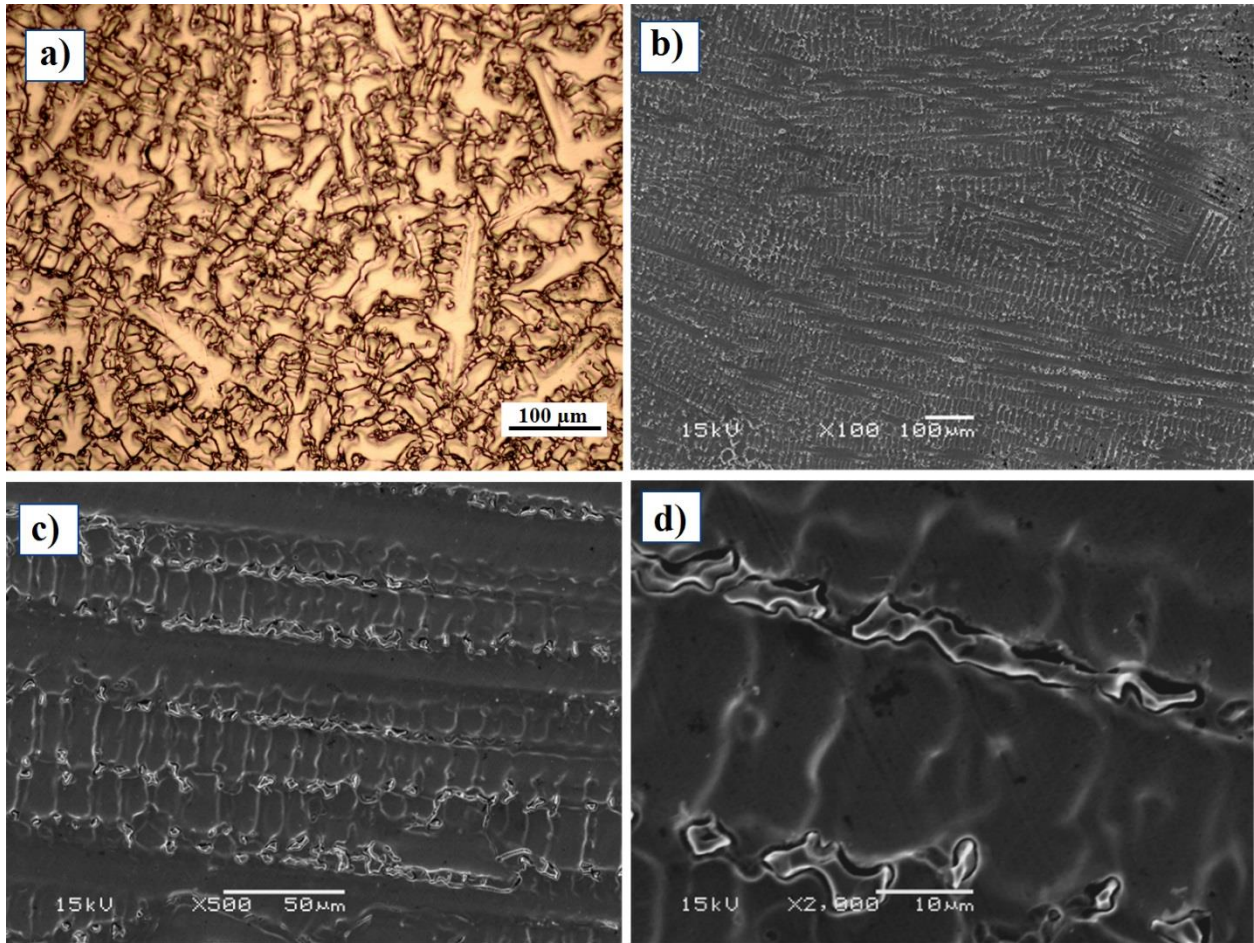


*Figure 3.3 – Images of Co-Cr-Mo-C alloy regarding its distance from the tip of the “V” shape mold- Copper mold cast-60 mm (cooling rate: 230 K/s), a) optical image 200x and SEM images b) 100x, c) 500x, and d)2000x.*

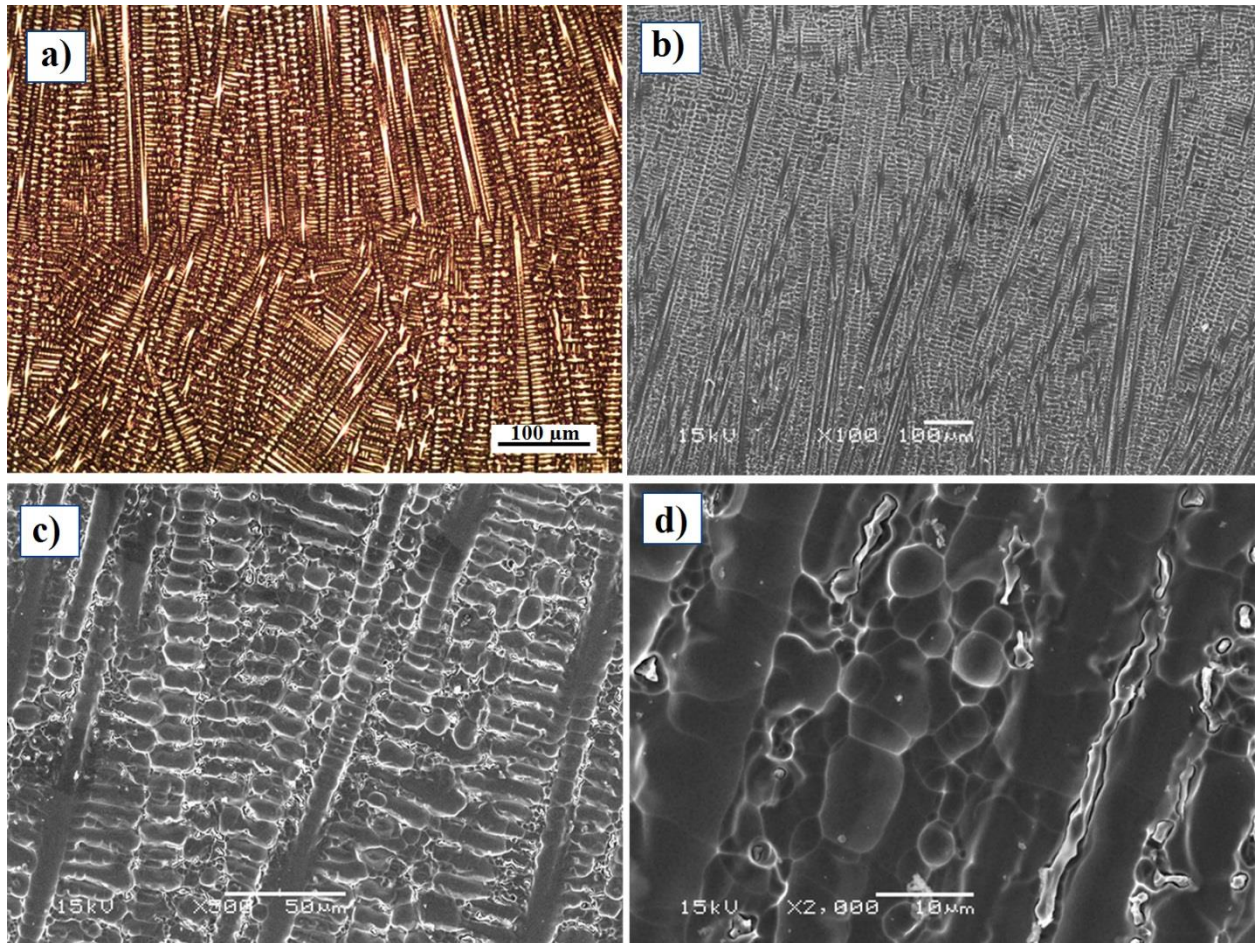


**Figure 3.4 – Images of Co-Cr-Mo-C alloy regarding its distance from the tip of the “V” shape mold- Copper mold cast-20 mm (cooling rate: 450 K/s), a) optical image 200x and SEM images b) 100x, c) 500x, and d)2000x.**

Using SEM, dendrite arm spacing (DAS), secondary dendrite arm spacing (SDAS), and carbide size were determined and reported on Figure 3.5 as well as Table 3.1 along with hardness of the samples regarding their cooling rate. It is very important to note the secondary dendrite arm spacing (SDAS) for evaluating microstructure of this alloy. In several studies SDAS is reported in the order of 5 to 18  $\mu\text{m}$  [27, 49]. In this research work, SDAS lower than 5  $\mu\text{m}$  were obtained

in the bulk microstructure. In addition, precipitates are randomly distributed in the primary and secondary arms of the matrix, which were identified with scanning electron microscopy. As it is shown in figure 3.5, increasing the cooling rate will decrease the DAS, SDAS, and carbide size while increasing the hardness; however, the carbide percentage alteration in rapidly solidified samples prepared by using copper mold is not significant. Hardness measurement was performed on samples using Hardness Rockwell C and the average of five measurements is reported.

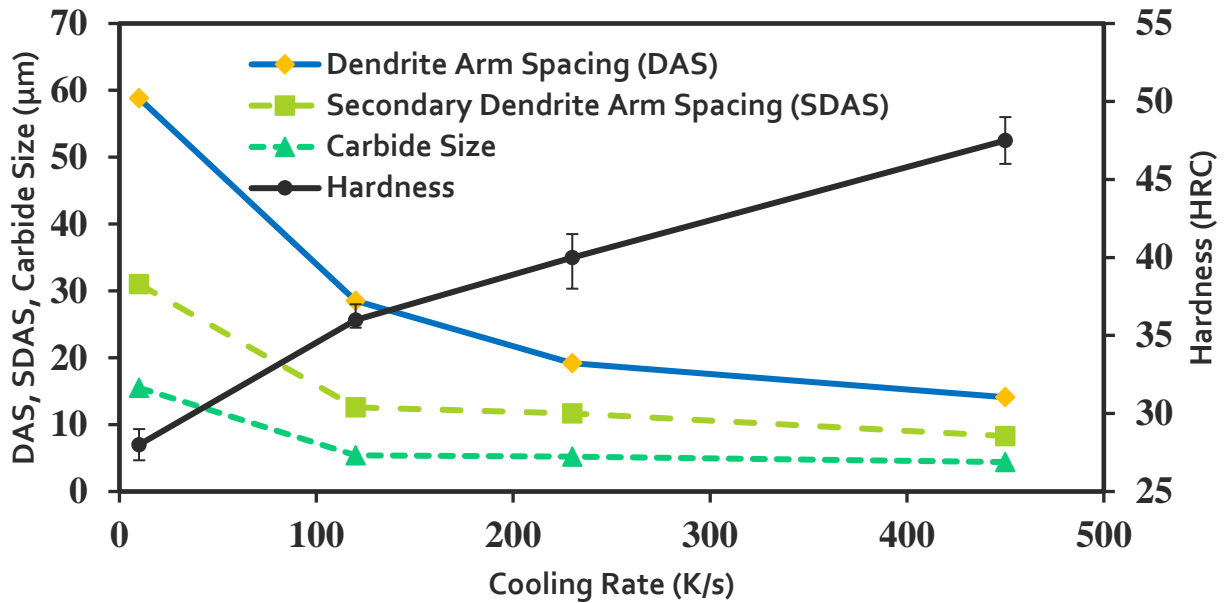


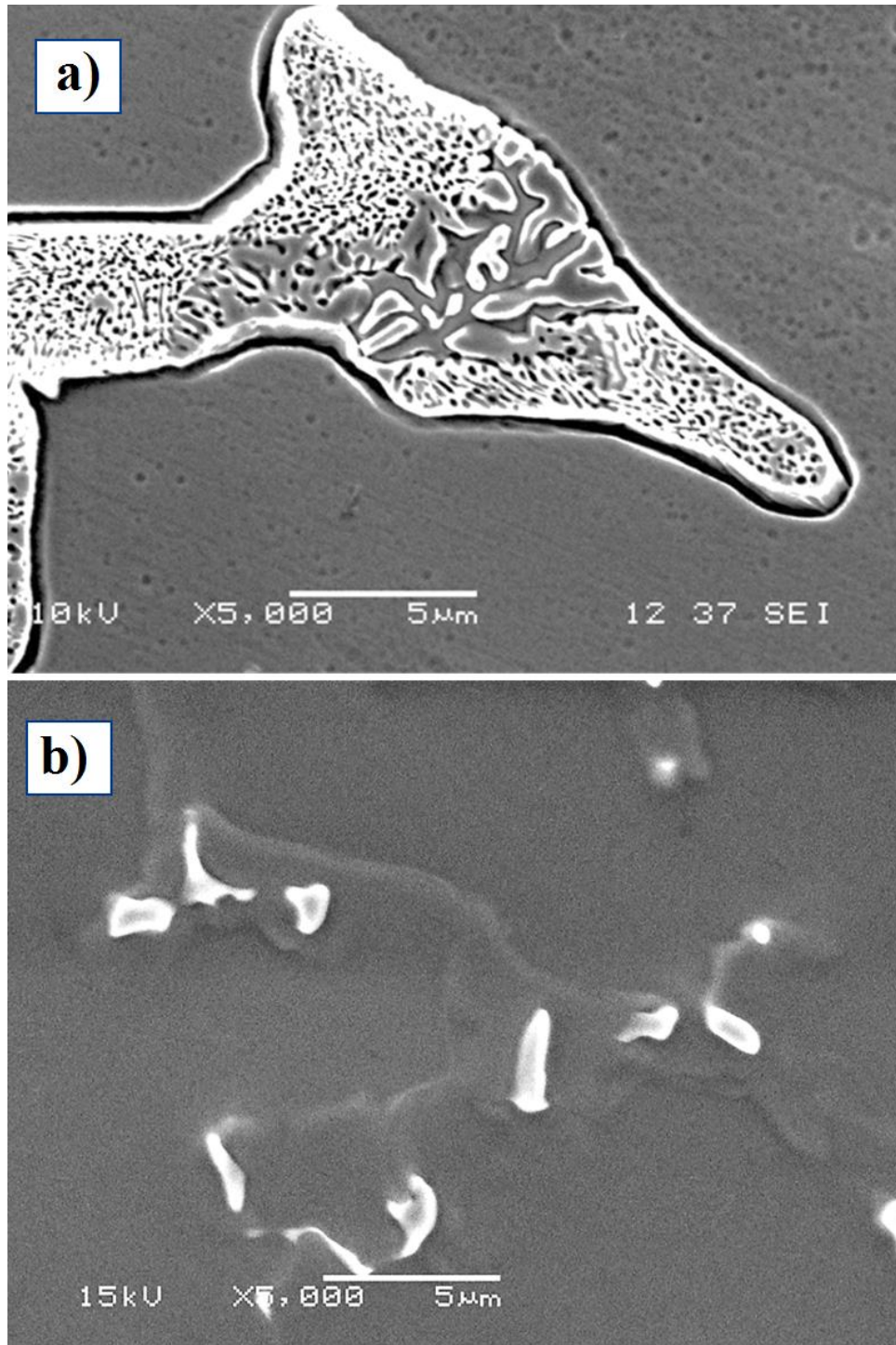
Figure 3.5 - Microstructure analyzing of Co-Cr-Mo-C alloy regarding their cooling rates.

Table 3.1 - Microstructure analyzing of Co-Cr-Mo-C alloy in different positions

Mold/Distance from tip	DAS (μm)/St.D	SDAS (μm)/St. D	Carbide size (μm)/St. D	Hardness (HRC)
Sand/ 9cm	58.82/3.23	31.05/2.94	15.52/7.30	28
Cu/9cm	28.46/0.60	12.60/0.94	5.39/3.79	36
Cu/6cm	19.21/0.73	11.74/0.67	5.17/4.11	40
Cu/2cm	14.13/1.14	8.31/0.23	4.42/3.6	47.5

Microstructural analysis of the Co alloy revealed the presence of blocky and lamellar (dendritic) shape carbides in this alloy (Figure 3.6), depending on its cooling rate. Physical and chemical factors have a great influence on the carbide formation: the main alloying elements are responsible for their composition and structure, and the cooling rate largely affects their size and shapes. According to Tylor and Waterhouse [45] these carbides are most likely to be  $M_{23}C_6$  and  $M_6C$ . Cr has a predominant role in the formation of the carbide type  $M_{23}C_6$  (where  $M = Co, Cr, Mo$ ), but also Mo, when present in large quantities, can promote carbide precipitation in the form of  $M_6C$ .

Figure 3.6 shows two types of carbides formed in Co-Cr-Mo-C alloy due to its cooling rate. It is found that in low cooling rate solidification, carbides are larger and dendritic shape while in high cooling rate solidification carbides are blocky shape and finer in comparison with those at low cooling rate. Figures 3.7-3.10 show the EDS analysis results on the carbide and matrix of the alloy regarding their cooling rate. It can be understood from the EDS results that the area without carbide mainly consist of Co and Cr (Figure 3.7a). The EDS analysis shows that at low cooling rates the major alloying element is Mo (Figure 3.7b), while Cr is the predominant alloying element at high cooling rates and represent blocky shaped carbides (Figure 3.10b).



*Figure 3.6 – Showing carbide morphology in Co-Cr-Mo-C alloy regarding its cooling rate, a) 10 K/s cast in sand mold 90 mm from the tip of “V” shaped mold, and b) 450 K/s cast in copper mold 20 mm from the tip of “V” shaped mold.*

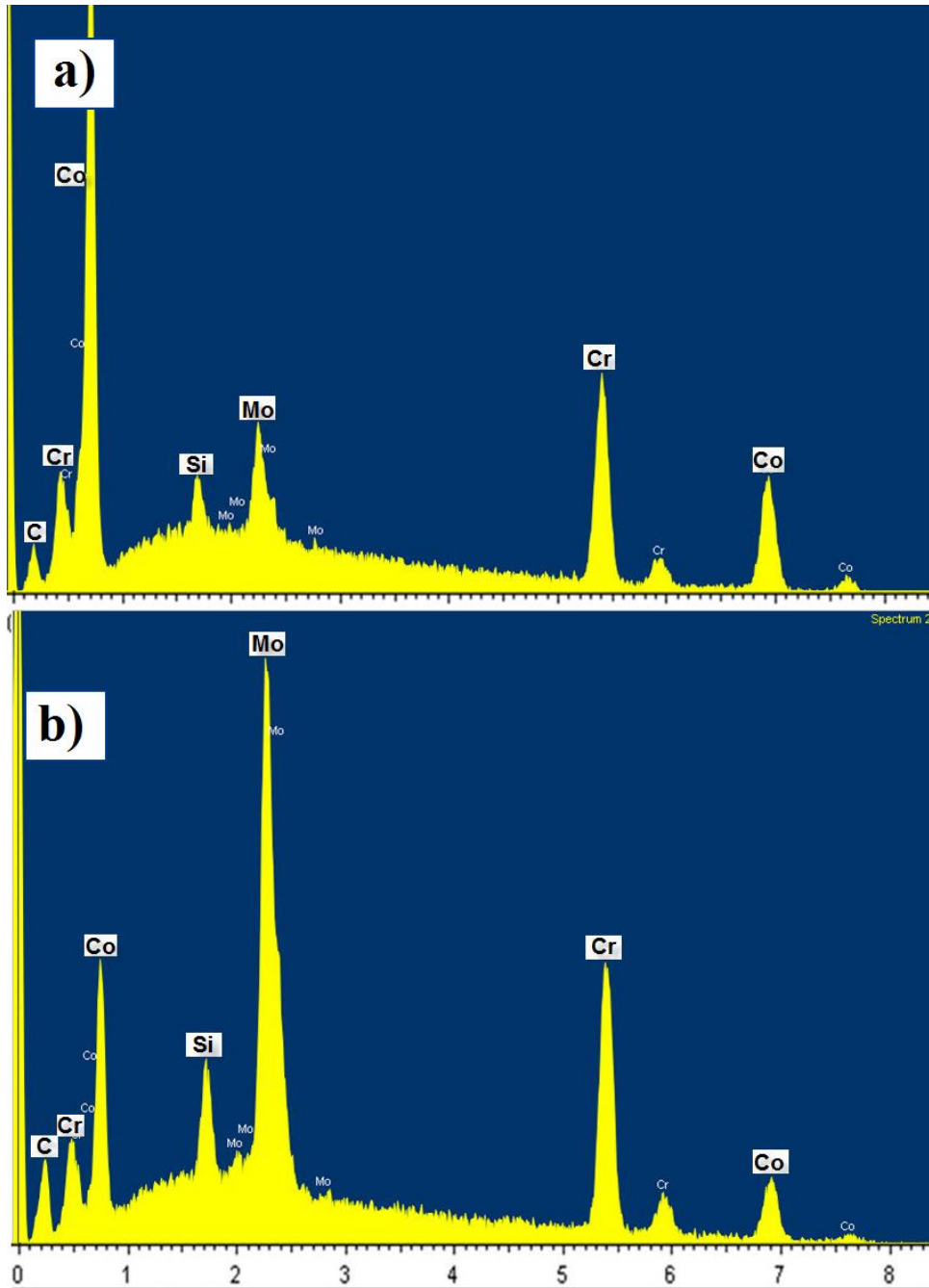


*Figure 3.7 - Shows the EDS analysis results on the a) matrix and b) carbide of the sand cast alloy 90mm from the tip of the “V” shaped mold.*

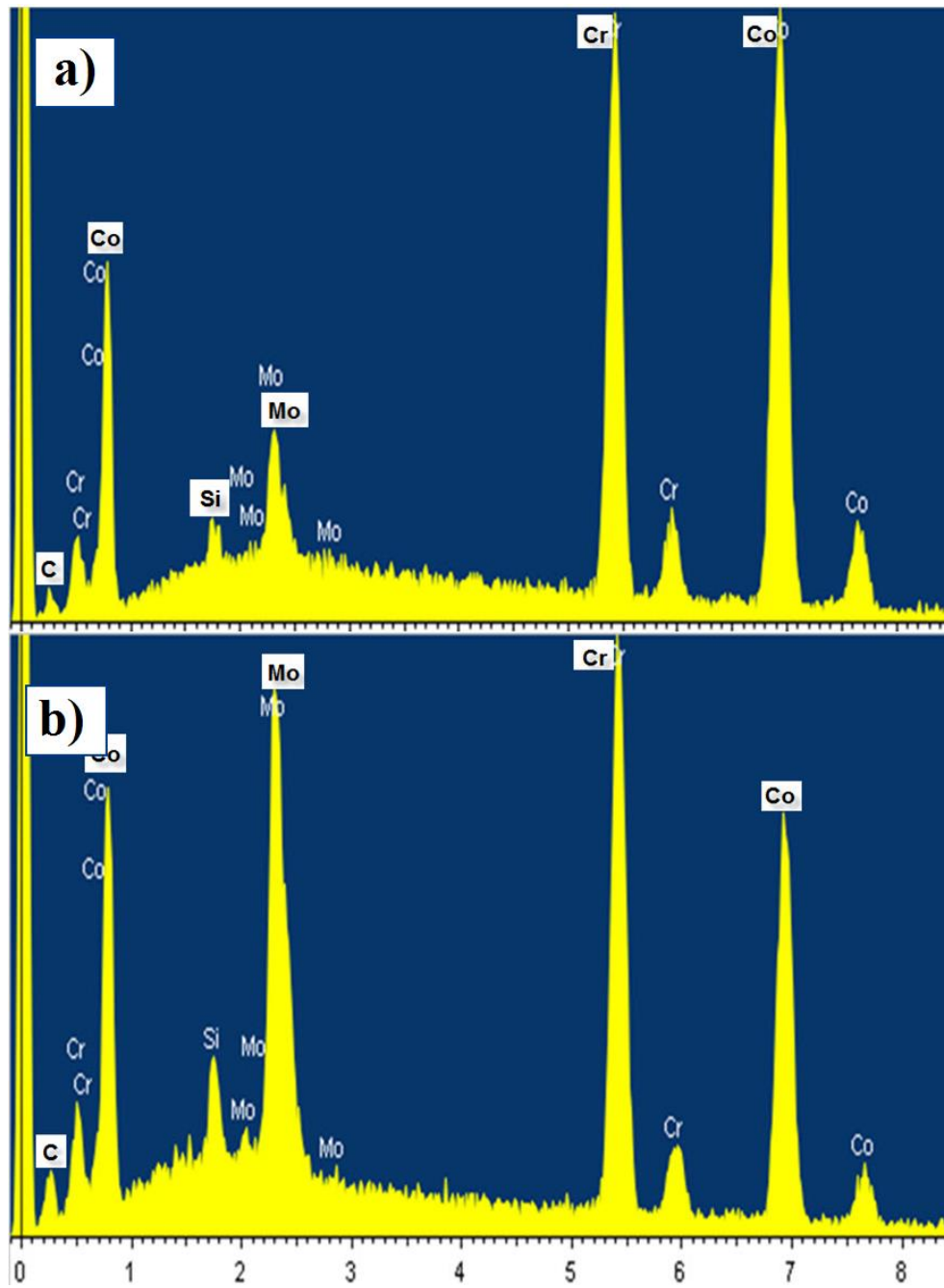


*Figure 3.8 - Shows the EDS analysis results on the a) matrix and b) carbide of the copper mold cast alloy 90mm from the tip of the “V” shaped mold.*

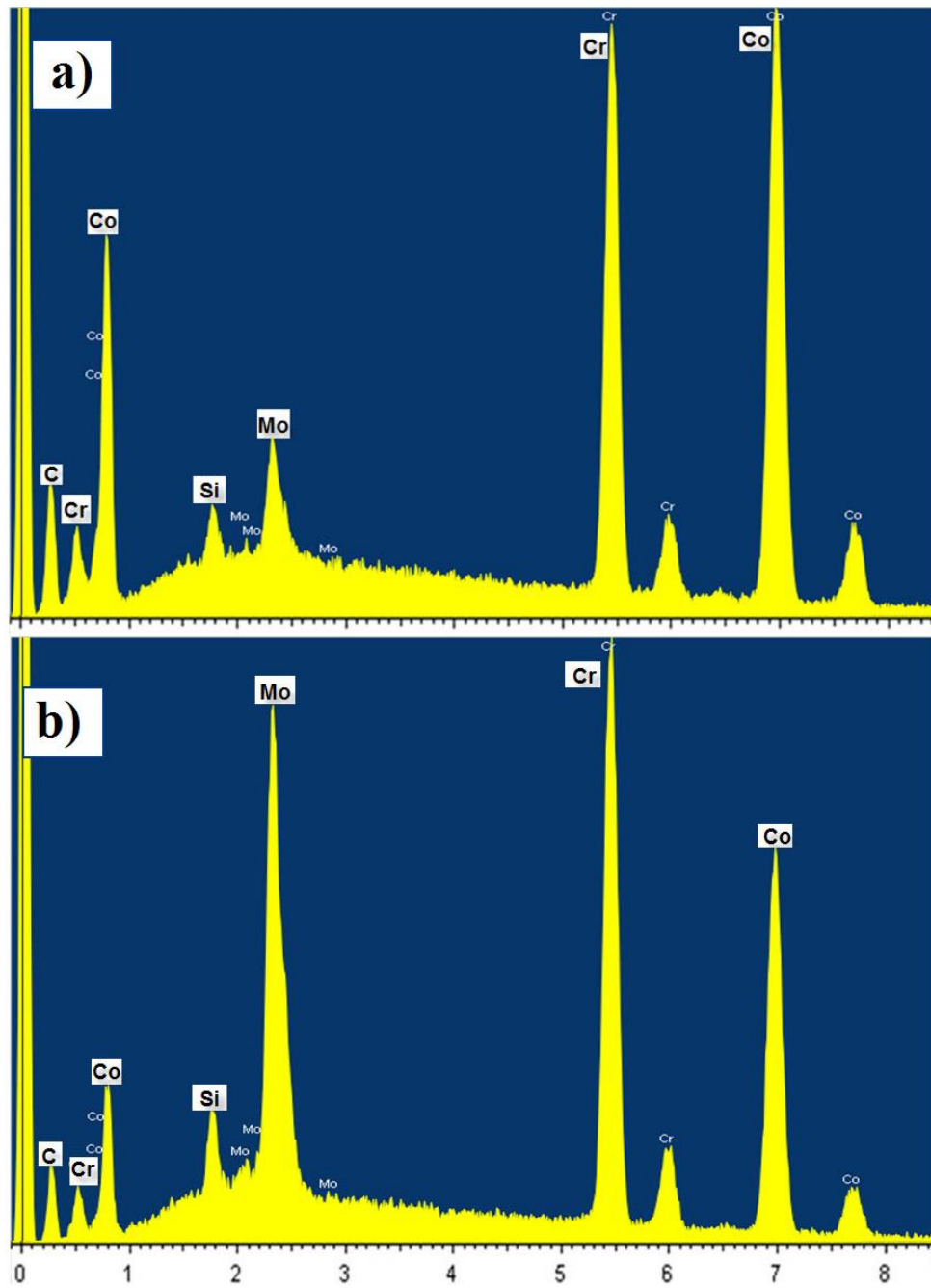


*Figure 3.9 - Shows the EDS analysis results on the a) matrix and b) carbide of the copper mold cast alloy 60mm from the tip of the “V” shaped mold.*

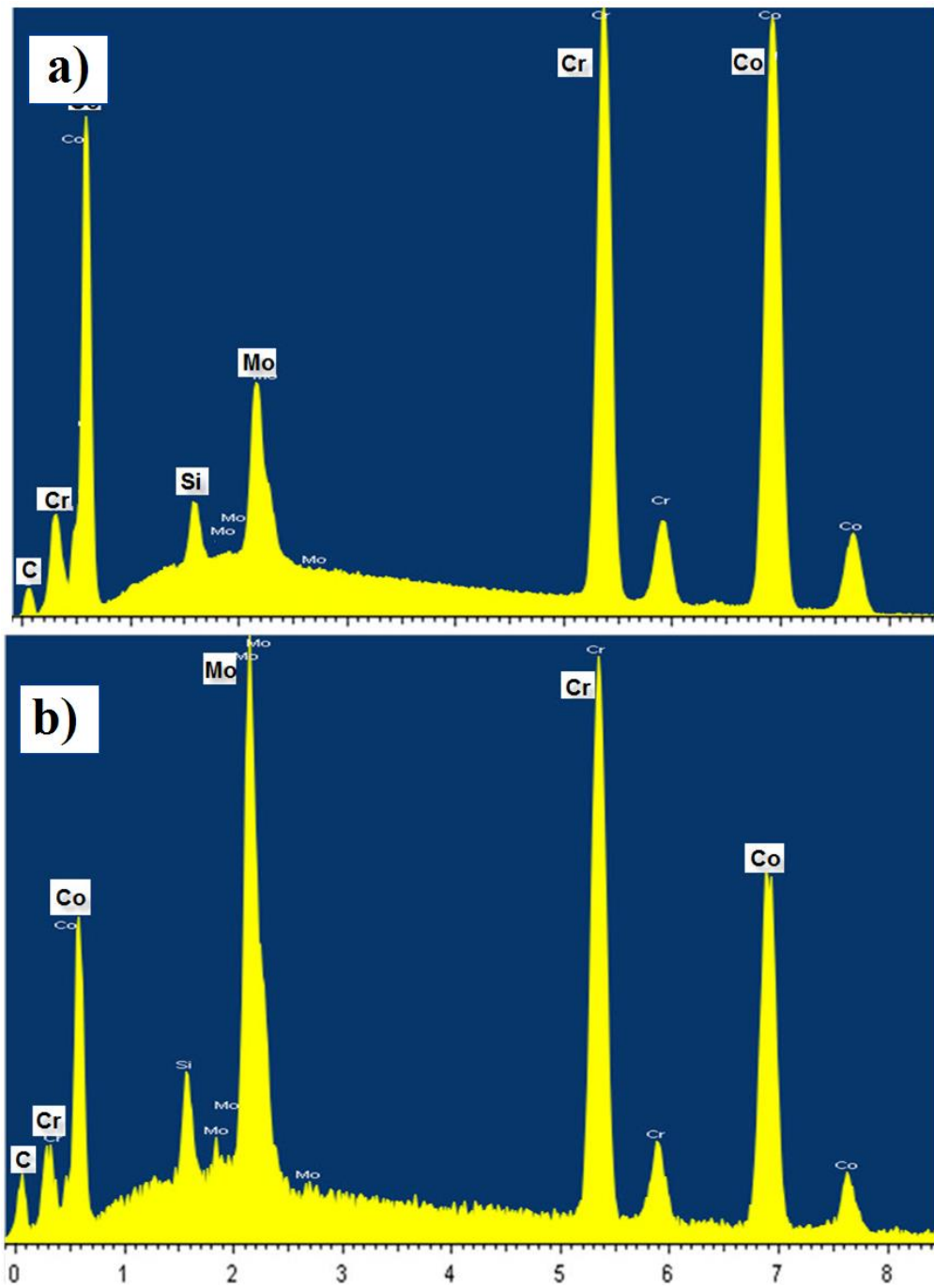


*Figure 3.10 - Shows the EDS analysis results on the a) matrix and b) carbide of the copper mold cast alloy 20mm from the tip of the “V” shaped mold.*

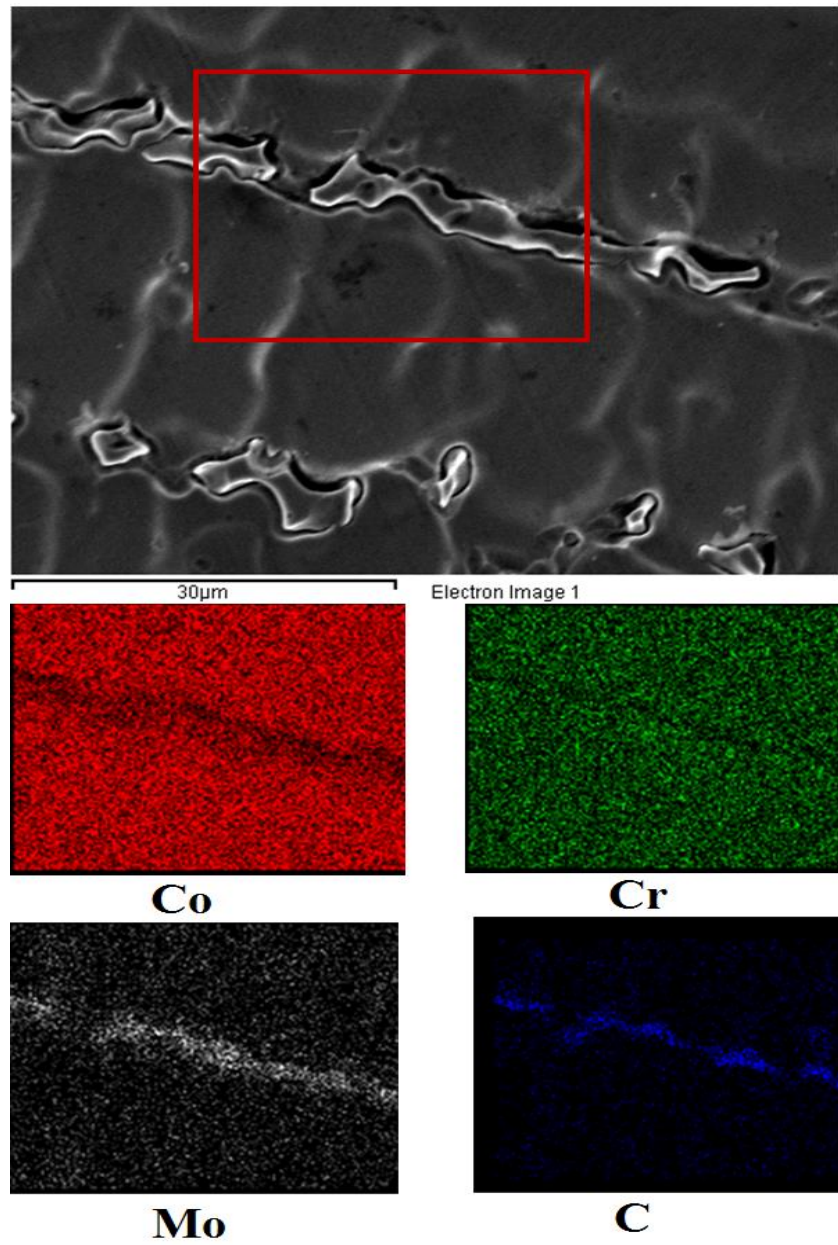


*Figure 3.11 - Shows the EDS results of Co-Cr-Mo-C alloy in presence of carbide.*

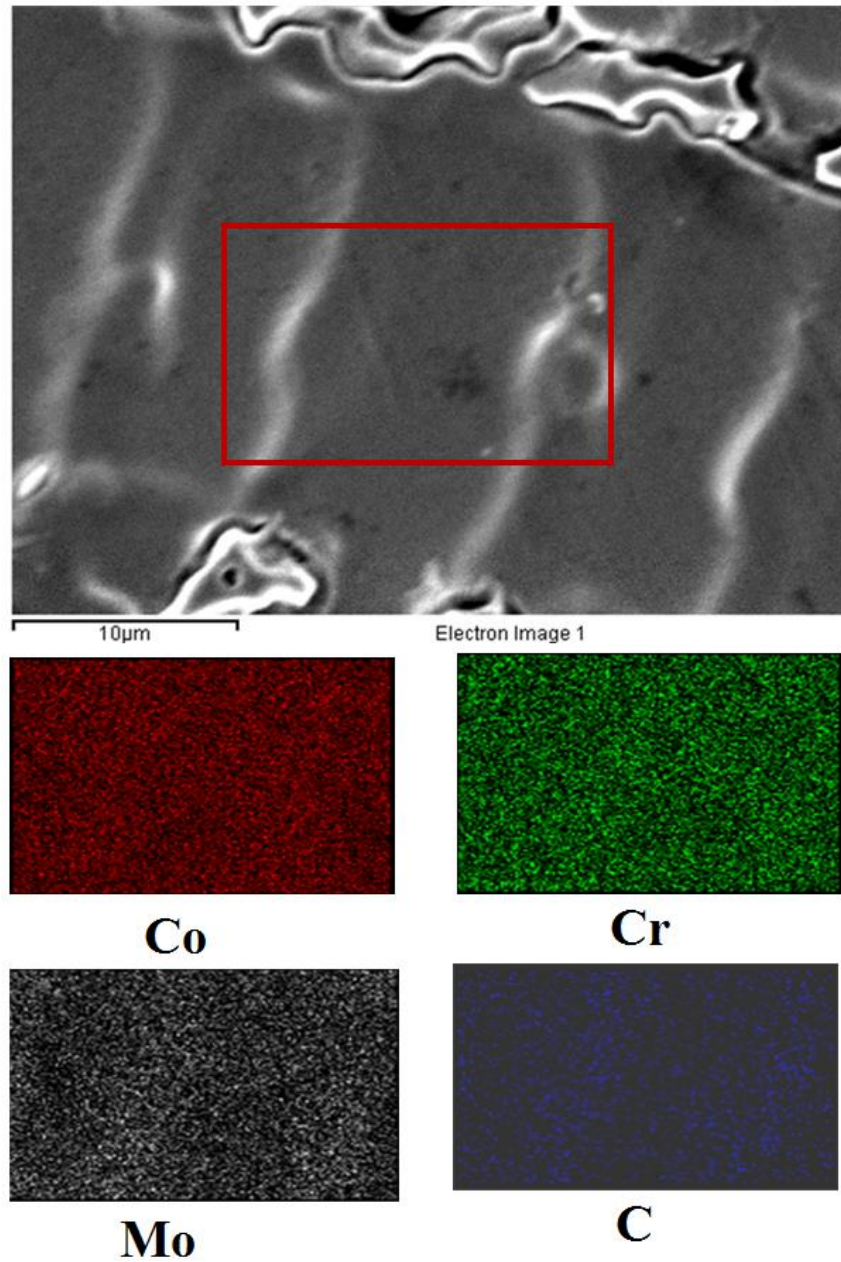


*Figure 3.12 - Shows the EDS results of Co-Cr-Mo-C alloy in presence of carbide.*

From EDS analysis (Figures 3.11 and 3.12), it was found that rapid solidification either reduces or eliminates segregation. Despite the columnar dendritic structure, which is expected to become

heavily segregated at the interdendritic locations, EDS results of interdendritic regions shows no evidence of segregation, Figure 3.12. A reduction in the primary dendrite arm spacing was observed (see Figure 3.5). It is obvious in Figure 3.11 that Mo is dominant in carbides at the interdendritic regions in compare with the matrix of the alloy.

### **3.1.1. Mathematical model of directional solidification under conditions of forced solidification (rapid solidification)**

In order to understand the effects of rapid solidification on Co-Cr-Mo-C alloy, a mathematical model of directional solidification under rapid solidification conditions was considered. Using this model, a direct relation of the columnar dendrite tip radius and the concentration of solute (Cr in this case) can be obtained regarding to the velocity of the solidification front. In this way, a theoretical prediction of the solidification velocity is necessary to reduce or eliminate the interdendritic segregation in the proposed alloy. In 1986 Kurz, Giovanola and Trivedi [76] proposed a mathematical model to describe the directional growth of columnar dendrites under conditions of forced solidification (rapid solidification). Langer and Müller-Krumbhaar [77] demonstrated that the tip of a dendrite grows closer to a marginally stable state. Therefore, the following approximation can be written:

$$R = \lambda_s$$

*Equation 3.1*

Where  $R$  is the radius of the tip of the dendrite growing in steady state and  $\lambda_s$  is the critical wavelength of the solid-liquid interface at the stability limit. Subsequently, Müllins and Sekerka [78], concluded that the marginally stable wavelength in a plane front can be given by:

$$\omega^2 \Gamma = m_l G_c \xi_c - G \quad \text{Equation 3.2}$$

$$\text{With } \omega = 2\pi / \lambda_s \quad \text{Equation 3.3}$$

$$\xi_c = 1 - \frac{2k}{\{1 + [4\pi D / (\lambda_s V)]^2\}^{1/2} - 1 + 2k} \quad \text{Equation 3.4}$$

Where  $\Gamma$  is the Gibbs-Thompson parameter, defined as the ratio of the solid-liquid interface energy specific to the fusion entropy,  $m_l$  is the liquid slope,  $G_c$  is the concentration gradient of the liquid at the interface,  $G$  is the average temperature gradient at the interface,  $k$  is the partition coefficient,  $D$  is the diffusion coefficient and  $V$  is the interphase velocity, Table 3.2.

*Table 3.2 - Properties for Co-28Cr-6Mo-0.25C*

Property	Value (Unit)	Reference
$D$	$7.74 \times 10^{-3}$ (mm/s)	[79]
$K$	0.58	Figure 1.5
$\Gamma$	$2.7 \times 10^{-4}$ (K.mm)	[80]
$m_l$	-3.14 (K/wt%)	Figure 1.5

Using Eq. 3.1, and defining the number of solute Peclet (the ratio of a characteristic dimension,  $R$ , of the system to the boundary layer of solute in the planar interface) as  $P_c = RV/2D$ , we obtain:

$$\frac{2k}{\left[1 + \left(\frac{2\pi}{P_c}\right)^2\right]^{1/2} - 1 + 2k} \quad \text{Equation 3.5}$$

of the Eq. 3.2 :  $\omega = \left\{\frac{mG_c\xi_c - G}{\Gamma}\right\}^{1/2}$ , substituting in  $\lambda_s = \frac{2\pi}{\omega}$ , we have:

$$\lambda_s = \frac{2\pi}{\left\{\frac{mG_c\xi_c - G}{\Gamma}\right\}^{1/2}} \quad \text{Equation 3.6}$$

$$\lambda_s = \frac{2\pi\Gamma^{1/2}}{\{mG_c\xi_c - G\}^{1/2}} \quad \text{Equation 3.7}$$

$$R = 2\pi \left[\frac{\Gamma}{mG_c\xi_c - G}\right]^{1/2} \quad \text{Equation 3.8}$$

With high solute Peclet numbers ( $P_c > \pi^2/\sqrt{k}$ ), Eq. 3.4 is reduced to:

$$\xi_c = \frac{\pi^2}{kP_c^2} \quad \text{Equation 3.9}$$

and, substituting this limit value in Eq. 3.2 with  $\mathbf{G} = \mathbf{0}$ , we have the condition of absolute stability. In order to solve the Eq. 3.22,  $\mathbf{G}_c$  and  $\mathbf{G}$  must be known. From Eq. 3.9, the concentration gradient,  $\mathbf{G}_c$ , in front of the dendrite advance can be found from a flow balance [81]. In this way:

$$\mathbf{G}_c = \frac{-V\mathbf{C}_L^*p}{D} \quad \text{Equation 3.10}$$

with  $(1 - \kappa) \mathbf{C}_L^* = \frac{C_0}{1 - (1 - \kappa)I\nu(P_c)}$  or,  $\frac{C_L^*}{C_0} = \mathbf{A}(P_c)$ , where  $\mathbf{A}(P_c) = [1 - (1 - \kappa)I\nu(P_c)]^{-1}$

where  $C_0$  is the initial composition of the liquid. Thus, the concentration gradient at the tip of the dendrite can be obtained in the following way:

$$\mathbf{G}_c = \frac{-V(1 - \kappa)C_0\mathbf{A}(P_c)}{D} \quad \text{Equation 3.11}$$

$$\mathbf{G}_c = \frac{-V(1 - \kappa)C_0}{D[1 - (1 - \kappa)I\nu(P_c)]} \quad \text{Equation 3.12}$$

Substituting the previous expression in the Eq. 3.8:

$$\mathbf{R} = \frac{2\pi\Gamma^{1/2}}{\left\{m\left(\frac{-V(1 - \kappa)C_0}{D[1 - (1 - \kappa)I\nu(P_c)]}\right)\xi_c - \mathbf{G}\right\}^2} \quad \text{Equation 3.13}$$

But considering  $\mathbf{R} = \frac{2P_cD}{V}$ , we have:

$$\frac{2P_c D}{V} = \frac{2\pi\Gamma^{1/2}}{\left(\frac{-mV(1-\kappa)C_0}{D[1-(1-\kappa)I\nu(P_c)]}\xi_c - G\right)^{1/2}} \quad \text{Equation 3.14}$$

$$\frac{P_c D}{V} = \frac{\pi\Gamma^{1/2}}{\left(\frac{-mV(1-\kappa)C_0\xi_c}{D[1-(1-\kappa)I\nu(P_c)]} - G\right)^{1/2}} \quad \text{Equation 3.15}$$

$$\left\{\left(\frac{-mV(1-\kappa)C_0\xi_c}{D[1-(1-\kappa)I\nu(P_c)]} - G\right)^{1/2} P_c D\right\}^2 = \{\pi\Gamma^{1/2}V\}^2 \quad \text{Equation 3.16}$$

$$\left(\frac{-mV(1-\kappa)C_0\xi_c}{D[1-(1-\kappa)I\nu(P_c)]} - G\right) P_c^2 D^2 = \pi^2 \Gamma V^2 \quad \text{Equation 3.17}$$

$$\frac{mV(1-\kappa)C_0\xi_c}{D[1-(1-\kappa)I\nu(P_c)]} P_c^2 D^2 + G P_c^2 D^2 + \pi^2 \Gamma V^2 = 0 \quad \text{Equation 3.18}$$

$$\frac{mV(1-\kappa)C_0\xi_c P_c^2 D}{[1-(1-\kappa)I\nu(P_c)]} + G P_c^2 D^2 + \pi^2 \Gamma V^2 = 0 \quad \text{Equation 3.19}$$

Rearranging terms,

$$\pi^2 \Gamma V^2 + \frac{m(1-\kappa)C_0\xi_c P_c^2 D}{[1-(1-\kappa)I\nu(P_c)]} V + G P_c^2 D^2 = 0 \quad \text{Equation 3.20}$$

$$\frac{\pi^2 \Gamma}{P_c^2 D^2} V^2 + \frac{m(1-\kappa)C_0\xi_c}{D[1-(1-\kappa)I\nu(P_c)]} V + G = 0 \quad \text{Equation 3.21}$$

Following the approach of Kurz and Fisher [82], but using Ivantsov's solution for the transport problem, we obtain:

$$AV^2 + BV + C = 0 \quad \text{Equation 3.22}$$

Thus:

$$A = \frac{\pi^2 \Gamma}{P_c^2 D^2} \quad \text{Equation 3.23}$$

$$B = \frac{m C_0 (1-k) \xi_c}{D [1 - (1-k) Iv(P_c)]} \quad \text{Equation 3.24}$$

$$C = G \quad \text{Equation 3.25}$$

It should be taken into account that both the distribution coefficient,  $\kappa$ , and the liquid slope,  $m_l$ , are considered as constants for the purpose of simplicity. The quadratic Eq. 3.22 can be solved numerically for obtaining the variation of  $R$  (radius of the dendrite tip) with respect to  $V$  (solidification front velocity) for different conditions of temperature gradient. These calculations were made for the Co-Cr alloy system and the physical properties for that system are found from Co-Cr-6Mo-0.25C phase diagram and reported in Table 3.2.

On the other hand, in order to derive the distribution of solute (Cr) during the dendrite-columnar solidification of the Co-Cr alloy system, the equations corresponding to the radius of the dendrite tip ( $R$ ), and the solute gradient (Cr) at the tip of the dendrite can be combined. To obtain  $R$  as a function of the number of Peclet ( $P_c$ ) and, consequently, to have an expression for the concentration of the liquid  $C_l^*$  at the tip of the dendrite:

$$C_l^* = \frac{C_0}{[1 - p Iv(P_c)]} \quad \text{Equation 3.26}$$

Finally, a prediction of the concentration of solute in the solid at the tip of the dendrite,  $C_s^*$ , can be obtained as:

$$C_s^* = \kappa C_l^* \quad \text{Equation 3.27}$$

The importance of knowing the distribution of solute,  $C_s^*$ , along the columnar dendrite lies in the fact that when retaining about 100% solute (rapid solidification), there is no residual solute that can become interdendritic segregation and / or precipitates during the solidification of the Co-Cr alloys which translates into microstructures free of defects that can cause early fracture of the material. The forced dendritic growth model shown in this research work was considered to predict the radius of the dendrite tip,  $R$ , and the solute distribution,  $C_s^*$  during the growth of columnar dendrites, including velocities of growth in the range of the absolute stability limit.

It is known that rapid solidification helps to obtain fine microstructures and a minimum amount of interdendritic segregation. Considering that the mechanical properties of a material are intrinsically related to the microstructure of the material, having control during the growth of said microstructures is essential to develop new alloys with excellent properties. In this sense, it is widely documented that materials obtained from processes involving rapid solidification regimes exhibit better fatigue properties, resistance to corrosion and wear. As a consequence of the microstructural advantages mentioned above. Figure 3.13 shows the results obtained from Eq. 3.22 and 3.26. The curve corresponding to the radius of the tip of the dendrite for both temperature gradients ( $G = 0 \text{ K/m}$  and  $G = 500 \text{ K/m}$ ) decrease as the velocity of the solidification

front is increasing. This behavior is interrupted when a critical velocity value is reached to the same representing the transition in the velocity range between the constitutional super-cooling speed [ $V_{cs} = G D k / -m C_0 (1 - k)$ ] at the speed of absolute stability [ $V_{abs} = -m C_0 (1 - k) D / k^2 \Gamma$ ]. After the mentioned velocity transition, the radius of the dendrite tip (independent parameter of the thermal gradient in the liquid), continues to decrease until the absolute stability speed is reached. Dendrite tip radius value for the alloy was determined with scanning electron microscopy. This value was placed in the graph of Figure 3.13 ( $R$  = radius of the dendrite tip vs  $V$  = speed of the solidification front), with the purpose of finding the growth rate of the dendrites (columns). As can be seen in the graph, the solidification front speed reached during the directional growth of columnar dendrites for this alloy is close to 1 mm/s. Such solidification rate is high enough to retain virtually all Cr in solid solution, which is in agreement with the predictions.

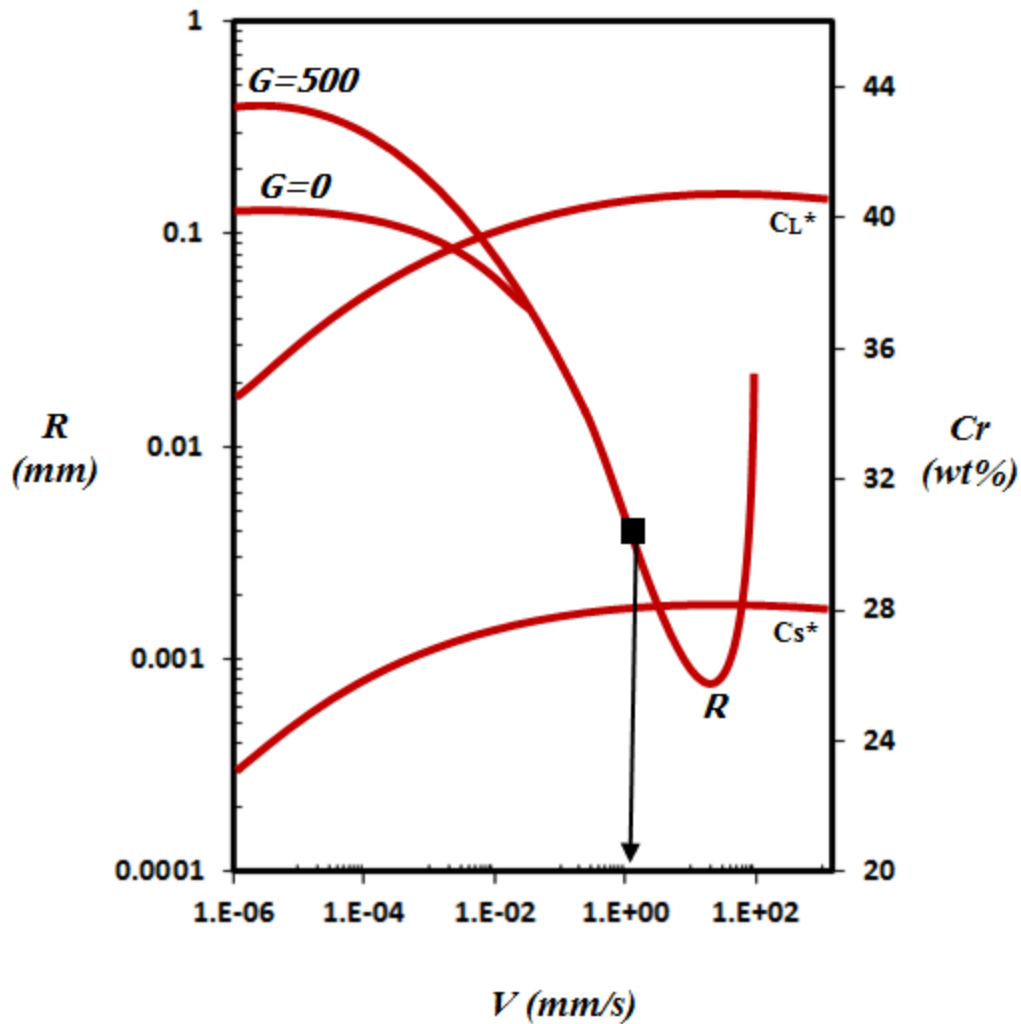


Figure 3.13 - Results of the mathematical model of directional solidification.

### 3.1.2. X-ray Diffraction (XRD)

The X-ray diffraction (XRD) patterns at the 20 mm, 60 mm and 90 mm locations of the wedge samples as well as sand cast mold sample (Figure 3.14) were obtained. From XRD analysis it was found that the directionally solidified dendrites for the Co-Cr-Mo-C alloys show up to 46 percentage of  $\epsilon$ -martensite phase ( $\epsilon$ -Co, HCP) 20 mm away from the tip of the wedge along with

precipitated carbides and  $\gamma$ -Co, FCC (austenite) phase. On all samples, XRD peaks originated from  $\gamma$ -FCC and  $\varepsilon$ -HCP phases were observed. Sage and Guillaud [83] proposed the quantitative model to calculate the developed HCP phase in the Co-alloy. According to their model, only the diffraction patterns corresponding to  $(002)_{\text{FCC}}$  and  $(10\bar{1}1)_{\text{HCP}}$  should be considered because they are the only well distinguished and not overlapped diffraction patterns at a given  $2\theta$ . The intensities of  $(002)_{\text{FCC}}$  peak at  $50.5^\circ$  and  $(10\bar{1}1)_{\text{HCP}}$  at  $46.5^\circ$  are used to calculate the volume fraction of  $\gamma$ -FCC and  $\varepsilon$ -HCP, respectively. The following equation [83] is used to calculate the FCC and HCP relative amounts quantitatively in Co-Cr-Mo-C alloy.

$$\frac{1-x}{x} = 1.5 \frac{I_{(002)\text{FCC}}}{I_{(10\bar{1}1)\text{HCP}}} \times 100 \quad \text{Equation 3.28}$$

Where  $x$  is HCP weight percentage,  $I_{(002)\text{FCC}}$  and  $I_{(10\bar{1}1)\text{HCP}}$  are integrated areas of the intensity peak correspond to FCC and HCP phases, respectively. Quantitative measurements of HCP developed phase by using Eq. 3.28 determines the formation of approximately 46%  $\varepsilon$ -martensite (HCP) phase in the sample with the highest cooling rate, 450 K/s, and less than 1% in the sample with the lowest cooling rate, 10 K/s. Increasing cooling rate will increase the amount of formed HCP. At the cooling rate of 120 K/s and 230 K/s the formed HCP measured to be 17% and 29%, respectively. Intrinsic stacking faults are known to be the potential sites for HCP phase nucleation as a result of lattice dislocations dissociating into Shockley partials. Because of relatively small stacking fault energy of Co-alloy, this transformation happens in the Co-alloy

spontaneously [26, 84]. Therefore, because of the lower amount of HCP phase in the low cooling rate sample it can be concluded that the volume fraction of stacking fault in this sample is low.

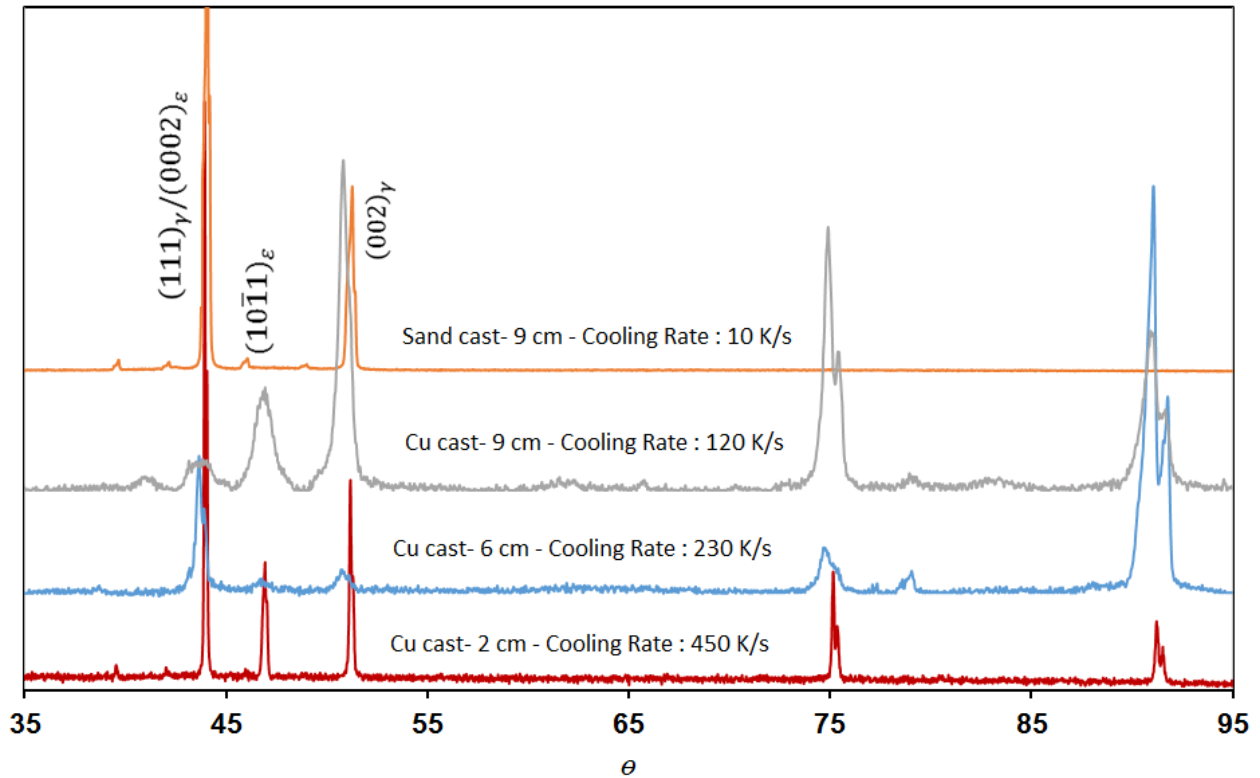
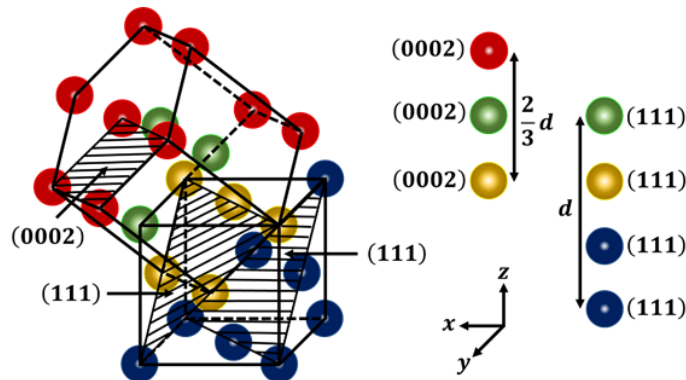


Figure 3.14 – XRD results of Co-Cr-Mo-C alloys regarding their cooling rate

Increase in the amount of  $\epsilon$ -martensite transformed athermally can be seen, which approximates a value of 46% induced through rapid solidification. The lattice parameters for the crystalline structures of the  $\gamma$ -Co, FCC and  $\epsilon$ -Co, HCP phases were calculated using Bragg's law and the corresponding crystallographic expressions for inter-planar spacing. The determinations of the lattice parameters for the  $\gamma$ -Co, FCC phase were based on the average values found from the diffraction peaks at positions (111), (200), (220) and (311). While for the  $\epsilon$ -Co phase, HCP peaks (101 $\bar{0}$ ), (0002) and (10 $\bar{1}$ 1) were used. It is well known [85] that the consistent growth in Bain's

distortion as presented in Figure 3.15 includes two mechanisms: 1) an invariant axis through coherent growth and 2) a contraction and expansion in the other axis of the net.



*Figure 3.15 - Schematic illustration of coherent growth between the  $\gamma$ -Co, FCC and  $\epsilon$ -Co, HCP phases in the austenite-martensite transformation. Note the relationship between the lattice parameter HCP and the major diagonal of the unit cell FCC.*

In cobalt base alloys, the martensitic transformation shows an invariant plane along the axis [111] and [0002] for the  $\gamma$ -Co, FCC and  $\epsilon$ -Co, HCP phases, respectively [85]. This implies that the magnitude of the lattice parameter  $\epsilon$ -HCP must be equal to  $2/3$  of the main diagonal of the unit cell FCC. From the X-ray diffraction data, the estimated lattice parameters are  $\gamma$ -FCC =  $3.4732 \text{ \AA}$  and  $\epsilon$ -HCP =  $3.9369 \text{ \AA}$  for the Co-Cr-Mo-C alloy in casting condition. From this result, a contraction in the c axis (normal to the basal plane) of approximately 1.89% was found which can be associated with an additional deformation contribution to the coherent deformation when the martensitic transformation occurs. Figure 3.16 is an SEM micrograph of the athermal  $\epsilon$ -HCP developed within the columnar dendritic structure in a Co-Cr-Mo-C alloy; in particular, notice the typical striations associated with the athermal  $\epsilon$ -HCP transformation.

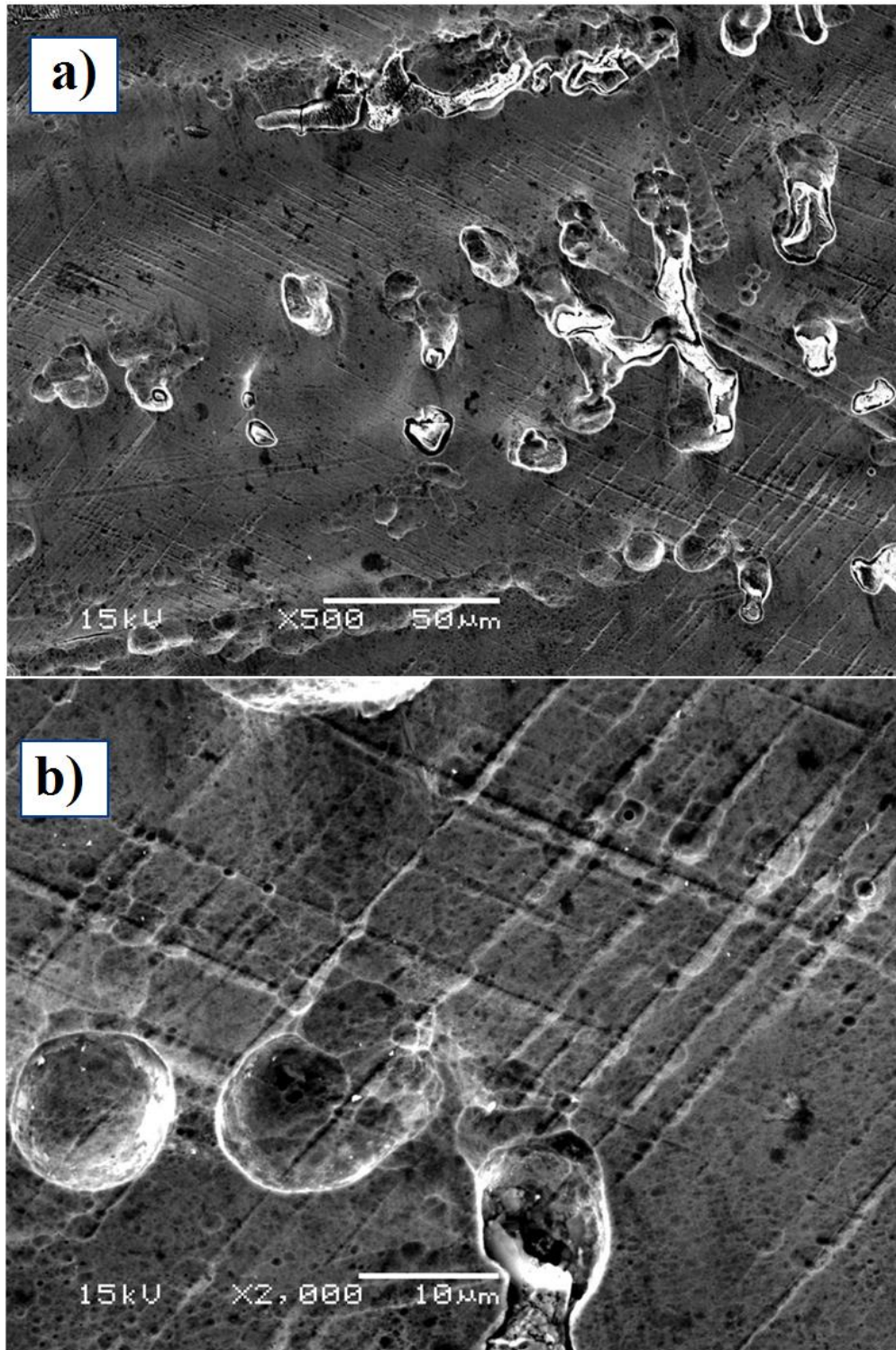


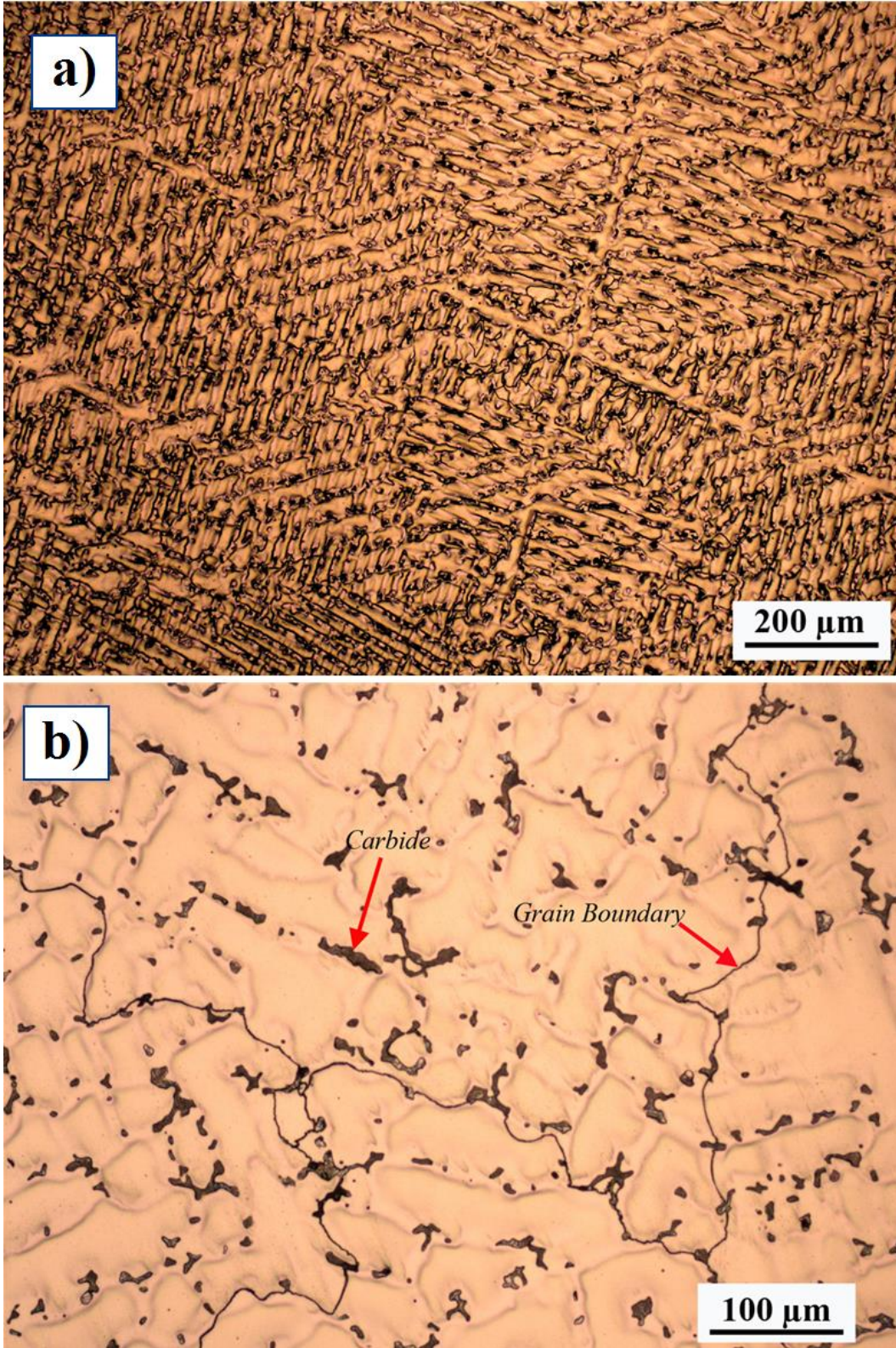
*Figure 3.16 – Showing the HCP phase formed in rapidly solidified Co-Cr-Mo-C alloy, 2cm from the tip of the Cu mold cast in two different magnifications.*

## **3.2. Laser modified surface**

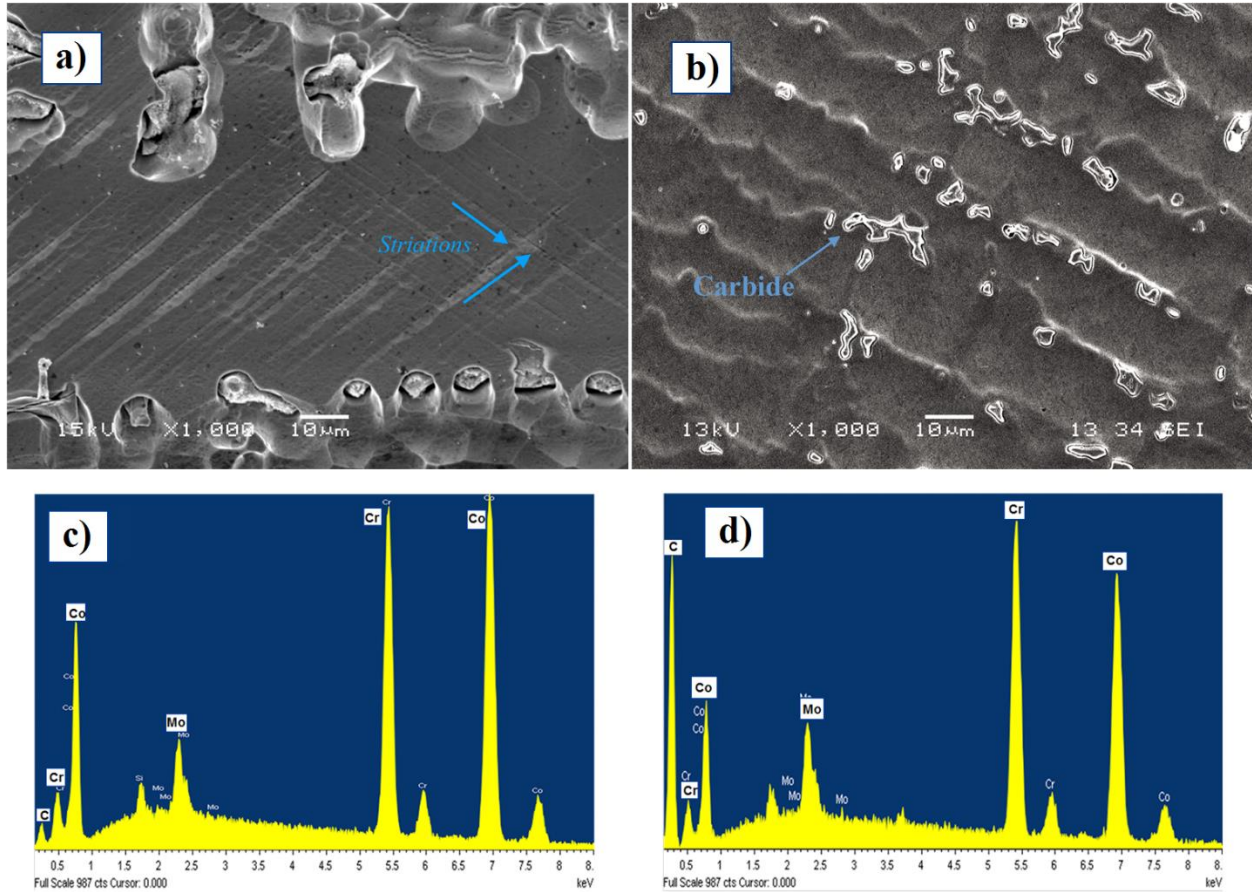
### **3.2.1. Microstructure analysis**

Figure 3.17 shows the exhibited microstructure of the investment cast Co-Cr-Mo-C alloy. Notice the dendritic structure (Figure 3.17a), as well as the distribution of coarse carbides at the interdendritic regions (Figure 3.17b). The size range of the precipitated carbides was found to oscillate between 5 and 25  $\mu\text{m}$  with an average size of 8  $\mu\text{m}$ . In addition, measurements of primary dendrite arm spacings (DAS) and secondary dendrite arm spacings (SDAS) yielded values of 45 $\mu\text{m}$  and 23 $\mu\text{m}$ , respectively.

Figures 3.18a-d are SEM micrographs of the investment cast Co-Cr-Mo-C alloy, including corresponding EDS graphs. From Figure 3.18a, athermal  $\epsilon$ -martensite is found to precipitate within the columnar dendritic structure as evidenced by the athermal  $\epsilon$ -martensite transformation striations. Figure 3.18b shows the presence of discontinuous strings of interdendritic carbides. The EDS results show a relatively small intensity peak corresponding to carbon as expected for the matrix (Figure 3.18c) and an appreciable intensification of the carbon peak where carbides are present (Figure 3.18d).



*Figure 3.17 – Optical images of the as-cast Co-Cr-Mo-C alloy showing (a) the dendritic matrix structure and (b) carbide precipitates in the interdendritic regions and at dendritic grain boundaries.*



**Figure 3.18 – SEM and EDS results of as-cast Co-Cr-Mo-C alloy showing (a) athermal  $\epsilon$ -martensite, (b) dendritic structure of as-cast alloy including carbides, (c) EDS peaks of alloying elements in the matrix and (d) EDS elements in precipitated carbides.**

The exhibited microstructure of the laser surface modified (LSM) Co-Cr-Mo-C alloy is shown in Figures 3.19a-b. At low magnification detailed microstructural features are not clearly resolved. Nevertheless, the interface between the solidified molten metal pool and the base as-cast alloy are clearly distinguished. Figure 3.19b shows the overlapping between solidified molten metal strings produced by the laser beam. The measured depth of the solidified pool is roughly 200  $\mu\text{m}$ . The HAZ is not easily resolved by optical means but it is found to consist of fine dendrites.

The microstructural features of the LSM regions were resolved by SEM means along with their corresponding EDS peaks (see Figures. 3.20a-d). In this work, it was found that the implemented pulsed laser conditions lead to the formation of a cellular front upon solidification of the molten pool (see Figure 3.20a). In addition, intercellular carbides are found to preferentially develop at cell corners in the solidified cellular front (see Figure 3.20b). The measured cell width, as well as size of intercellular carbides was 2  $\mu\text{m}$  and 200 nm, respectively. EDS analyses in both, matrix and intercellular carbides indicate that the precipitated carbides are Cr-rich (see Figures 3.20c-d). Notice that the composition of the cellular structure is rather similar to the one found in the as-cast Co-Cr-Mo-C alloy (see Figure 3.18c). The measured hardness of the as-cast alloy and LSM alloy are found to be 278 Vickers and 329 Vickers, respectively.

A cellular solidification front was found to develop as a result of rapid solidification induced by pulsed laser surface melting. Notice from Figure 3.20a, that the solidified pool consists of cellular grains containing a network of 2  $\mu\text{m}$  wide cells. In general, the exhibited solidified microstructure is a function of the temperature gradient,  $G$  and the solid growth rate  $R$  ratio,  $G/R$ . This ratio must equate or exceed  $\Delta T/D_L$  for a stable planar solid-liquid,  $S/L$  interface to be attained [78], where  $\Delta T$  is the melt undercooling ( $-m_l C_o [1 - k]/k$ ) and  $D_L$  is the solute diffusion coefficient in the liquid at the  $S/L$  interface. The development of a cellular solidification front is highly favored when the  $G/R$  ratio falls slightly below  $\Delta T/D_L$  giving rise to a relatively low extent of so-called constitutional super-cooling [78]. In the Co-Cr-Mo-C alloy, the  $G/R$  ratio was estimated from  $G/R = (-m_l C_o [1 - k]/k)/D_L$  [86] by considering the binary

Co-Cr phase diagram and the thermal data from Table 3.3, yielding values of  $G = 8.63 \times 10^7 \text{ }^\circ\text{C/m}$ , considering  $R = V$  (laser scan speed).

In laser and electro-beam pool melting, the exhibited solidification mode is directly influenced by the relatively low heat input ( $Q$ ) of these processes [87] which for a given laser melting speed ( $V$ ) tends to occur under relatively high  $G/R$  ratios. Accordingly, the development of either planar or cellular solidification fronts is commonly reported in laser or electron beam welding [88, 89]. An estimation of thermal gradients and resultant cooling rates under which the cellular solidification occurs in the Co-Cr-Mo-C alloy can be obtained by considering the 3-D Rosenthal Equation:

$$T - T_o = \frac{AP_L}{2\pi kr} \exp\left(\frac{-V(r-x)}{2\alpha}\right) \quad \text{Equation 3.29}$$

Where  $T$  is the molten pool temperature,  $T_o$  = room temperature,  $P_L$  = laser power and  $A$  = laser efficiency,  $K$  = thermal conductivity  $\alpha$  = thermal diffusivity,  $V$  = laser scanning speed,  $r = \sqrt{x^2 + y^2 + z^2}$  is the pool radius, Table 3.3 gives selected cobalt thermal properties, as well as LSM parameters.

**Table 3.3 - Laser melting parameters and cobalt thermal properties**

$T-T_o$ ( $^\circ\text{C}$ )	$V$ (mm/s)	$P_L$ (W)	$A^*$	$K$ [90] (W/(m·K))	$\alpha$ (cm <sup>2</sup> /s) [90]	$C_o$ (wt%)	$k$	$m_l$ ( $^\circ\text{C}/\text{wt}\%$ )	$D_l$ (cm <sup>2</sup> /s)[90]
1400	3.2	487.5	0.3	33	$7.45 \times 10^{-6}$	28	0.26	-3.00	$8.86 \times 10^{-5}$

\*Note: A low efficiency is assumed due to laser beam reflection;  $m_l$  is the slope of the liquidus line and  $k$  the solute partition coefficient for the binary Co-Cr alloy system;  $C_o$  is the alloy Cr content.

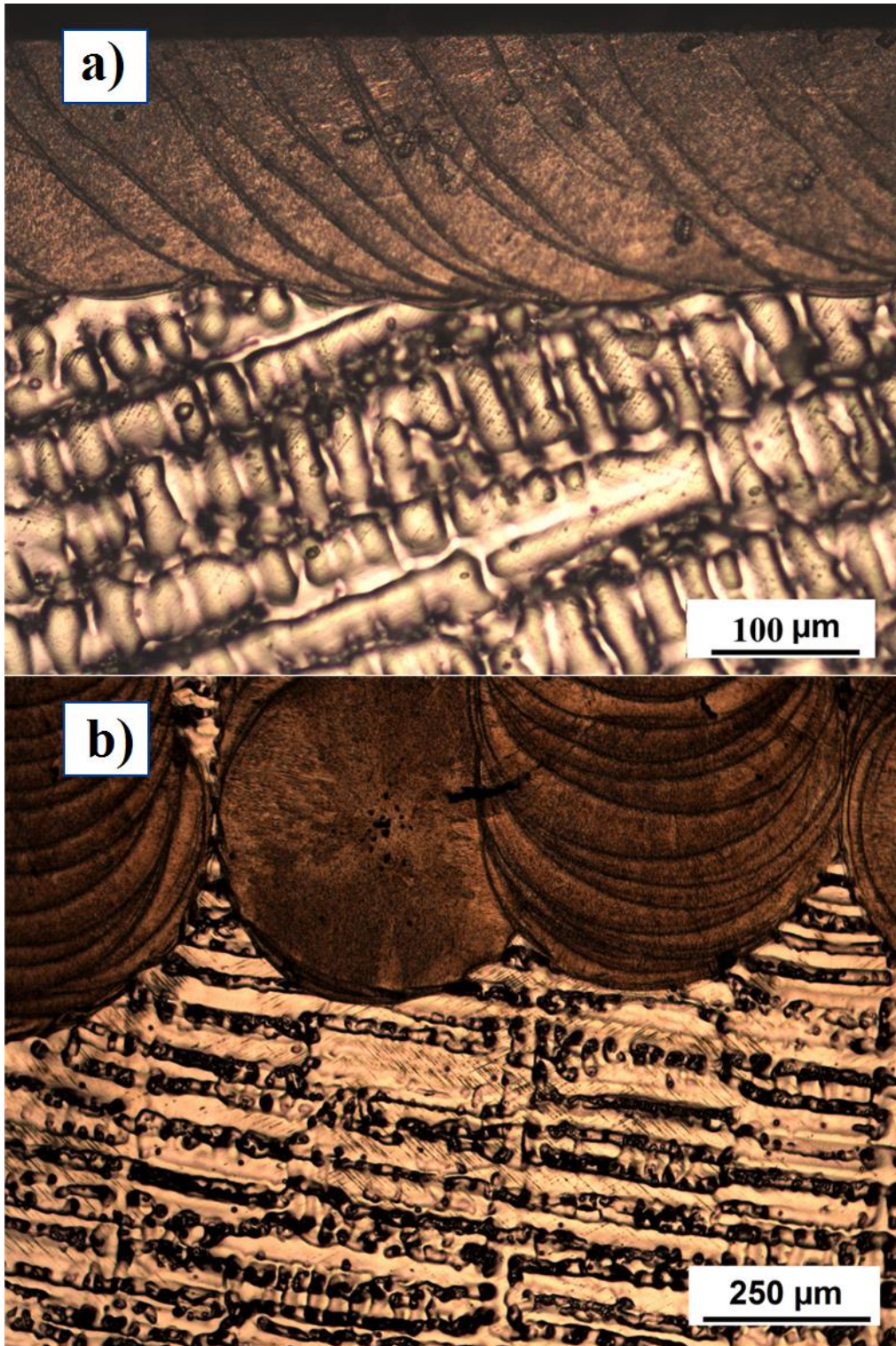


*Figure 3.19 - Optical images of the Co-Cr-Mo-C alloy after pulsed laser (a) Side view of the solidified metal pool and surrounding as-cast alloy b) front view of solidified metal string beads.*

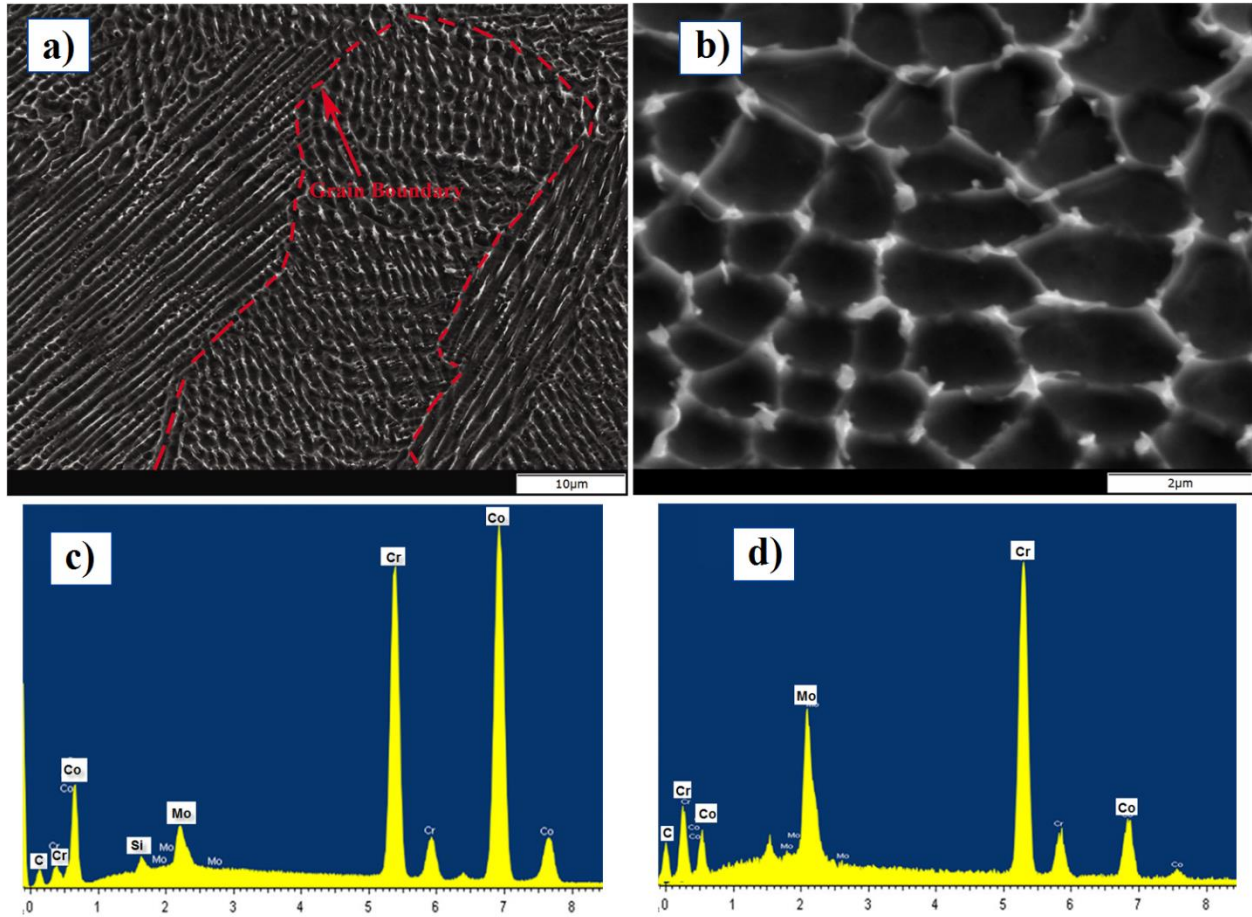


*Figure 3.20 – SEM images of solidified LSM Co-Cr-Mo-C alloy. (a) Solidified cellular structure, (b) cellular solidified front showing the carbide distribution in the cell boundaries, (c) EDS peaks of alloying elements in cellular matrix and (d) EDS peaks of elements in intercellular carbides.*

In Equation, 3.29 a moving point heat source is considered where quasi-steady state heat flow is reached and only conduction heat flow is attained for simplification purposes. From this equation solidification cooling ( $dT/dt$ ) can be obtained through differentiation,  $dT/dt = -VT/r \left[ \frac{x}{r} - (Vr/2a)(1 - x/r) \right]$ . Moreover, along the centerline (x-axis) of the molten laser pool (i.e.,  $r = x$ ),  $dT/dt$  can be estimated by considering that at the center line crystal growth,  $\mathbf{R}$  and the solidification velocity  $\mathbf{V}$  (laser scanning speed) are parallel to each other, (i.e  $\mathbf{R} = \mathbf{V}$ ).

Under these conditions the cooling rate along the centerline  $dT/dt = \theta = G \times R$  is given by  $-2\pi KV(T - T_o)^2/AP_l$  and the thermal gradient by  $G = (dT/dx) = \theta/V$ .

Using the parameters for cobalt (Table 3.3), cooling rates can be estimated all the way from melting to room temperature yielding  $dT/dt = 8892$  °C/s. Also, thermal gradients  $G$  as high as  $2.78 \times 10^6$  °C/m are estimated to occur at the centerline location. Accordingly, the condition for the development of a planar front at the S-L interface ( $G/R > \Delta T/D_L = 8.63 \times 10^7$  °C/m) is not attained in the Co-Cr-Mo-C alloy. Yet, relatively high  $G/R$  values develop which account for the observed cellular morphology. Moreover, the exhibited fine intercellular spacing,  $\lambda$ , can be related to the relatively large  $GV$  values as  $\lambda$  is directly proportional to  $(GV)^{-1}$  [86]. Apparently, relatively high cooling rates including elevated thermal gradients develop during LSM accounting for the presence of a cellular solidification front.

In the LMS of the cobalt alloy, a close inspection indicates that the cell cross-sections are characterized by a fine distribution of carbide phases of nano-metric sizes (see Figure 3.19b). Moreover, determinations using X-ray diffraction indicates that the matrix of the cellular microstructure is fully  $\gamma$ -FCC phase (see Figure 3.21b). Apparently, no measurably hexagonal athermal  $\epsilon$ -martensite develops in the cellular matrix. Besides, there is no evidence for the development of stacking faults or dissociated dislocations. The combination of a fully FCC matrix with a uniform distribution of carbide particles in a fine cellular microstructure is expected to provide a combination of outstanding corrosion and mechanical and tribological properties (as expected from the high hardness exhibited by LSM) as previously reported [91].

As it was previously mentioned in section 3.1, in the investment cast alloy two types of carbides were dominant and they were identified as blocky and lamellar shaped carbides [92]. According to Tylor and Waterhouse [45] these carbides are likely to be  $M_{23}C_6$  and  $M_6C$ . Also, when Mo is present in relatively large amounts  $M_6C$  can precipitate [93]. In this work EDS results (Figure 3.17d) suggest that in the as-cast alloy, Cr is the dominant carbide alloying element, typical of blocky shaped carbides. In the LSM alloy the type of carbides found in the solidified pool was not fully determined due to its fine size, but it is expected to be similar in composition to the ones found in the as-cast base alloy ( $M_{23}C_6$ ).

In the as-cast Co-Cr-Mo-C alloy, the exhibited amounts of athermal  $\epsilon$ -martensite (13 Vol%) indicate that the  $\gamma$  to  $\epsilon$  transformation is severely hindered probably due to the lack of enough defects that can act as effective nucleation sites [94]. Rapid solidification has been reported to promote the development of effective nucleation sites for the formation of  $\epsilon$ -athermal martensite when the solidified microstructure is dendritic [50]. Nevertheless, the presence of a cellular structure is concomitant with a lack of defects (stacking faults and dissociated dislocations) needed for the nucleation of athermal  $\epsilon$ -martensite. In turn, the overall effect is the suppression of the  $\gamma$  to  $\epsilon$  athermal transformation in the LSM Co-Cr-Mo-C alloy.

### **3.2.2. X-ray diffraction**

The exhibited crystal structures of both, the as-cast and the LSM Co-alloy were disclosed by XRD means as seen in Figures 3.20a and 3.20b, respectively. It was found that both  $\gamma$  and  $\epsilon$  phases are present in the as-cast alloy. In contrast, the  $\epsilon$ -phase was absent in the cellularly

solidified pool. Quantitative measurements of the developed athermal  $\varepsilon$ -martensite resulted in a 13 vol. % in the as-cast condition with no detectable HCP phase in the LSM regions.

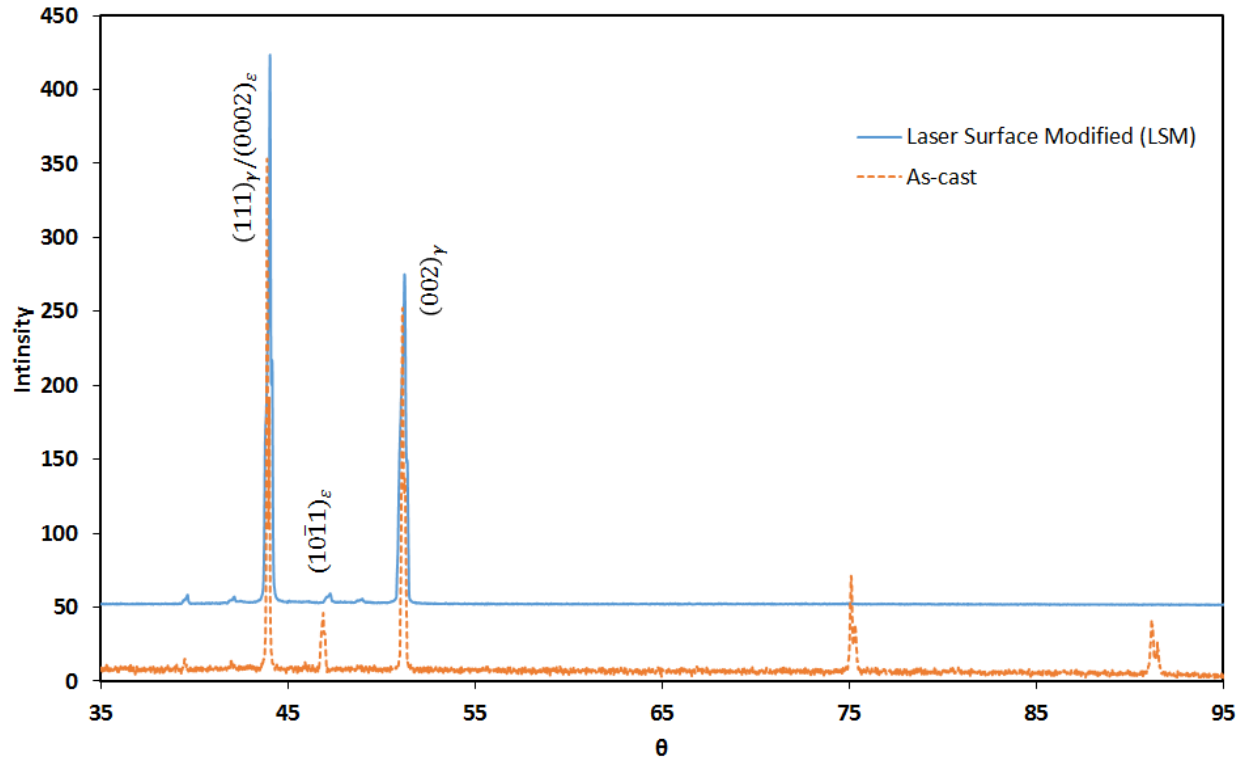


Figure 3.21- XRD results of Co-Cr-Mo-C alloy a) As-cast b) Laser surface modified (LSM).

### 3.3. Heat Treatment of Co-Cr-Mo-C rapidly solidified alloy

Apparently, during carbide precipitation, the interface regions on the matrix side become depleted in Cr and Mo, locally modifying the  $\gamma'_{HCP}$  to values that makes it difficult to develop  $\varepsilon$ -martensite embryos. Among the solutes that are expected to play a critical role in the transformation process is carbon. A similar or even stronger effect on the transformation process is linked to nitrogen in Co-Cr alloys [95]. As mentioned in section 1.3.1, the isothermal martensitic transformation is associated with the precipitation of rows or strings of carbides

and/or carbonitrides. These carbides are not found in untransformed regions (FCC), even though athermal martensite can be developed there (see Figure 1.14). Moreover, in the as-quenched condition, there is no evidence of significant carbide precipitation reactions. Hence, upon quenching from the annealing temperature, carbon remains in solid solution either at interstitial sites in the transformed HCP athermal martensite or at the FCC metastable phase. Because the carbon solubility in HCP cobalt is nearly zero according to the phase diagram, Figure 3.22, it is expected that  $\gamma'_{HCP}$  will increase significantly with carbon or nitrogen supersaturation at interstitial HCP sites and at dislocation cores. Preferential segregation at stacking faults is strongly opposed. Thus, from the Suzuki segregation equation, the effect of interstitials on  $\gamma'_{HCP}$  can be described by [96].

$$d\gamma'_{HCP} = - \left[ \Gamma_i - \left( \frac{C_i}{C_1} \right) \Gamma_1 \right] d\mu_i \quad \text{Equation 3.30}$$

where  $\Gamma_i$  is the surface excess of interstitial carbon or nitrogen,  $\Gamma_1$  is the surface excess of solvent,  $C_1$  is the mole fraction of solvent, and  $C_i$ ,  $\mu_i$  are the mole fraction and chemical potential of carbon or nitrogen, respectively. Accordingly, the changes in stacking fault energies can lead to relatively high  $\gamma'_{HCP}$  values depending on the local interstitial content.

The Co-Cr-Mo-C alloy samples were solutionized at 1150 °C for 1 hour and then aged at 750 °C, 800 °C, 850 °C, and 900 °C for different times (3 hours to 25 hours). Figure 3.23 shows the presence of the  $\epsilon$ -martensite phase and intragranular striations in samples aged at 850 °C for 5, 10 and 20 hours. Main microstructural features were similar among the samples heat-treated at 850 °C, but the morphology of carbide phase changed from blocky shape into globular.

Significant decrease in volume fraction of the  $\gamma$  phase is exhibited in the alloy heat-treated at 850 °C for 20 hours. Furthermore, the dendritic structure disappears, Figure 3.23c. Figure 3.23d shows that in higher magnification, the interdendritic precipitates eventually disappears consequently a homogeneous microstructure will be achieved.

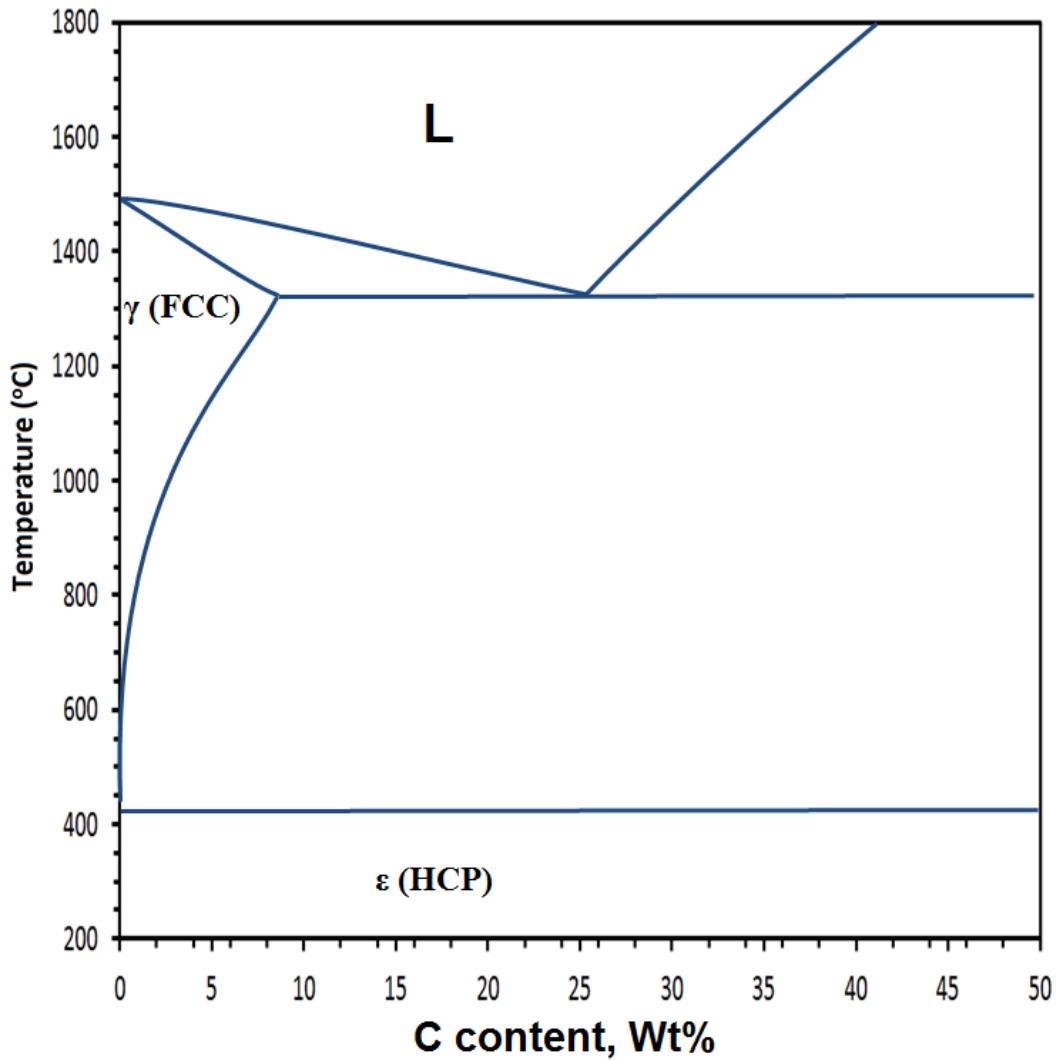
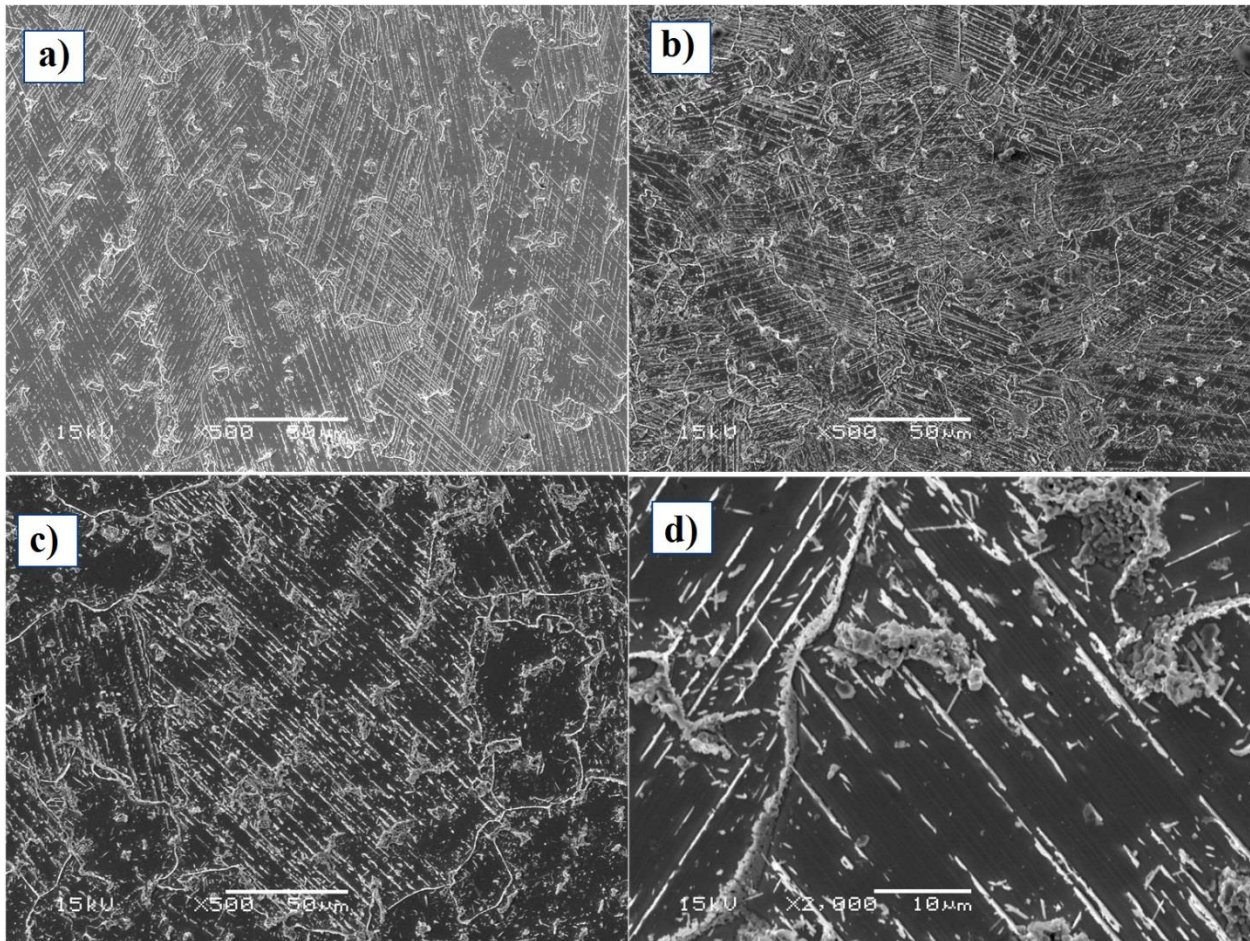


Figure 3.22 – Phase diagram of Co-C, shows zero solubility of carbon in HCP cobalt alloy [40].



**Figure 3.23 – Co-Cr-Mo-C alloy after ageing heat treatment solutionized at 1150 °C for 1 hour and then aged at 850 °C for a) 5 hours, b) 10 hours, c) 20 hours d) 20 hours in 2000x magnification**

The best wear properties in Co-based alloys are found when the alloy matrix is fully HCP, either in metal on metal wear couples, or in metal on UHDPE wear couples [24, 91]. Nevertheless, the fatigue properties are significantly reduced when the matrix is fully HCP. Apparently, the limited number of slip systems in the HCP matrix severely limits plastic deformation, thus promoting fatigue cracking. Moreover, the mechanical properties (strength and ductility) of Co based alloys are strongly influenced particularly by the amount of carbon, nitrogen grain size and by the processing route (casting versus brought or powder processing).

Figure 3.23a shows Co-Cr-Mo-C alloy after ageing at 850 °C for 5 hours. Notice the drastic change in morphology as a result of a carbide precipitation reaction. In this micrograph, the triangular striations correspond to athermal martensite formed in the FCC phase.

Thermodynamically speaking, the effect of C can be described by the phase diagram for a given alloy composition. Figures 1.3 and 1.5 are the Thermocalc diagrams for the Co-28Cr-6Mo-XC alloy systems. Notice from these figures that carbon expands the field of stability of both, the  $\epsilon$ -phase as well as of the carbide phases.

### **3.3.1. Effect of heat treatment on mechanical properties and X-ray diffraction patterns**

Figure 3.24 shows the X-ray diffraction patterns of the as-cast alloy and heat-treated alloys at 800 °C for 7, 10, and 15 hours, all the XRD results are reported in appendix Table 6.1A. The relative intensities of the measured diffraction peaks are associated with  $\gamma$  phase and  $\epsilon$  phase of Co. No significant degree of peaks exists except the  $\gamma$  phase and  $\epsilon$  phases of Co, suggesting that no significant number of additional phases exist. The complete analysis of  $\epsilon$ -martensite phase formed in heat treated Co-Cr-Mo-C alloy samples is shown in Figure 3.25 in a form of Transformation-Time-Temperature diagram.

Prolonged ageing at the higher temperatures also affect the stability of  $\gamma$  phase. As shown in Figure 3.24, the intensity of  $\gamma(200)$  diffraction peak of the alloy heat-treated at 900 °C for 25 h significantly decreases. Accordingly, the higher ageing temperature as well as prolonged ageing time can suppress the athermal martensitic transformation from  $\gamma$  phase to  $\epsilon$  phase, resulting in an increase in volume fraction of the retained  $\gamma$  phase at room temperature. This can be associated with reduction of the driving force for the martensitic transformation because of

elimination of the intrinsic stacking faults and dislocations during higher temperatures and longer heat-treating time. In addition, the concentration of Cr and Mo solute in the  $\gamma$  phase is enriched and reaches the final composition of 28.54 and 5.43 wt%, respectively, by the heat treatment because of the dissolution of the  $\gamma$  phase containing higher amount of Cr and Mo than the  $\epsilon$  phase. Thus, it is likely that the athermal martensitic transformation from  $\gamma$  to  $\epsilon$  phase can be affected by the variation in the chemical composition of the  $\gamma$  phase. As a result, the stability of the  $\gamma$  phase can be promoted by heat treatment.

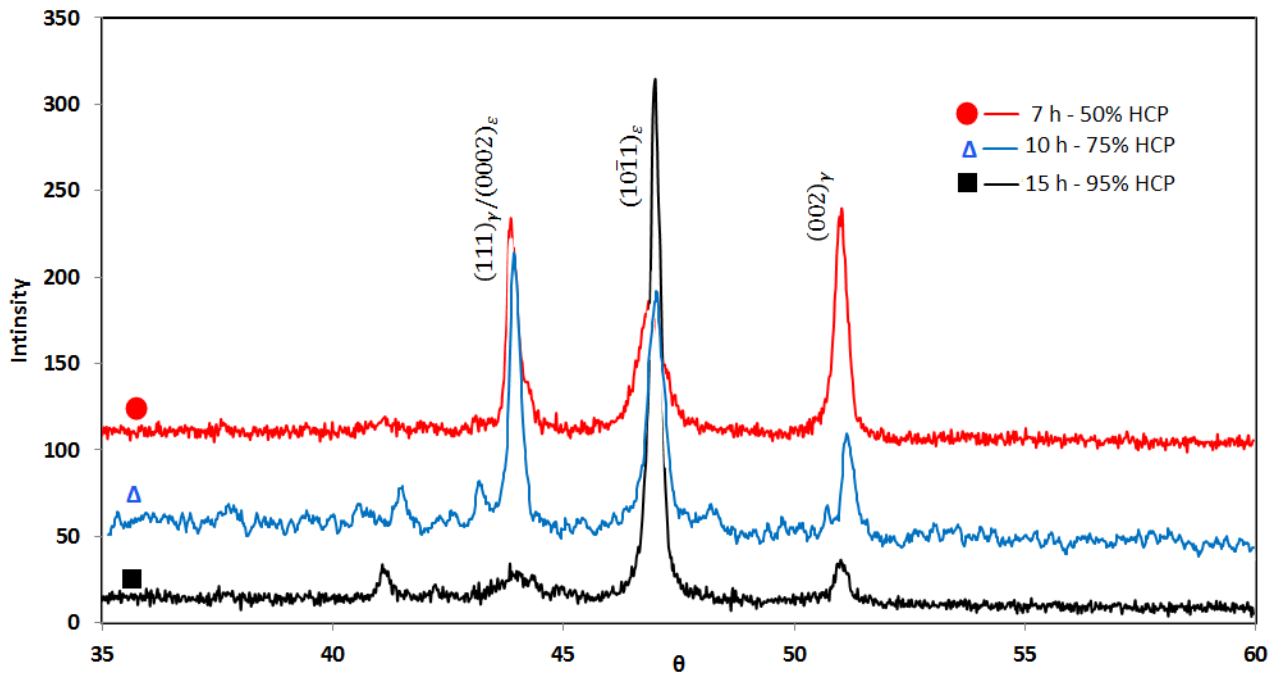


Figure 3.24 - XRD results of Co-Cr-Mo-C alloy aged at 800 °C for 7 h, 10 h, and 15 h.

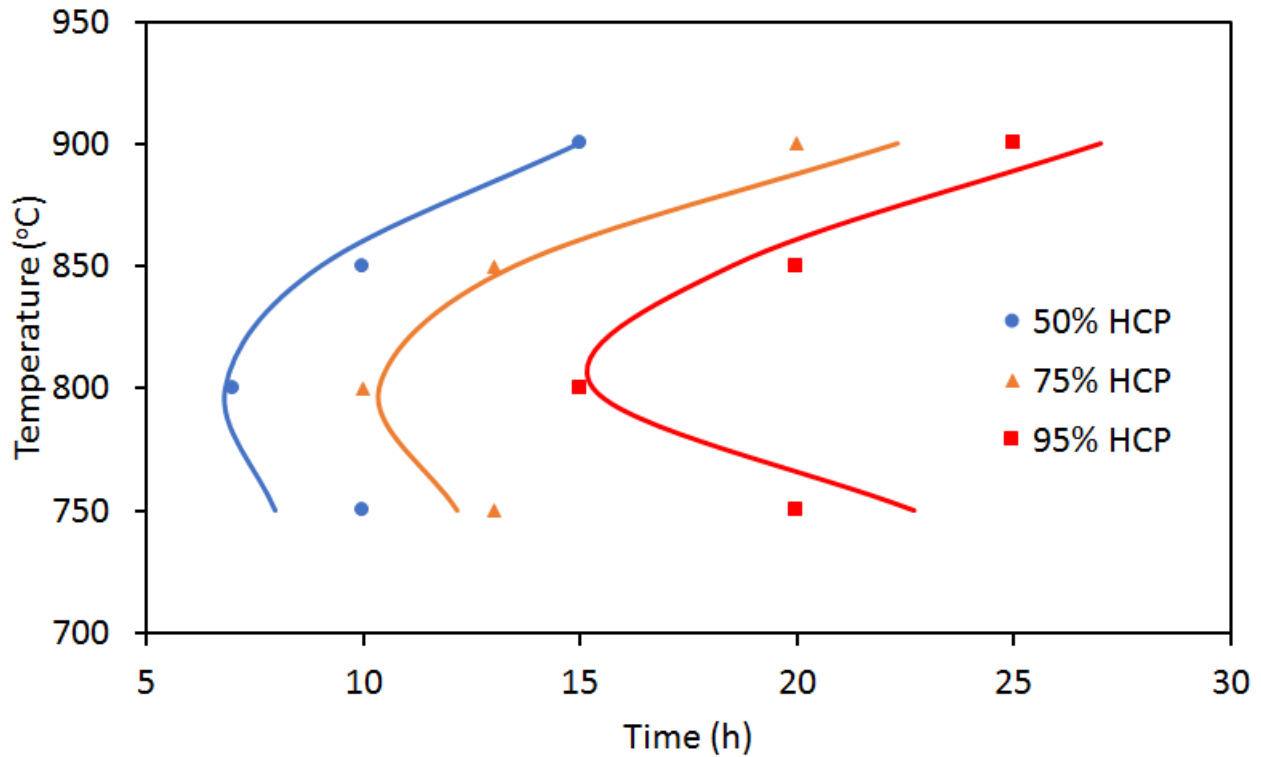


Figure 3.25 - Transformation-Time-Temperature diagram for the Co-Cr-Mo-C alloy.

### 3.4. Corrosion test

Figure 3.26 shows the anodic and cathodic polarization curves for Co-Cr-Mo-C alloy in rapidly solidified, as-cast, and laser surface modified conditions in Ringer's solution. Corrosion parameters such as  $E_{\text{corr}}$ ,  $i_{\text{corr}}$ ,  $b_a$  and  $b_c$  are measured and reported in Table 3.4. According to the results, increasing the cooling rate improves the electrochemical behavior of the alloy. The samples under higher cooling rate show higher corrosion potential and lower corrosion rate. The results show that the as-cast sample has the lower  $E_{\text{corr}}$  and higher  $i_{\text{corr}}$  than the laser surface modified sample. The cathodic current densities show a rather linear region with a negative slope from the  $E_{\text{ocp}}$  to -0.64V and -0.56V for the as-cast and laser surface modified alloys, respectively

and then the slope increase to zero. No significant differences are detected in the cathodic current densities.

The anodic part of the polarization curve demonstrates that all samples passivated by anodic polarization. Region of passivity for as-cast and laser surface modified is at the potential of -0.10V to 0.20V and -0.02V to 0.19V, respectively. The as-cast sample was found to have a wider passivity region. Also, the secondary passive and transpassive regions are observed. The primary transpassive potential for the as-cast sample is 0.31V and the sample is repassivated at a potential between 0.68V to 0.72V. For laser surface modified sample, transpassive potential is 0.24V and the sample does not display secondary passivity region.

Solidified structure, size and distribution of carbides and the amount of HCP phase characterize each sample. This means that different microstructural properties affect the corrosion behavior of samples. Better corrosion resistivity obtained by rapidly solidification is believed to be the result of better distribution of alloying elements, carbides, and a lack of grain boundaries. Figure 3.27 shows an optical image of the samples microstructure solidified at different cooling rate. As it shown in Figure 3.27, increasing cooling rate highly reduces the density of grain boundaries.

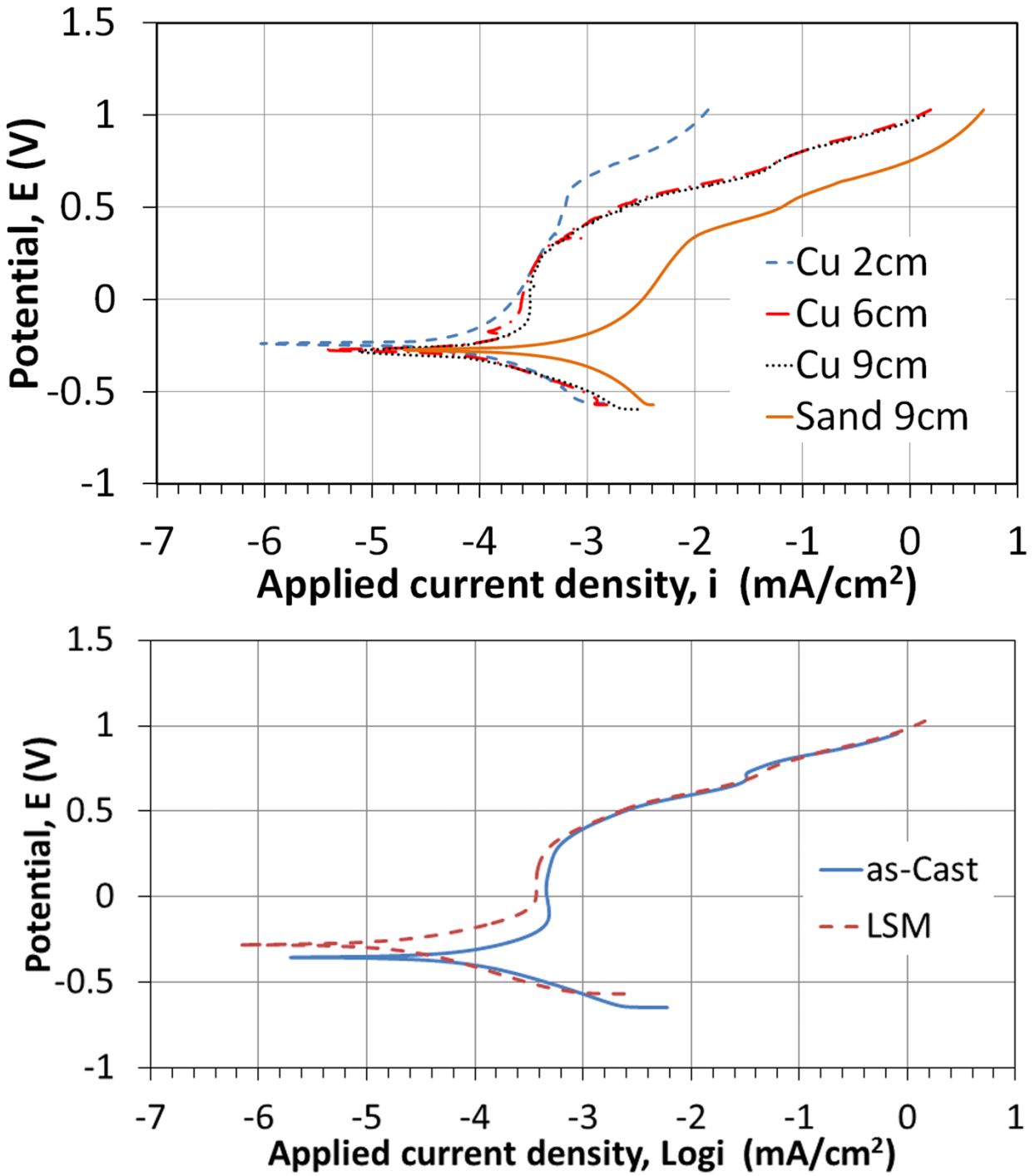
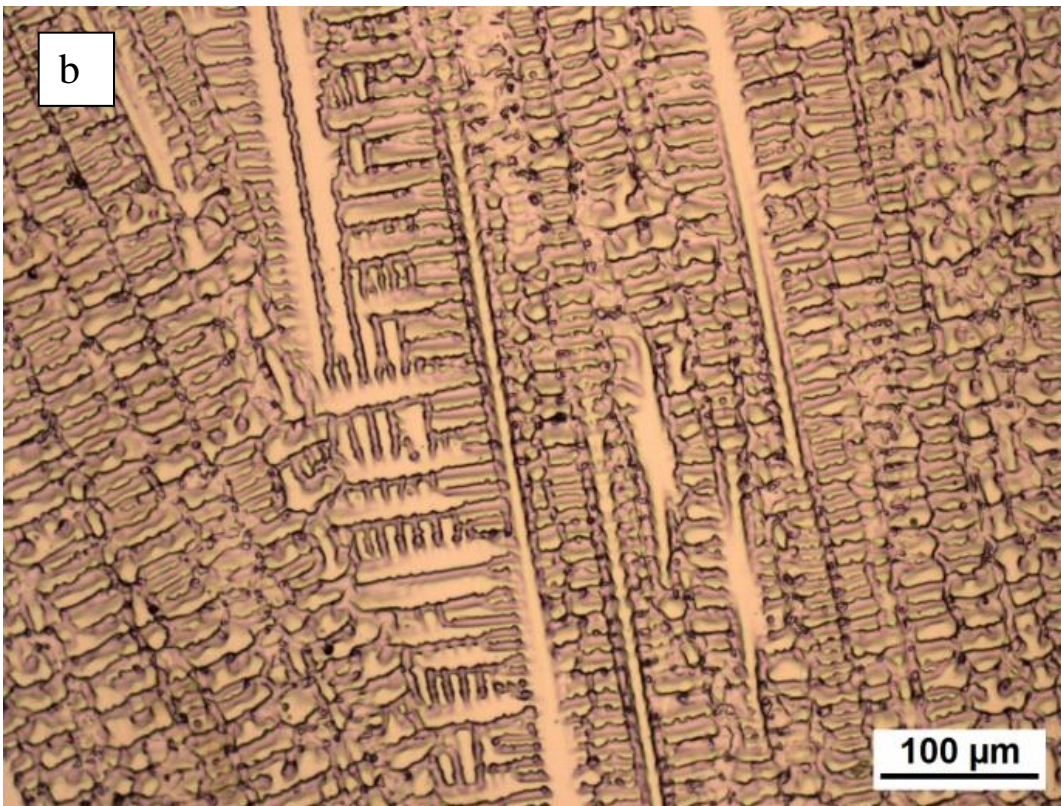
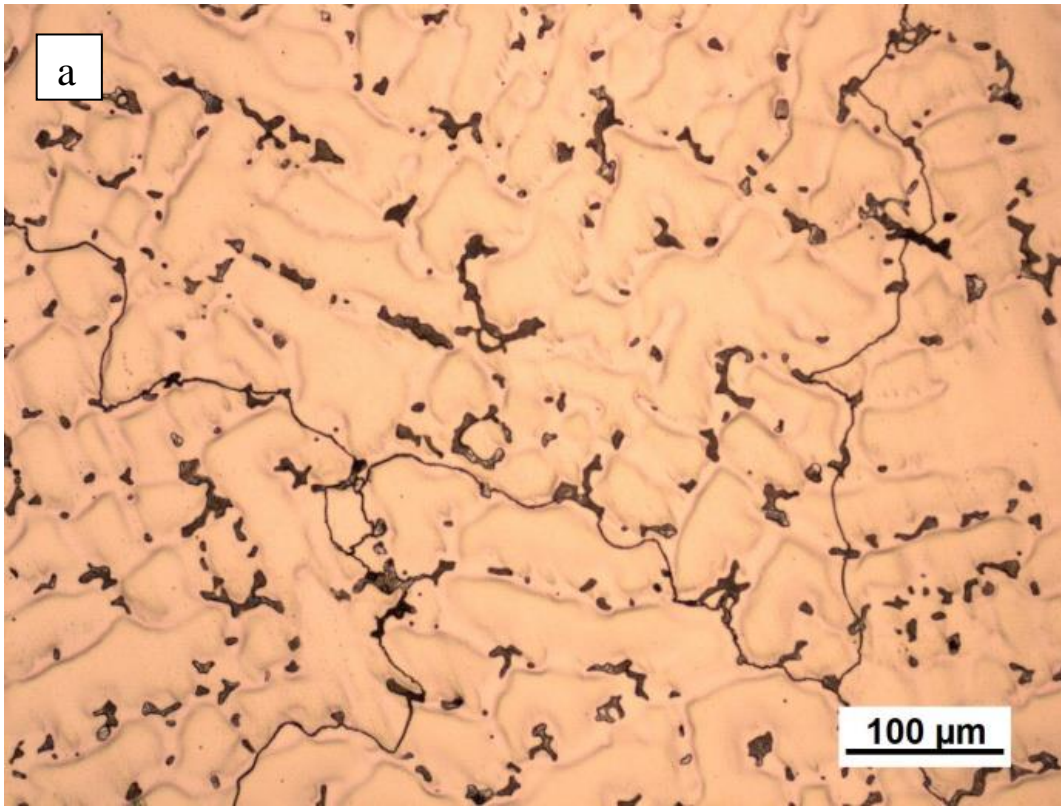


Figure 3.26 – Potentiodynamic curves for Co-Cr-Mo-C alloy in different conditions (Cu: Cu mold cast, Sand: Sand mold cast).



*Figure 3.27 – Optical microstructure of Co-Cr-Mo-C in different casting conditions, a) Sand cast- 9cm from tip and b) Cu mold cast- 2cm from tip*

*Table 3.4 Corrosion parameters for Co–Cr–Mo–C alloys in Ringer’s solution*

Sample/Distance from tip	$b_a$ (mV)	$-b_c$ (mV)	$i_{corr}$ ( $\mu\text{A}/\text{cm}^2$ )	$E_{corr}$ (mV)
Cu mold cast/2 cm	135	141	0.02	-240
Cu mold cast/6 cm	171	170	0.07	-270
Cu mold cast/9 cm	185	191	0.06	-278
Sand cast/9 cm	175	171	0.09	-280
As-cast	170	152	0.08	-356
Laser surface modified (LSM)	142	177	0.03	-281

The results of corrosion test also reveal better corrosion resistivity was achieved after applying laser welding on the surface of as-cast Co-alloy. Laser surface modified sample has the finer grain size; generally it is believed that increasing the volume fraction of grain boundaries as a result of decreasing the grain size makes the sample less corrosion resistant and shifts the  $E_{corr}$  to negative. Therefore, because of better electrochemical behavior of laser modified surface sample, the grain size is not the dominant microstructural feature to affect the corrosion resistivity of the sample.

C. Brito et al. [97] studied the effect of cellular and dendritic microstructure on corrosion behavior of Al-alloy. They found by altering the microstructure from cellular to dendritic the corrosion rate will increase. This improved electrochemical behavior of the cellular structure can be related to homogenous distribution and finer size of the intermetallic compound in the cellular regions due to rapid solidification. Consequently, laser modified sample with a cellular structure and small carbides size and better distribution of carbides exhibits increasing corrosion resistivity in comparison with the as-cast sample.

On the other hand, the protectiveness of passive oxide layer in the as-cast sample is higher due to its wider passivity region. The reason of narrower passivity region of laser surface modified samples can be attributed to the carbides size and distribution. The dispersion of carbides causes the increase in local active cell between carbides and base alloy, and then the increase in local corrosion is the result [25]. Local corrosion during passivity causes failure in oxide films and consequently smaller passivity regions in laser surface modified samples. The increase in the grain boundary volume fraction and the precipitates at the grain boundaries cause a decrease in protectiveness of the passive oxide film [25]. Laser surface modified sample does not show any secondary passive region which indicates that the oxide layer dissolution has occurred.

The exhibited corrosion resistance found in the investigated cobalt alloy can be related to the solidified microstructure, carbide size and distribution, as well as, to the amount of  $\epsilon$ -martensite phase present in the alloy. The results indicate that improved corrosion resistance is achieved by LSM processing as shown in Figure 3.26 and Table 3.4. In general, structural alloys exhibit improved corrosion resistance due to protective oxide films formed on their surfaces [98-100]. Corrosion involves surface redox reactions (metal oxidation coupled with solution reduction) and interfacial transfer of the charged species involved in the redox reactions. Hence the presence of an oxide film hinders the interfacial charge transfer, reducing the corrosion rates [98].

The LSM microstructure possesses a fine intercellular size and a uniform distribution of nanometric size carbides. Accordingly, the improved electrochemical behavior exhibited by the cellular structure can be related to the homogenous distribution of nanometric carbides coupled with the lack of any significant segregation effects due to rapid solidification which eventually

creates a rather uniform oxide layer. In a related work, Brito et al. [97] studied the effect of cellular and dendritic microstructures on the corrosion behavior of an Al-alloy. In their work, they found that by altering the microstructure from dendritic to cellular the corrosion rate decreases. In turn, they related improvements in corrosion behavior to the refined cellular microstructure and to an extensive distribution of fine second phases along the intercellular regions.

Figure 3.28 shows the distribution of alloying elements in the LSM cobalt alloy. Notice the homogeneous nature of the distribution of elements such as Cr, Mo and C. No appreciable build-up of solute is found which in turn indicates a lack of significant solute segregation. The development of a non-segregated microstructure such as in cellular solidification leads to a reduced corrosion rate. In particular, there is a drop in corrosion potential across the growing oxide layer in the LSM Co-Cr-Mo-C alloy.

Alternatively, from the polarization curves it is evident that the protectiveness of the passive film in the as-cast alloy is superior as evidenced by its relatively wide passivity region. In the LSM alloy a narrow passivation region is present. This can be attributed to a local increase in the active cell between the fine carbides and the surrounding cellular alloy matrix [25]. The pitting resistance is associated with the number of pit initiation sites (carbides) and also the extent of Cr-depletion around these carbides [101, 102]. It is well known that local corrosion during passivity can cause breakdown in the passivation film. Thus, a relatively small passivity region can lead to a limited protectiveness of the passive oxide film in the LSM alloy [25]. Also, notice that the

LSM alloy does not show any secondary passivation region which in turn indicates that dissolution of the oxide layer occurs at corrosion potentials near 0.4 mV.

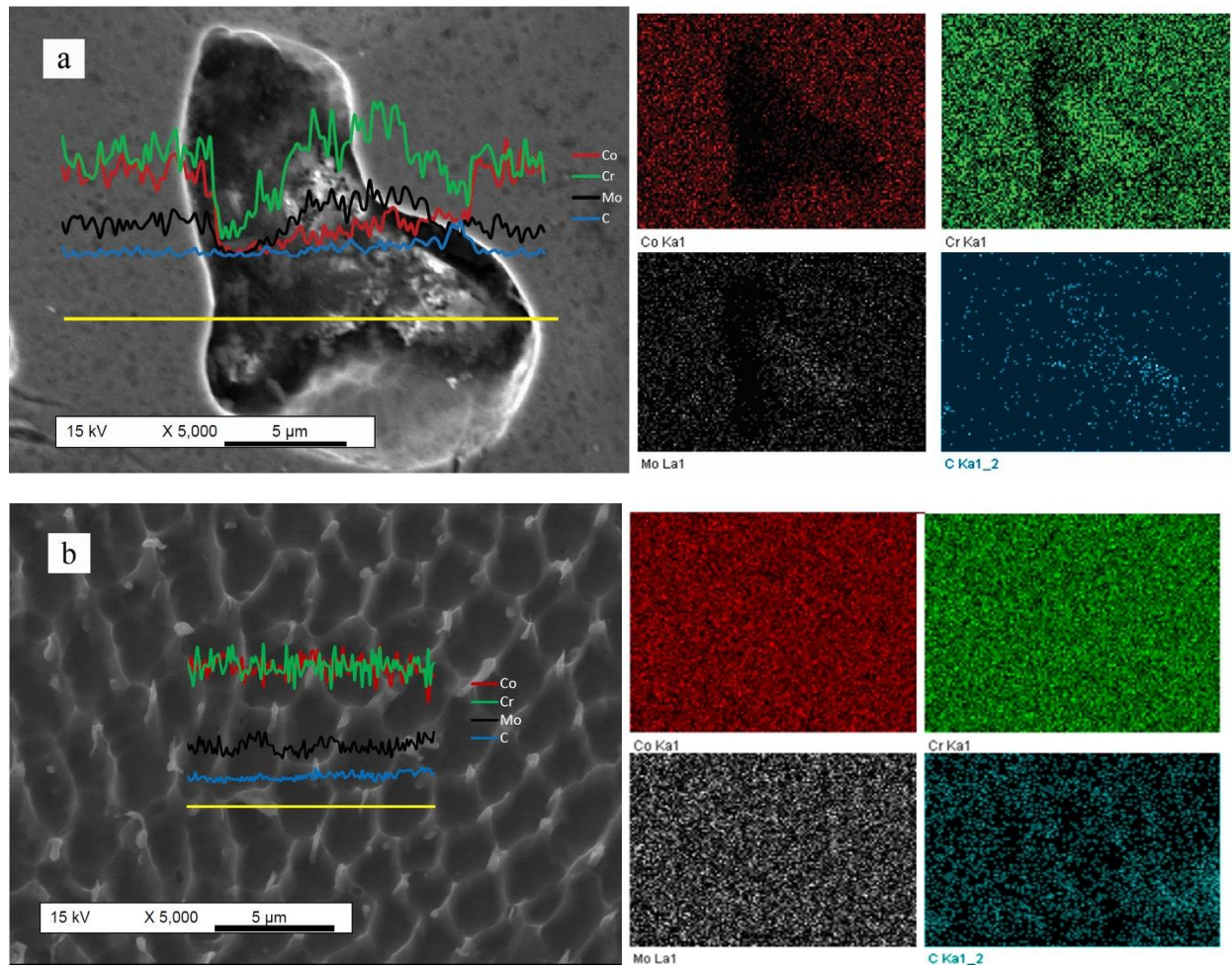


*Figure 3.28 – EDS line scan and mapping of CoCrMoC alloy, a) as-cast, b) laser surface modified.*

#### ***4. Conclusions***

In this research, rapid solidification is proposed to create Co-Cr-Mo-C alloy samples. Two methods were used to prepare samples: a “V” shaped copper mold with water cooling and laser surface modification. As-cast samples were also homogenized, quenched and then isothermally aged to prepare the corresponding TTT diagram. Results are summarized below:

- Using the wedge-shaped sand and copper mold to create rapid solidification regimes with cooling rate up to 450 K/s resulted in a columnar dendritic microstructure. The microstructure, morphology, and size of the dendrites were highly affected by cooling rate. Grain boundaries vanished by changing to copper mold from sand mold. Increasing the cooling rate from 10 K/s to 450 K/s resulted in a reduction in average secondary dendrite arm spacing from 31 $\mu$ m to 5 $\mu$ m.
- The shape, composition, and size of carbides was highly affected by cooling rate. Increasing the cooling rate from 10 K/s to 450 K/s resulted in a change in carbide morphology from lamellar to blocky, along with a decrease in size from 15 $\mu$ m to 4 $\mu$ m. The main metal alloying elements in lamellar carbides were Mo and Co, while the blocky carbides consisted of Co, Mo, and Cr.
- Rapid solidification effects, such as excess vacancies and the development of numerous stacking faults and corresponding intersections, strongly favored the athermal martensite,  $\epsilon$ -HCP. The formation of athermal martensite microstructure was confirmed by means of SEM and XRD. Increasing the cooling rate from 10 K/s to 120 K/s, 230 K/s, and 450 K/s was found to increase the fraction of  $\epsilon$ -HCP amount from less than a 1% to 17%, 29%, and 46%, respectively.

- Potentiodynamic polarization curves indicate that increasing the cooling rate from 10 K/s to 450 K/s will increase the corrosion potential from -280mV to -240 mV.
- Laser welding was found to alter the surface solidified structure to cellular, with a cell width of 2 $\mu$ m and carbides dispersed within cell walls with an average size of 200 nm. The final structure was found to be 100%  $\gamma$ -FCC, which was attributed to laser welding reducing the stacking fault defects needed for  $\epsilon$ -HCP nuclei.
- Isothermal aging heat treatment was found to promote the formation of  $\epsilon$ -HCP structure in Co-Cr-Mo-C alloy. 95%  $\epsilon$ -HCP structure was achieved with 15 hours of aging at 800°C. Increasing the ageing temperature to 900°C was found to increase the required time for formation of 95%  $\epsilon$ -HCP structure to 25 hours.

## ***5. References***

- [1] M. Lysaght, T. Webster, S. Breiter, C. Yao, J. Lu, T. J. Webster, E. Oral, M. J. Ebert, S. Lyu, M. F. Wolf, M. T. Rise, M. N. Helmus, C. M. Cunanan, M. Hiles, J. Hodde, M. N. Rahaman, B. S. Bal, D. U. Erbulut, I. Lazoglu, Y. Chen, and D. Gorth, in *Biomaterials for Artificial Organs*, M. Lysaght and T. J. Webster, Eds., ed: Woodhead Publishing, 2011, pp. ix-xi.
- [2] T. Hanawa, "Research and development of metals for medical devices based on clinical needs," *Science and technology of advanced materials*, vol. 13, pp. 064102-064102, 2012.
- [3] M. Navarro, A. Michiardi, O. Castaño, and J. A. Planell, "Biomaterials in orthopaedics," *Journal of the Royal Society, Interface*, vol. 5, pp. 1137-1158, 2008.
- [4] M. Geetha, A. K. Singh, R. Asokamani, and A. K. Gogia, "Ti based biomaterials, the ultimate choice for orthopaedic implants – A review," *Progress in Materials Science*, vol. 54, pp. 397-425, 2009/05/01/ 2009.
- [5] M. Long and H. J. Rack, "Titanium alloys in total joint replacement—a materials science perspective," *Biomaterials*, vol. 19, pp. 1621-1639, 1998/09/01/ 1998.
- [6] S. H. Teoh, "Fatigue of biomaterials: a review," *International Journal of Fatigue*, vol. 22, pp. 825-837, 2000/11/01/ 2000.
- [7] S. Ghosh and S. Abanteriba, "Status of surface modification techniques for artificial hip implants," *Science and technology of advanced materials*, vol. 17, pp. 715-735, 2016.
- [8] A. Mahajan and S. S. Sidhu, "Surface modification of metallic biomaterials for enhanced functionality: a review," *Materials Technology*, vol. 33, pp. 93-105, 2018/01/28 2018.
- [9] N. Eliaz, "Corrosion of Metallic Biomaterials: A Review," *Materials (Basel, Switzerland)*, vol. 12, p. 407, 2019.
- [10] in *Metals for Biomedical Devices*, M. Niinomi, Ed., ed: Woodhead Publishing, 2010, pp. i-iii.
- [11] J. E. Lemons, F. Misch-Dietsh, and M. S. McCracken, "Chapter 4 - Biomaterials for Dental Implants," in *Dental Implant Prosthetics (Second Edition)*, C. E. Misch, Ed., ed St. Louis: Mosby, 2015, pp. 66-94.
- [12] K. Yang and Y. Ren, "Nickel-free austenitic stainless steels for medical applications," *Science and technology of advanced materials*, vol. 11, pp. 014105-014105, 2010.
- [13] L.-C. Zhang and L.-Y. Chen, "A Review on Biomedical Titanium Alloys: Recent Progress and Prospect," *Advanced Engineering Materials*, vol. 21, p. 1801215, 2019.
- [14] ASTM E139-11, *Standard Test Methods for Conducting Creep, Creep-Rupture, and Stress-Rupture Tests of Metallic Materials*. West Conshohocken, PA, 2006: ASTM International.
- [15] L. Z. Zhuang and E. W. Langer, "Effects of cooling rate control during the solidification process on the microstructure and mechanical properties of cast Co-Cr-Mo alloy used for surgical implants," *Journal of Materials Science*, vol. 24, pp. 381-388, February 01 1989.
- [16] M. Hindsén, Å. S. Carlsson, and H. Möller, "Orthopaedic metallic implants in extremity fractures and contact allergy," *Journal of the European Academy of Dermatology and Venereology*, vol. 2, pp. 22-26, 1993.
- [17] R. Adams and C. Altstetter, *Trans. TMS-AIME*, vol. 242, pp. 139–143, 1968.
- [18] S. M. Kurtz and J. N. Devine, "PEEK biomaterials in trauma, orthopedic, and spinal implants," *Biomaterials*, vol. 28, pp. 4845-4869, 2007/11/01/ 2007.
- [19] K. C. Antony, "Wear-Resistant Cobalt-Base Alloys," *JOM*, vol. 35, pp. 52-60, February 01 1983.
- [20] S. Spriano, S. Yamaguchi, F. Baino, and S. Ferraris, "A critical review of multifunctional titanium surfaces: New frontiers for improving osseointegration and host response, avoiding bacteria contamination," *Acta Biomaterialia*, vol. 79, pp. 1-22, 2018/10/01/ 2018.
- [21] Y. Liao, E. Hoffman, M. Wimmer, A. Fischer, J. Jacobs, and L. Marks, "CoCrMo Metal-on-Metal Hip Replacements," *Phys Chem Chem Phys : PCCP*, vol. 15, p. 10.1039/c2cp42968c, 2013.
- [22] A. Jokstad, U. Braegger, J. B. Brunski, A. B. Carr, I. Naert, and A. Wennerberg, "Quality of dental implants\*," *International Dental Journal*, vol. 53, pp. 409-443, 2003.

- [23] C. R. Brooks, *Heat treatment, structure, and properties of nonferrous alloys*. Ohio American Society for Metals: inMetals park, 1982.
- [24] L. Casabán Julián and A. Igual Muñoz, "Influence of microstructure of HC CoCrMo biomedical alloys on the corrosion and wear behaviour in simulated body fluids," *Tribol Int*, vol. 44, pp. 318-329, 2011.
- [25] S. Hiromoto, E. Onodera, A. Chiba, K. Asami, and T. Hanawa, "Microstructure and corrosion behaviour in biological environments of the new forged low-Ni Co–Cr–Mo alloys," *Biomaterials*, vol. 26, pp. 4912-4923, 2005.
- [26] H. F. López and A. J. Saldivar-Garcia, "Martensitic Transformation in a Cast Co-Cr-Mo-C Alloy," *Metallurgical and Materials Transactions A*, vol. 39, pp. 8-18, 2007.
- [27] A. L. L. Ramirez-Ledesma, H.F.; Juarez-Islas, J.A., "Evaluation of Chill Cast Co-Cr Alloys for Biomedical Applications," *Metals*, vol. 6, 2016.
- [28] H. K. Koerten, J. J. M. Onderwater, E. W. A. Koerten, F. P. Bernoski, and R. G. H. H. Nelissen, "Observations at the articular surface of hip prostheses: An analytical electron microscopy study on wear and corrosion," *J Biomed Materials Res*, vol. 54, pp. 591-596, 2001.
- [29] H. Nakayama, *Dentistry and Metal Allergy*. London: Dental-Diamond Co, 1997.
- [30] R. W.-W. Hsu, C.-C. Yang, C.-A. Huang, and Y.-S. Chen, "Electrochemical corrosion studies on Co–Cr–Mo implant alloy in biological solutions," *Mater Chem Phys*, vol. 93, pp. 531-538, 2005.
- [31] R. Kaiser, K. Williamson, C. O'Brien, and D. J. Browne, "Effects of Section Size, Surface Cooling Conditions, and Crucible Material on Microstructure and As-Cast Properties of Investment Cast Co-Cr Biomedical Alloy," *Metallurgical and Materials Transactions A*, vol. 44, pp. 5333-5342, December 01 2013.
- [32] R. Lizárraga, F. Pan, L. Bergqvist, E. Holmström, Z. Gercsi, and L. Vitos, "First Principles Theory of the hcp-fcc Phase Transition in Cobalt," *Scientific reports*, vol. 7, pp. 3778-3778, 2017.
- [33] L. E. Ramírez-Vidaurri, M. Castro-Román, M. Herrera-Trejo, C. V. García-López, and E. Almanza-Casas, "Cooling rate and carbon content effect on the fraction of secondary phases precipitate in as-cast microstructure of ASTM F75 alloy," *Journal of Materials Processing Technology*, vol. 209, pp. 1681-1687, 2009.
- [34] K. P. Gupta, "The Co-Cr-Ta (Cobalt-Chromium-Tantalum) System," *Journal of Phase Equilibria and Diffusion*, vol. 26, pp. 93-97, February 01 2005.
- [35] Y. Li, J. Wang, X. Zhu, Q. Feng, X. Li, and X. Feng, "Urinary protein markers predict the severity of renal histological lesions in children with mesangial proliferative glomerulonephritis," *BMC Nephrology*, vol. 13, p. 29, May 20 2012.
- [36] D. A. Puleo, "Biochemical surface modification of Co-Cr-Mo," *Biomaterials*, vol. 17, pp. 217-222, 1996.
- [37] S.-H. Lee, E. Takahashi, N. Nomura, and A. Chiba, "Effect of Heat Treatment on Microstructure and Mechanical Properties of Ni- and C-Free Co–Cr–Mo Alloys for Medical Applications," *MATERIALS TRANSACTIONS*, vol. 46, pp. 1790-1793, 2005.
- [38] *ASTM F75-12, Standard Specification for Cobalt-28 Chromium-6 Molybdenum Alloy Castings and Casting Alloy for Surgical Implants (UNS R30075)*. West Conshohocken, PA: ASTM International, 2012.
- [39] I. Milošev and H. H. Strehblow, "The composition of the surface passive film formed on CoCrMo alloy in simulated physiological solution," *Electrochimica Acta*, vol. 48, pp. 2767-2774, 2003.
- [40] A. J. Saldivar Garcia, A. Mani Medrano, and A. Salinas Rodriguez, "Effect of solution treatments on the fcc/hcp isothermal martensitic transformation in Co-27Cr-5Mo-005C aged at 800 C," *Scripta Materialia*, vol. 40, pp. 717-722, 1999.

- [41] A. d. J. Saldívar García, A. M. Medrano, and A. S. Rodríguez, "Formation of hcp martensite during the isothermal aging of an fcc Co-27Cr-5Mo-0.05C orthopedic implant alloy," *Metallurgical and Materials Transactions A*, vol. 30, pp. 1177-1184, May 01 1999.
- [42] G. B. Olson and M. Cohen, "A general mechanism of martensitic nucleation: Part I. General concepts and the FCC  $\rightarrow$  HCP transformation," *Metallurgical Transactions A*, vol. 7, pp. 1897-1904, December 01 1976.
- [43] J. B. Vander Sande, J. R. Coke, and J. Wulff, "A transmission electron microscopy study of the mechanisms of strengthening in heat-treated Co-Cr-Mo-C alloys," *Metallurgical Transactions A*, vol. 7, pp. 389-397, March 01 1976.
- [44] H. F. López and A. J. Saldívar-García, "Martensitic Transformation in a Cast Co-Cr-Mo-C Alloy," *Metall Mater Trans A*, vol. 39, pp. 8-18, January 01 2008.
- [45] R. N. J. Taylor and R. B. Waterhouse, "A study of the ageing behaviour of a cobalt based implant alloy," *J Mater Sci*, vol. 18, pp. 3265-3280.
- [46] K. Rajan and J. B. Vander Sande, "Room temperature strengthening mechanisms in a Co-Cr-Mo-C alloy," *Journal of Materials Science*, vol. 17, pp. 769-778, March 01 1982.
- [47] S. R. Pati and M. Cohen, "Nucleation of the isothermal martensitic transformation," *Acta Metallurgica*, vol. 17, pp. 189-199, 1969/03/01/ 1969.
- [48] K. Yamanaka, M. Mori, and A. Chiba, "Developing high strength and ductility in biomedical Co-Cr cast alloys by simultaneous doping with nitrogen and carbon," *Acta Biomaterialia*, vol. 31, pp. 435-447, 2016/02/01/ 2016.
- [49] M. Mori, K. Yamanaka, S. Sato, K. Wagatsuma, and A. Chiba, "Microstructures and Mechanical Properties of Biomedical Co-29Cr-6Mo-0.14N Alloys Processed by Hot Rolling," *Metall Mater Trans A*, vol. 43, pp. 3108-3119, September 01 2012.
- [50] A. L. Ramirez-Ledesma, E. Lopez-Molina, H. F. Lopez, and J. A. Juarez-Islas, "Athermal  $\epsilon$ -martensite transformation in a Co-20Cr alloy: Effect of rapid solidification on plate nucleation," *Acta Mater*, vol. 111, pp. 138-147, 2016/06/01/ 2016.
- [51] K. E. Easterling and A. R. Thölen, "The nucleation of martensite in steel," *Acta Metallurgica*, vol. 24, pp. 333-341, 1976/04/01/ 1976.
- [52] A. L. Ramirez-Ledesma, H. F. Lopez, and J. A. Juarez-Islas, "Rapid Solidification Effects on the Development of an HCP Matrix in a Co-20Cr Alloy," *Metallurgical and Materials Transactions A*, vol. 47, pp. 2566-2568, June 01 2016.
- [53] S. Allain, J. P. Chateau, O. Bouaziz, S. Migot, and N. Guelton, "Correlations between the calculated stacking fault energy and the plasticity mechanisms in Fe-Mn-C alloys," *Materials Science and Engineering: A*, vol. 387, pp. 158-162, 2004/12/15/ 2004.
- [54] L. Rémy, A. Pineau, and B. Thomas, "Temperature dependence of stacking fault energy in close-packed metals and alloys," *Materials Science and Engineering*, vol. 36, pp. 47-63, 1978/11/01/ 1978.
- [55] K. Yamanaka, M. Mori, K. Yoshida, K. Kuramoto, and A. Chiba, "Manufacturing of high-strength Ni-free Co-Cr-Mo alloy rods via cold swaging," *Journal of the Mechanical Behavior of Biomedical Materials*, vol. 60, pp. 38-47, 2016.
- [56] K. Yamanaka, M. Mori, S. Kurosu, H. Matsumoto, and A. Chiba, "Ultrafine Grain Refinement of Biomedical Co-29Cr-6Mo Alloy during Conventional Hot-Compression Deformation," *Metallurgical and Materials Transactions A*, vol. 40, pp. 1980-1994, August 01 2009.
- [57] J. L. Acevedo-Dávila, H. F. López, F. Cepeda-Rodríguez, M. Rodríguez-Reyes, F. García-Vazquez, and H. M. Hernández-García, "Microstructural effects on the wear behavior of a biomedical as-cast Co-27Cr-5Mo-0.25C alloy exposed to pulsed laser melting," *Journal of Biomedical Materials Research Part A*, vol. 102, pp. 2008-2016, 2014.

- [58] A. Mani, R. Salinas, and H. F. Lopez, "Deformation induced FCC to HCP transformation in a Co–27Cr–5Mo–0.05C alloy," *Materials Science and Engineering: A*, vol. 528, pp. 3037-3043, 2011/03/25/ 2011.
- [59] S. Kurosu, H. Matsumoto, and A. Chiba, "Isothermal Phase Transformation in Biomedical Co–29Cr–6Mo Alloy without Addition of Carbon or Nitrogen," *Metallurgical and Materials Transactions A*, vol. 41, pp. 2613-2625, October 01 2010.
- [60] Y. Tomota, M. Strum, and J. W. Morris, "Microstructural dependence of Fe-high Mn tensile behavior," *Metallurgical Transactions A*, vol. 17, pp. 537-547, March 01 1986.
- [61] J. Talonen and H. Hänninen, "Energetics of Plastic Deformation of Metastable Austenitic Stainless Steel," *steel research international*, vol. 78, pp. 260-265, 2007.
- [62] in *Martensitic Transformation*, M. E. Fine, M. Meshii, C. M. Wayman, and Z. Nishiyama, Eds., ed: Academic Press, 1978, p. ix.
- [63] C. Cayron, "Continuous atomic displacements and lattice distortion during fcc–bcc martensitic transformation," *Acta Materialia*, vol. 96, pp. 189-202, 2015/09/01/ 2015.
- [64] O. N. Senkov, G. B. Wilks, D. B. Miracle, C. P. Chuang, and P. K. Liaw, "Refractory high-entropy alloys," *Intermetallics*, vol. 18, pp. 1758-1765, 2010/09/01/ 2010.
- [65] T. Wang, B. Li, M. Li, Y. Li, Z. Wang, and Z. Nie, "Effects of strain rates on deformation twinning behavior in  $\alpha$ -titanium," *Materials Characterization*, vol. 106, pp. 218-225, 2015/08/01/ 2015.
- [66] S. Hu, J. A. Loo, and D. T. Wong, "Human body fluid proteome analysis," *Proteomics*, vol. 6, pp. 6326-6353, 2006.
- [67] T. Hanawa, S. Hiromoto, and K. Asami, "Characterization of the surface oxide film of a Co–Cr–Mo alloy after being located in quasi-biological environments using XPS," *Applied Surface Science*, vol. 183, pp. 68-75, 2001/11/12/ 2001.
- [68] K. L. Luthra, "Low Temperature Hot Corrosion of Cobalt-Base Alloys: Part II. Reaction Mechanism," *Metallurgical Transactions A*, vol. 13, pp. 1853-1864, October 01 1982.
- [69] P. E. Sinnott-Jones, J. A. Wharton, and R. J. K. Wood, "Micro-abrasion–corrosion of a CoCrMo alloy in simulated artificial hip joint environments," *Wear*, vol. 259, pp. 898-909, 2005/07/01/ 2005.
- [70] T. Hryniewicz, R. Rokicki, and K. Rokosz, "Co–Cr alloy corrosion behaviour after electropolishing and "magneto-electropolishing" treatments," *Materials Letters*, vol. 62, pp. 3073-3076, 2008.
- [71] A. Igual Munoz, J. Schwiesau, B. M. Jolles, and S. Mischler, "In vivo electrochemical corrosion study of a CoCrMo biomedical alloy in human synovial fluids," *Acta Biomater.*, vol. 21, pp. 228-236, 2015.
- [72] E. Krasicka-Cydzik, Z. Oksiuta, and J. R. Dabrowski, "Corrosion testing of sintered samples made of the Co–Cr–Mo alloy for surgical applications," *Journal of Materials Science: Materials in Medicine*, vol. 16, pp. 197-202.
- [73] F. Ren, W. Zhu, and K. Chu, "Fabrication, tribological and corrosion behaviors of ultra-fine grained Co–28Cr–6Mo alloy for biomedical applications," *J Mech Behav Biomed Mater*, vol. 60, pp. 139-147, 2016.
- [74] Y. N. Petrov, G. I. Prokopenko, B. N. Mordyuk, M. A. Vasylyev, S. M. Voloshko, V. S. Skorodzievski, and V. S. Filatova, "Influence of microstructural modifications induced by ultrasonic impact treatment on hardening and corrosion behavior of wrought Co–Cr–Mo biomedical alloy," *Mater Sci Eng: C*, vol. 58, pp. 1024-1035, 2016.
- [75] W. C. Rodrigues, L. R. Broilo, L. Schaeffer, G. Knörnschild, and F. R. M. Espinoza, "Powder metallurgical processing of Co–28%Cr–6%Mo for dental implants: Physical, mechanical and electrochemical properties," *Powder Technol*, vol. 206, pp. 233-238, 2011.
- [76] W. Kurz, B. Giovanola, and R. Trivedi, "Theory of microstructural development during rapid solidification," *Acta Metallurgica*, vol. 34, pp. 823-830, 1986/05/01/ 1986.

- [77] J. S. Langer and H. Müller-Krumbhaar, "Theory of dendritic growth—I. Elements of a stability analysis," *Acta Metallurgica*, vol. 26, pp. 1681-1687, 1978/11/01/ 1978.
- [78] W. W. Mullins and R. F. Sekerka, "Stability of a Planar Interface During Solidification of a Dilute Binary Alloy," in *Dynamics of Curved Fronts*, P. Pelcé, Ed., ed San Diego: Academic Press, 1988, pp. 345-352.
- [79] X. Lin, Y. Li, M. Wang, L. Feng, J. Chen, and W. Huang, "Columnar to equiaxed transition during alloy solidification," *Science in China Series E: Technological Sciences*, vol. 46, pp. 475-489, October 01 2003.
- [80] B. Wei, D. M. Herlach, F. Sommer, and W. Kurz, "Rapid solidification of undercooled eutectic and monotectic alloys," *Materials Science and Engineering: A*, vol. 173, pp. 355-359, 1993/12/20/ 1993.
- [81] G. Kühn, "W. Kurz, D. J. Fisher, Fundamentals of Solidification. Trans Tech Publications, Switzerland-Germany-UK-USA, 1986 (Erstauflage 1984), 242 Seiten, zahlreiche Abbildungen und Tabellen, Sachwortindex, SFr 54.00, ISBN 0-87849-523-3," *Crystal Research and Technology*, vol. 21, pp. 1176-1176, 1986.
- [82] W. Kurz and D. J. Fisher, "Dendrite growth at the limit of stability: tip radius and spacing," *Acta Metallurgica*, vol. 29, pp. 11-20, 1981/01/01/ 1981.
- [83] M. Sage and C. Guillaud, *Rev. Métall.*, vol. 47, pp. 139-145, 1950.
- [84] J. P. Hirth, "Thermodynamics of stacking faults," *Metallurgical Transactions*, vol. 1, pp. 2367-2374.
- [85] P. J. Ferreira and P. Müllner, "A thermodynamic model for the stacking-fault energy," *Acta Materialia*, vol. 46, pp. 4479-4484, 1998/08/10/ 1998.
- [86] M. C. Flemings, *Solidification Processing*. New York: McGraw-Hill, 1974.
- [87] S. Kou, *Welding Metallurgy*, 2nd ed.: A Wiley-Interscience publication, 2003.
- [88] W. F. Savage, Nippes, E. F., and Erickson, J. S. , "Solidification Mechanisms in Fusion Welds," *Weld. J.*, vol. 55, 1976.
- [89] J. W. Elmer, S. M. Allen, and T. W. Eagar, "Microstructural development during solidification of stainless steel alloys," *Metall Trans A*, vol. 20, pp. 2117-2131, October 01 1989.
- [90] A. K. Roy and R. P. Chhabra, "Prediction of solute diffusion coefficients in liquid metals," *Metallurgical Transactions A*, vol. 19, pp. 273-279, February 01 1988.
- [91] J. L. Acevedo-Davila, H. F. Lopez, F. Cepeda-Rodriguez, M. Rodriguez-Reyes, F. Garcia-Vazquez, and H. M. Hernandez-Garcia, "Microstructural effects on the wear behavior of a biomedical as-cast Co-27Cr-5Mo-0.25C alloy exposed to pulsed laser melting," *J Biomed Mater Res A*, vol. 102, pp. 2008-16, 2014.
- [92] E. Bettini, T. Eriksson, M. Boström, C. Leygraf, and J. Pan, "Influence of metal carbides on dissolution behavior of biomedical CoCrMo alloy: SEM, TEM and AFM studies," *Electrochimica Acta*, vol. 56, pp. 9413-9419, 2011/10/30/ 2011.
- [93] J. R. Davis, *Nickel Cobalt, and their Alloys*. United State of America: ASM International Handbook, 2000.
- [94] A. L. Ramirez-Ledesma, H. F. Lopez, and J. A. Juarez-Islas, "Rapid Solidification Effects on the Development of an HCP Matrix in a Co-20Cr Alloy," *Metall Mater Trans A*, vol. 47, pp. 2566-2568, June 01 2016.
- [95] J. Escobedo, J. Méndez, D. Cortés, J. Gómez, M. Méndez, and H. Mancha, "Effect of nitrogen on the microstructure and mechanical properties of a CoCrMo alloy," *Materials & Design*, vol. 17, pp. 79-83, 1996/01/01/ 1996.
- [96] J. P. Hirth, "The influence of grain boundaries on mechanical properties," *Metallurgical Transactions*, vol. 3, pp. 3047-3067, December 01 1972.

- [97] C. Brito, T. Vida, E. Freitas, N. Cheung, J. E. Spinelli, and A. Garcia, "Cellular/dendritic arrays and intermetallic phases affecting corrosion and mechanical resistances of an Al–Mg–Si alloy," *J Alloys Compd*, vol. 673, pp. 220-230, 2016.
- [98] M. Momeni, M. Behazin, and J. C. Wren, "Mass and Charge Balance (MCB) Model Simulations of Current, Oxide Growth and Dissolution during Corrosion of Co-Cr Alloy Stellite-6," *J Electrochem Soc*, vol. 163, pp. C94-C105, January 1, 2016 2016.
- [99] M. Momeni and J. C. Wren, "A mechanistic model for oxide growth and dissolution during corrosion of Cr-containing alloys," *Faraday Discuss*, vol. 180, pp. 113-135, 2015.
- [100] Q. W. Knapp and J. C. Wren, "Film formation on type-316L stainless steel as a function of potential: Probing the role of gamma-radiation," *Electrochim Acta*, vol. 80, pp. 90-99, 2012/10/01/ 2012.
- [101] S. K. Bonagani, V. Bathula, and V. Kain, "Influence of tempering treatment on microstructure and pitting corrosion of 13 wt.% Cr martensitic stainless steel," *Corros Sci*, vol. 131, pp. 340-354, 2018/02/01/ 2018.
- [102] K. Chandra, V. Kain, and R. Tewari, "Microstructural and electrochemical characterisation of heat-treated 347 stainless steel with different phases," *Corros Sci*, vol. 67, pp. 118-129, 2013/02/01/ 2013.

## **6. *Appendix***

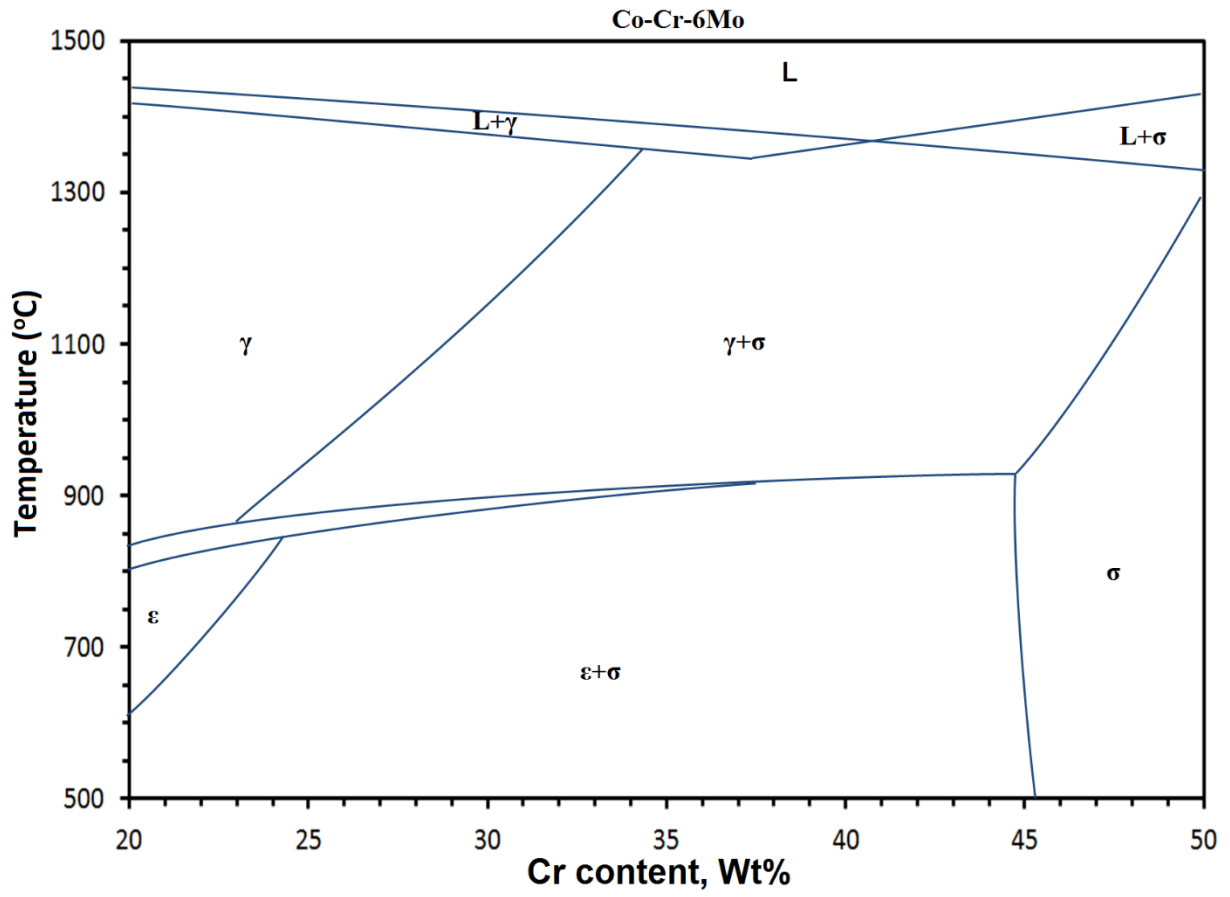
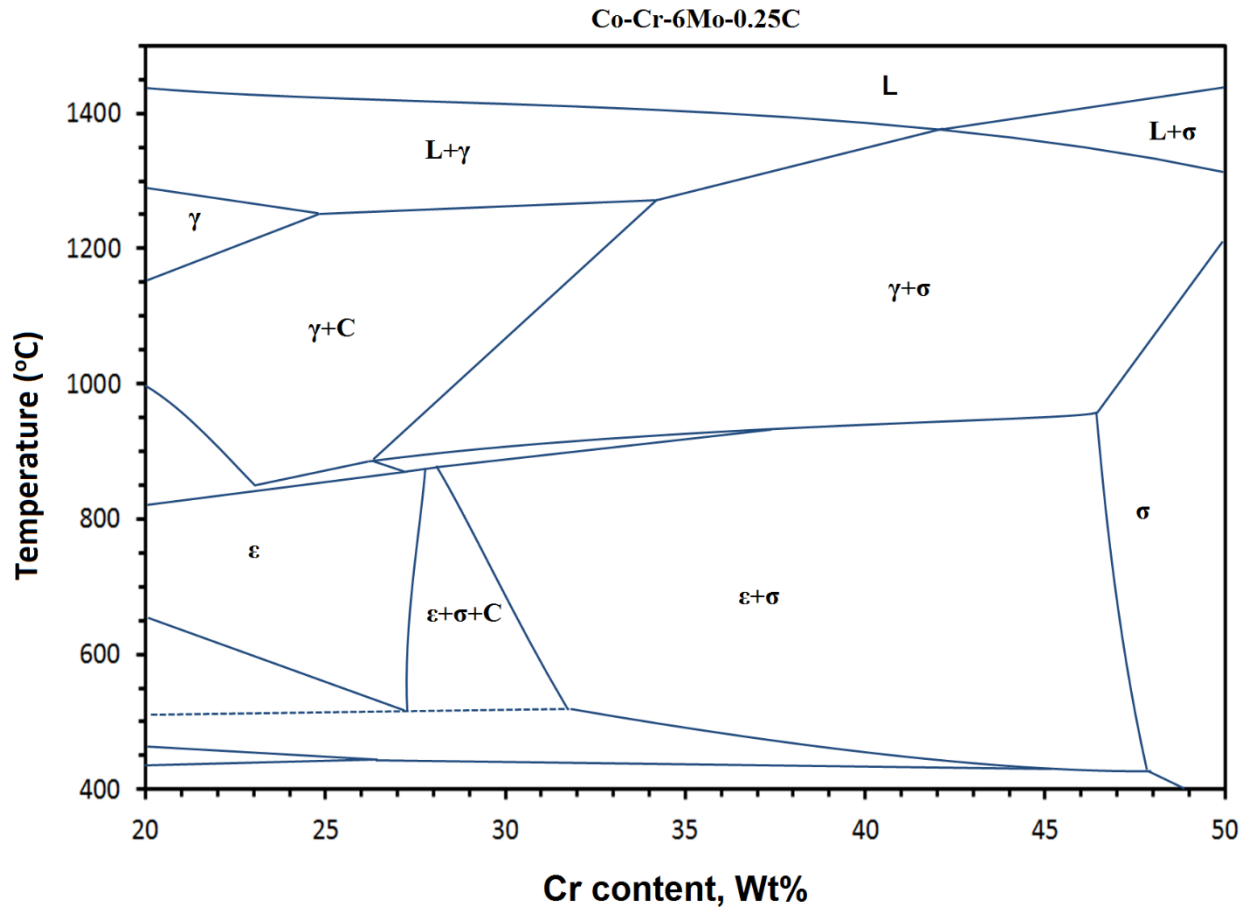


Figure 6.1A - Phase diagram of Co-Cr-6Mo based on Thermo-Calc simulation software.



*Figure 6.2A - Phase diagram of Co-Cr-6Mo-0.25C based on Thermo-Calc simulation software (C = Carbides).*

*Table 6.1A – Amount of HCP structure formed in Co-Cr-Mo-C alloy for different ageing temperature and time*

<b>Ageing Temperature (°C)</b>	<b>Time (h)</b>	<b>HCP structure (%)</b>
750	5	32
	10	51
	13	74
	15	83
	20	96
800	5	38
	7	49
	10	76
	13	87
	15	95
850	5	33
	10	53
	13	76
	15	81
	20	94
900	5	31
	10	37
	13	41
	15	52
	20	76
	25	94

## ***7. Curriculum Vitae***

## EDUCATION

- **PhD candidate, Material Science& Engineering (GPA: 3.95)**  
University of Wisconsin Milwaukee, Expect to graduate by May 2019
- **Master of Science, Material Engineering (GPA: 3.5)**  
Ferdowsi University of Mashhad, Iran. Graduated September 2013
- **Bachelor of Science, Material Science& Engineering (GPA: 3.0)**  
Ferdowsi University of Mashhad, Iran. Graduated September 2010

## SELECTED PUBLICATIONS AND CONFERENCE PRESENTATION

- **Hamid-Reza Erfanian-Nazif Toosi**, Hugo F. Lopez, The Effect of Rapid Solidification on Microstructure and Mechanical Properties of Advanced Biomaterial Co-Cr-Mo-C Alloy, International Journal of Advances in Science Engineering and Technology, March 2019, Volume 7, 1 Spl. Issue-2, 17-19
- Elhajjar Rani, Titi Hani H, Van Dyke Stacy, **Erfanian Hamid**, Correlation of ASTM D4833 and D6241 Geotextile Puncture Test Methods and Results for Use on WisDOT Projects, Report number: WisDOT ID no. 0092-15-07 Affiliation: Wisconsin Highway Research Program, Wisconsin Department of Transportation
- **H.R. Erfanian-Naziftoosi**, Ernesto J. Rincon, Hugo Lopez, Creep Properties of As-Cast Al-A319 Alloy: T4 and T7 Heat Treatment Effects, Metallurgical and Materials Transactions A (2016), 47, 8, 4258–4267
- **HR Erfanian-Naziftoosi**, Seyedmohammad S Shams, Rani Elhajjar, Composite wave springs: Theory and design, Materials & Design, Volume 95, 5 April 2016, Pages 48–53
- **H.R. Erfanian-Naziftoosi**, N. Haghddadi, A.R. Kiani-Rashid, The effect of isothermal heat treatment time on the microstructure and properties of 2.11% Al austempered ductile iron, Journal of Materials Engineering and Performance, August 2012, Volume 21, Issue 8, pp 1785-1792.
- N. Haghddadi, B. Bazaz, **H.R. Erfanian-Naziftoosi**, A.R. Kiani-Rashid, Microstructural and mechanical characteristics of Al-alloyed ductile iron upon casting and annealing, September 2012 International Journal of Minerals Metallurgy and Materials 19(9)
- **Hamid-Reza Erfanian-Naziftoosi**, Hugo López, Microstructure and corrosion behavior of as-cast and laser surface modified Co-Cr-Mo-C alloy (under review)
- Hugo F Lopez, **Hamid-Reza Erfanian-Naziftoosi**, Effect of Rapid Solidification on the Microstructure of a Biomaterial Co-Cr-Mo-C Alloy, Pan American Materials Congress: Advanced Biomaterials, TMS 2017- Feb 26-March 2- San Diego
- **Hamid-Reza Erfanian-Naziftoosi**, Hugo López, The Effect of Rapid Solidification on Physical Properties of Advanced Biomaterial Co-Cr-Mo-C Alloy, Biomaterials- Next Generation Biomaterials- Metallic implant materials, MS&T2017-Oct 8-12- Pittsburgh

## WORK EXPERIENCE

### **Materials Engineer (Product Development), Dec 2018-now**

*Sturtevant, WI*

- As an expert in metallic (ferrous and non-ferrous) and nonmetallic (polymers and composites) materials selection and failure analysis for the Evinrude outboard engine division, I am supporting new product development, led problem-solving teams, and conducting research, internally, in collaboration with suppliers and academic partners. I am responsible for materials selection, failure analysis and corrosion prevention strategy for G2 outboard engine.

**Materials Engineer (Product Development) Co-Op, BRP US Inc., October 2016-Dec 2018**

*Sturtevant, WI*

- Assist with laboratory evaluation of materials including steel, aluminum, cast iron, and plastics for failure investigation, new product development, prototype design, and manufacturing support.
- Support development of methods and processes for cost reduction, corrosion and quality improvement by working with team developing on different heat treatment process, casting, material selection, coating, painting, and fasteners.

**Material Engineer, Material Engineering Consultant and Welding Inspection Co. March2012-June 2014**

*Mashhad, Iran*

- Technical inspector supervisor and responsible for material and process selection of weld parts.

**Process Engineer, Industrial Forging Company, Internship, Summer2010**

*Mashhad, Iran*

- Quality control of products to apply improvement on forging and heat treatment process.

**Teaching Assistant, UW-Milwaukee, September 2014-May 2018**

*Milwaukee, WI*

- Material Lab, MATLENG411- Fall 2017-
- Material 201 lab instructor including metallography and mechanical testing.
- TAs supervisor in material department at UW-Milwaukee.
- Training new TAs and maintaining the Lab equipment.

**Research Assistant, UW-Milwaukee, September 2014-December 201**

*Milwaukee, WI*

- Studying physical, mechanical and corrosion properties of cast and rapidly solidified Co-alloy.
- Studying the heat treatment and creep properties of Al-A319 alloy used in automotive industry.
- Analyzing the mechanical behavior of springs made by Carbon fiber/epoxy composites by means of experimental, analytical, and numerical methods.
- Developing new specification for soil stabilizer fabrics under WI-DOT supervision.
- Studying the effect of powder recycling in additive manufacturing method (DMLS).
- Working with customers to deliver desired parts and reduce production cost.

**ENGINEERING SOCIETIES MEMBERSHIP**

- Member of ASM Materials Property Database Committee
- Organizing Committee Member of SAE Small Engine Conference (SETC)
- American for Iron & Steel Technology, American Society of Material, The Minerals, Metals & Materials Society, and The American Ceramic Society

**HONORS/AWARDS**

- Distinguished Dissertation Fellowship, UW-Milwaukee *Fall 2018*
- Chancellor's Graduate Student Award, UW-Milwaukee *October 2016*
- Iran Nano Technology Initiative Council, Research Thesis Grant *November2011*
- Ferdowsi University of Mashhad, Research Thesis Grant *November2011*